Single crystal growth and structural characterization of intermetallic phases for thermoelectric applications

Mirtha Pillaca Quispe

München, 2020

Single crystal growth and structural characterization of intermetallic phases for thermoelectric applications

Dissertation
der Fakultät für Geowissenschaften
der Ludwig-Maximilians-Universität München
zur Erlangung des Grades Doktor rer. nat.

vorgelegt von
MIRTHA PILLACA QUISPE
aus Peru

München, den 17.01.2020

Erstgutachter: Prof. Dr. Peter Gille

Zweitgutachter: Prof. Dr. SoHyun Park

Tag der mündlichen Prüfung: 03.08.2020

Dedicated to my father, Jaime Pillaca Palomino, and my family.

Contents

Abstract

During the last decades, thermoelectric materials have been profiled to be part of the solution to the problem of energy consumption of the world. In particular, binary compounds ($FeSb_2$ and $CoSb_3$) and third-component modifications based on them were found to be promising candidates. The main advantage of these compounds compared to the present record holders like PbTe are the better availability and less toxicity of their constituting metals.

$FeSb_2$ (marcasite-type structure) and $CoSb_3$ (skutterudite-type structure) are peritectically melting compounds with decomposition temperatures of 750 °C and 874 °C, respectively. Thus, they cannot be crystallized from congruent melts but have to be grown below the peritectic temperature from Sb-rich solutions of more than 90 at.% Sb. In addition, because of the relatively high Sb vapor pressure, the crystal growth has to be carried out in closed ampoules, e.g. using the Bridgman method from a high-temperature solution. Unfortunately, using a vertical Bridgman arrangement we found a high amount of Sb-inclusions in the grown $FeSb_2$ and $CoSb_3$ crystals. Thus, in order to avoid mother liquid inclusion formation in these compounds we used a forced convection in the melt by tilting the Bridgman-type crystal growth setup (15° with respect to the horizontal direction) combined with an ampoule rotation (100 rpm along its axis). This new modification of the directional solidification principle was named as Inclined Rotary Bridgman (IRB) method.

Our results showed that the IRB method produced a better mixing of the melt compared to the other Bridgman arrangements due to the gravitational forces. Thus, the new technique, strongly minimizes the high risk of Sb-inclusion formation in the crystal growth of $FeSb_2$ and $CoSb_3$. These results were also corroborated with numerical modeling of the hydrodynamics of the melt by employing the commercial software package ANSYS-cfx and crysMAS. Further improvement was achieved when using a

native seed in the IRB method. Growing large single crystals of high quality with a size of approximately 15 mm in diameter and 15 mm in length could be achieved at the end of this study. Similarly, the ternary compounds $Fe_{1-x}Co_xSb_2$ and $In_xCo_4Sb_{12}$ with different Co and In doping concentrations were successfully grown as well. All the crystals were characterized by optical microscopy, X-ray powder diffraction (XRD), X-ray Laue backscattering, and electron probe microanalysis (EPMA). The influence of In doping on the electrical properties of $CoSb_3$ was also studied by means of a standard DC 4-probe technique.

Finally, it is worth mentioning that the advantage of this Inclined Rotary Bridgman method is not at all restricted to the Sb-based thermoelectric materials. Therefore, it may be a powerful approach in unidirectional solidification from off-stoichiometric melts, in general.

Chapter 1

Introduction

Energy consumption is a big challenge that is currently affecting our world. From the overall primary energy (e.g. gas, oil, coal) only about one third is effectively used and the rest is lost as heat during conversion processes in the industry (e.g. power engineering, chemical processing, metallurgy, transport) [1, 2]. Thus, in the recent decades, the development of sustainable technologies for the efficient use, conversion, and recovery of the waste heat has attracted considerable attention of governments and research institutes [3–5]. Within this context, devices made of thermoelectric (TE) materials, which can convert waste heat directly into electrical energy by the Seebeck effect or in the inverse process may be used for refrigeration by the Peltier effect [6–8], have been considered as a potential technology for waste heat harvesting [9–11]. The efficiency of the energy conversion process of a thermoelectric material (whether power generation or cooling) is generally evaluated by the dimensionless figure of merit, ZT,

$$ZT = \frac{S^2\sigma}{\kappa}T = \frac{S^2}{\rho\kappa}T \tag{1.1}$$

where S is the Seebeck coefficient (also known as thermoelectric power), σ is the electrical conductivity, $S^2\sigma$ is the power factor, ρ is the electrical resistivity, T is the absolute temperature, and $\kappa = \kappa_{lat} + \kappa_{ele}$ is the total thermal conductivity which is composed of lattice thermal conductivity κ_{lat} and electronic thermal conductivity κ_{ele} [7]. A good TE material demands to possess a high ZT, therefore, both the Seebeck coefficient S and the electrical conductivity σ must be large, while the thermal conductivity κ must be minimized. However, there are certain dependences among these quantities that prevents the easy improvement of ZT [12, 13], e.g., the Pisarenko relation

[14] limits the simultaneous enlargement of σ and S, and the Wiedemann-Franz law [15] requires the electronic contribution of the thermal conductivity κ_{ele} to be proportional to the electrical conductivity σ. Hence, the design of an effective TE material is restricted to maximize either the electronic transport $S^2\sigma$ or to minimize the lattice thermal conductivity κ_{lat} [16, 17].

In general, in bulk thermoelectric materials from intermetallic compounds (such as clathrates, half-Heusler alloys, skutterudites, and complex chalcogenides, etc.) [17] the optimization of ZT is being made by lowering κ_{lat} through alloying, doping, rattler atoms, nanostructuration, and solid solution formation [18, 19]. Particularly, there have been suggested various intermetallic compounds exhibiting figures of merit that exceed this one corresponding to classical PbTe, Bi_2Te_3, and SiGe alloys which are considered the best conventional thermoelectric materials at different ranges of temperature. Among them, Sb-based compounds like $FeSb_2$ and $CoSb_3$ as well as ternaries based on these materials are very attractive candidates (see Figure 1.1) [19–22]. The main advantages of the $FeSb_2$ and $CoSb_3$ compounds compared to the present ZT record holders are the better availability, less volatile, less toxicity, and lower price of the constituting elements.

An extremely high Seebeck coefficient (thermoelectric power) of approx. -45,000 μVK^{-1} at 10 K [23] and a new record high power factor of $\sim$ 8,000 $\mu WK^{-2}cm^{-1}$ at 23 K [24] were observed in the narrow band-gap semiconductor $FeSb_2$ (marcasite-like structure with space group *Pnnm* (No. 58)). However, this compound also presents a high thermal conductivity leading to a poor thermoelectric performance with a very small ZT value of 0.005 at 12 K [25]. Consequently, many efforts have been focused on the reduction of the lattice thermal conductivity of $FeSb_2$, specially, via substitution of various transition metals such as Cr and Co at the Fe site or chalcogenides (e.g. Se, S) at the Sb site [26–30].

The potential of the compound $CoSb_3$ as a thermoelectric material is mainly due to its skutterudite crystal type structure (cubic system with space group $Im\bar{3}$ (No. 204)) which has two large empty cages in its unit cell. Here, the guest atoms R (such as rare-earth metals, alkaline metals and/or alkaline-earth metals [31–38]) can be partially or completely filled, forming the so-called filled skutterudites $R_xM_4X_{12}$ (x is its filling factor). This type of structure lets $CoSb_3$ to present a *p*-type or *n*-type conductivity, and sometimes, both behaviors [39–43]. $CoSb_3$ also displays a good Seebeck coefficient (200 μVK^{-1}) at room temperature [44, 45]. In particular, the incorporation of indium atoms [46] to reduce the thermal conductivity has been intensively studied due to the possibility of these materials

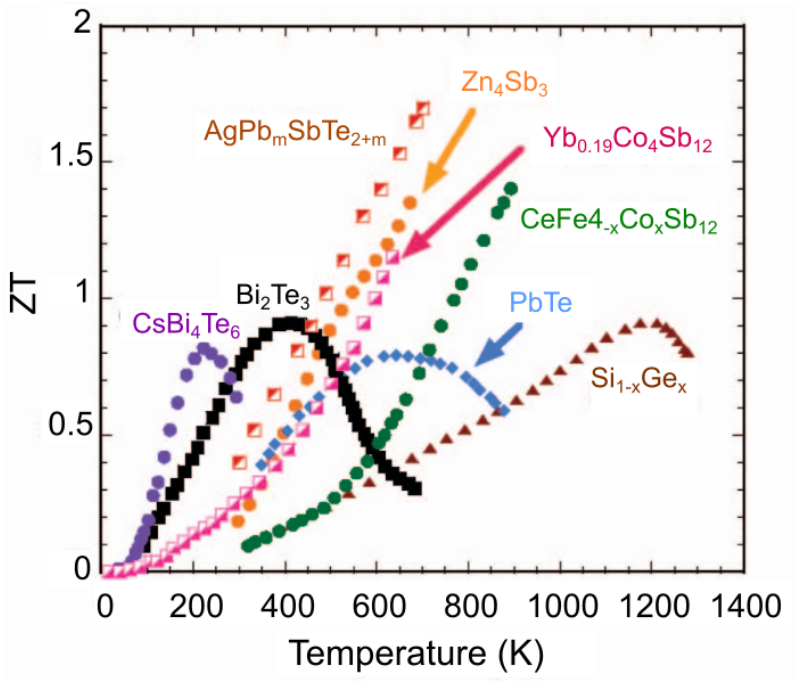

Figure 1.1: Temperature dependence of the figure of merit ZT for conventional (Bi_2Te_3 and PbTe) and novel thermoelectric materials, among them Sb-based compounds. Taken from [19].

to be used as high-temperature power generators, e.g., T. He *et al.* [47] obtained $ZT = 1.2$ at 575 K for $In_xCo_4Sb_{12}$ considering $x \leq 0.2$.

In this sense, there have been several attempts to grow single crystals of these binary and ternary compounds with the goal of improving their thermoelectric properties and having a better understanding of them. $FeSb_2$ and $CoSb_3$ are peritectically melting compounds with decomposition temperatures of 750 °C [48] and 874 °C [49], respectively. This means that they cannot be crystallized from congruent melts but have to be grown below the peritectic temperature from Sb-rich solutions of more than 90 at.% Sb. Also, crystal growth has to be carried out in closed ampoules due to the relatively high Sb vapor pressure. Thus, in the available literature, most of the authors have used what they call "self-flux method" or just "flux method" that can be traced back to Canfield and Fisk [50], and typically yields to mm-sized crystals [51, 52]. Directional solidification by the vertical Bridgman technique from Sb-rich solutions was also applied for $FeSb_2$ [53] and $CoSb_3$ [54] resulting in large-grained structures that allowed single crystal preparation. M. Kowasch [55] has recently tried to grow large-grained $FeSb_2$ from a three-phase initial ingot by

using the traveling heather method. Unfortunately, the majority of these works have not reported on the inclusion formation which is considered to be the most severe problem in high-temperature solution growth. A first attempt was done by M. Akasaka *et al.* [56], who suggested a post-growth annealing procedure which is more or less an evaporation of the second-phase Sb inclusions which is not applicable to single crystal preparation. Hence, this is still an open issue which needs more profound experimental and theoretical investigation. So far, it is only known that to avoid mother liquid inclusions crystal growth of both compounds has to be carried out extremely slowly and materials transport in the high-temperature solution has to be assisted by some technique of forced convection.

1.1 Objectives and outline

In the present thesis, we will use forced convection to avoid the formation of Sb-inclusions in the $CoSb_3$ and $FeSb_2$ single crystals. Since a strong mixing of the melt in closed ampoules is not easy to be obtained, a technique developed in our laboratory and named as Inclined Rotary Bridgman (IRB) method will be applied. This new modification of the directional solidification principle uses the gravitational forces in a tilted arrangement of the furnace-ampoule system. Additionally, native seeds will be used in the IRB experiments in order to grow oriented single crystals. To gain a deep insights into the experiments, numerical simulations of hydrodynamics in crystal growth will also be carried out using the software Ansys-cfx and crysMAS.

Once having succeeded in the growth of inclusion-free single crystals of the binary Sb-compounds from starting compositions Fe_9Sb_{91} and Co_7Sb_{93}, the second objective of this thesis is the incorporation of Co and In atoms into the crystal structures of $FeSb_2$ and $CoSb_3$, respectively. To do this, firstly, $Fe_{1-x}Co_xSb_2$ and $In_xCo_4Sb_{12}$ will be crystallized from starting compositions $(Fe_{1-x_0}Co_{x_0})_{0.10}Sb_{0.90}$ ($0.1 \leq x_0 \leq 0.5$) and $(In_{x_0}Co_{1-x_0})_{0.06}Sb_{0.94}$ ($0.05 \leq x_0 \leq 0.2$), respectively, by using a small-scale vertical Bridgman method. Once the optimal starting compositions are found for each case, the IRB growth experiments will be carried out with the ternaries compounds as well. All the grown single crystals will be structurally characterized by different experimental techniques. Electrical properties of $CoSb_3$ and In-doped $CoSb_3$ will also be studied.

The present work is structured as follows. In Chapter 2, the phase diagrams and structures of binary and ternary $FeSb_2$ and $CoSb_3$ compounds are discussed. Then, in

chapter 3, a brief description of the main aspects in the theory of crystal growth is given in order to understand the processes happening inside the ampoule. In Chapter 4, the experimental setups and equipments employed in the present thesis are described in details. The results for the $FeSb_2$ and $CoSb_3$ single crystals and their corresponding ternary compounds are shown and discussed in Chapter 5 and 6, respectively. Chapter 7 presents the numerical simulations carried out to understand the hydrodinamics of the melts in the different setups of the Bridgman method. Finally, the summary and outlook of the work are displayed in Chapter 8.

Chapter 2

Sb-based compounds

Following to the motivation given in the previous chapter, here, the binary (Fe-Sb and Co-Sb) and ternary (Co-Fe-Sb and In-Co-Sb) systems will be described in more detail. Their corresponding phase diagrams and crystal structures are also presented. Particularly, the discussion will be focused on the Sb-rich region of the phase diagrams.

2.1 The Fe-Sb system

2.1.1 Phase diagram

The binary Fe-Sb phase diagram has been first studied by H. Okamoto [57], and then reviewed by B. Pei et al. [58]. Further assessment and then re-investigation was performed by K. W. Richter *et al.* [49] in the range from 25 to 90 at.% Sb. Figure 2.1 shows the partial Fe-Sb phase diagram between 25 and 100 at.% Sb [49]. The Fe-Sb system has in total five solid phases: the Sb-rich region is characterized by two main intermetallic phases FeSb and $FeSb_2$ and one solid solution (Sb). In the Fe-rich region (not shown here), there are two terminal solid solutions of Sb in Fe, one in (αFe) and another in (γFe). Moreover, it can be seen from the phase diagram that the FeSb phase has a broad homogeneity range between about 40 and 48 at.% Sb.

Four invariant reactions occur in the Fe-Sb system: two eutectic reactions L $\rightleftharpoons$ (αFe) + FeSb and L $\rightleftharpoons$ $FeSb_2$ + (Sb) with eutectic composition of 33 at.% Sb and ~97 at.% Sb, respectively; one congruent melting point of FeSb which melts around 1025 °C at the

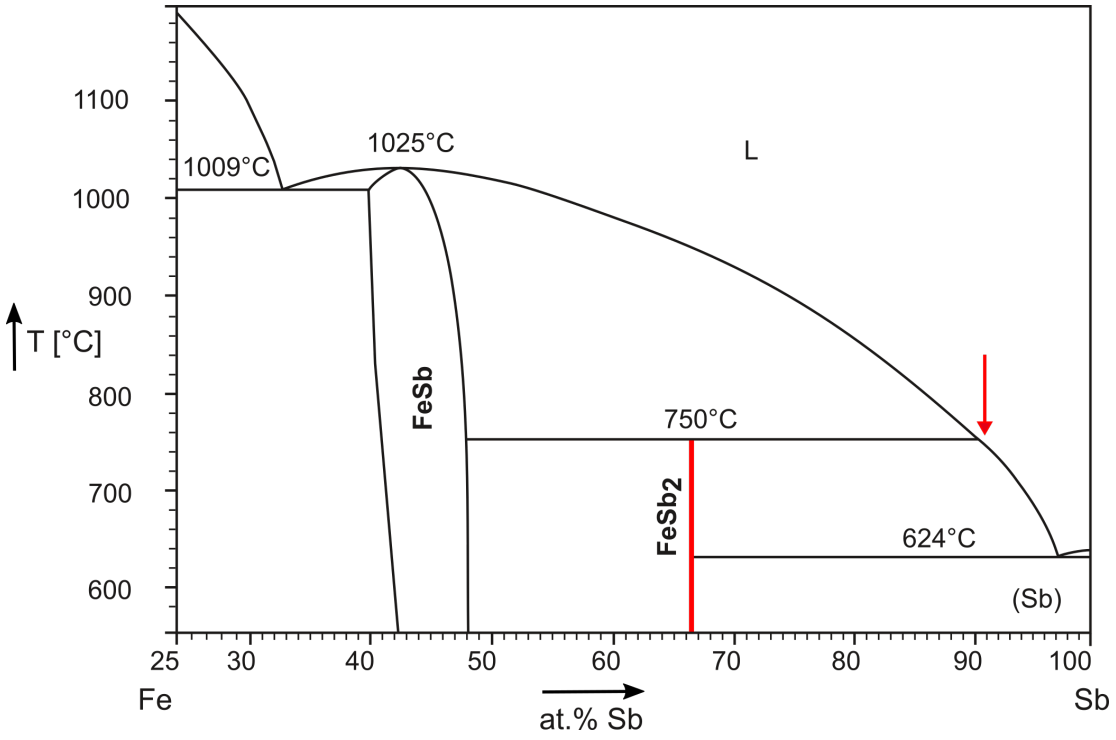

Figure 2.1: Fe-Sb binary phase diagram. Red arrow indicates the possible starting melt composition to obtain $FeSb_2$ compound. This figure has been adapted from Ref. [49].

composition of 43 at.% Sb; and one peritectic reaction,

$$\mathrm{FeSb} + L \rightleftharpoons \mathrm{FeSb_2} \qquad \text{at} \qquad T_P = 750\ ^\circ C \tag{2.1}$$

$FeSb_2$ is a line compound (red line in Figure 2.1) and the liquidus curve in the range 624 °C < T < 750 °C describes the equilibrium of $FeSb_2$ with an Sb-rich solution. Hence, $FeSb_2$ has to be grown below the T_P from Sb-rich solutions of more than 90 at.% Sb as indicated with the red arrow in the Fe-Sb phase diagram. However, due to the relatively high Sb vapor pressure that reaches 10^{-3} atm (=1.01325 mbar) at a temperature of 733 °C to 738 °C [59] (see Figure 2.2), crystal growth has to be carried out in closed ampoules, e.g. using the Bridgman method from a high-temperature solution. Consequently, more powerful techniques such as Czochralski growth [60] cannot be used if no additional tools like in the liquid-encapsulated technique are applied.

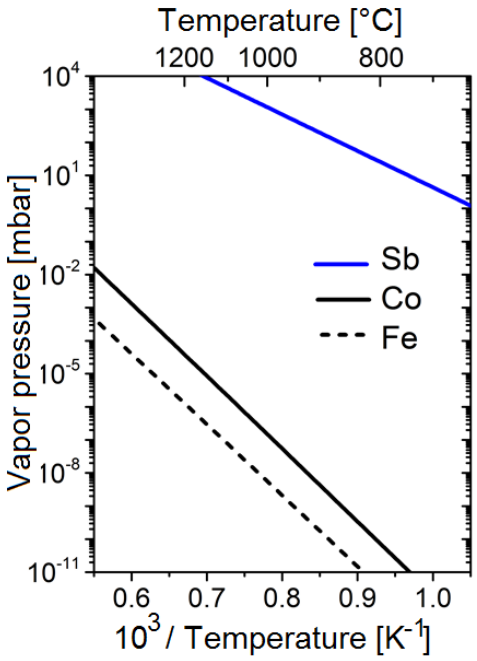

Figure 2.2: High vapor pressure of Sb compared to Fe and Co.

2.1.2 Crystal structures

(Sb)

Solid solution antimony, Sb, crystallizes in the trigonal crystal system with the space group $R\bar{3}m$ (No. 166). The unit cell dimensions are a = 4.3084(2) Å and c = 11.274(6) Å at a temperature of 298 K. Sb atoms occupy the Wyckoff position 6c (0, 0, 0.2338(5)) [61].

$FeSb_2$

$FeSb_2$ crystallizes in an orthorhombic structure with space group $Pnnm$ (No. 58) and Pearson symbol o$P6$. Its lattice parameters are a = 5.8328(5) Å, b = 6.5376(5) Å, and c = 3.1973(3) Å [62]. The unit cell contains two $FeSb_2$ formula units. Fe atoms occupy the Wyckoff position 2a (0, 0, 0) and Sb atoms 4g (x, y, 0), where x = 0.18885(2) and y = 0.3651(4). Figure 2.3 shows the crystal structure of $FeSb_2$ where Fe atoms are surrounded by six Sb atoms forming a distorted $FeSb_6$ octahedron. The corner of these octahedra are linked together in the ab-plane.

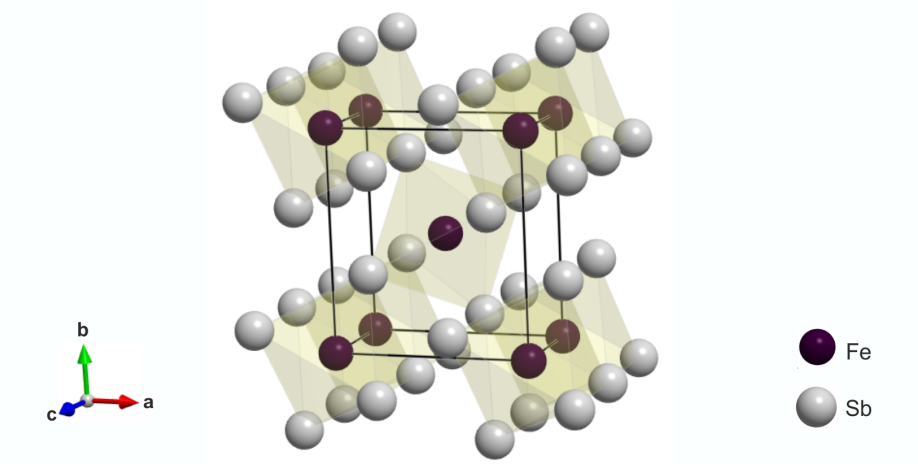

Figure 2.3: Crystal structure of the orthorhombic $FeSb_2$ phase where Sb atoms are positioned at the corners of $FeSb_6$ octahedra. The graph has been designed using VESTA software [63].

2.2 The Co-Fe-Sb system

The thermodynamic description of the Co-Fe-Sb ternary system was first reported by Y. Zhang *et al.* [64] and later improved by Ch. Li *et al.* [65]. These works were mainly based on the literature available for Co-Fe, Co-Sb and Fe-Sb systems [48, 49, 66]. In Figure 2.4, one can see that the liquidus projection of the Co-Fe-Sb system shows six primary crystallization regions [65]: four phases that form via peritectic reactions (γ(A1), $\alpha(A2)$, β, ξ) and two phases that form during eutectic reactions (η, Sb), which are described as

- γ(A1), Solid solution based on (Co,Fe) or (Co,Sb) with FCC-A1 structure.
- α(A2), Solid solution based on the disorder phase (Co,Fe) or (Fe,Sb) with BCC-A2 structure.
- β, Continuous solid solution based on β(CoSb) and β(FeSb).
- ξ, Linear stoichiometric compound based on $CoSb_2$ and $FeSb_2$.
- η, Linear stoichiometric compound based on $\eta CoSb_3$ with partial substituion of Fe for Co.
- Sb, Pure Sb with no solubilities of Co and Fe .

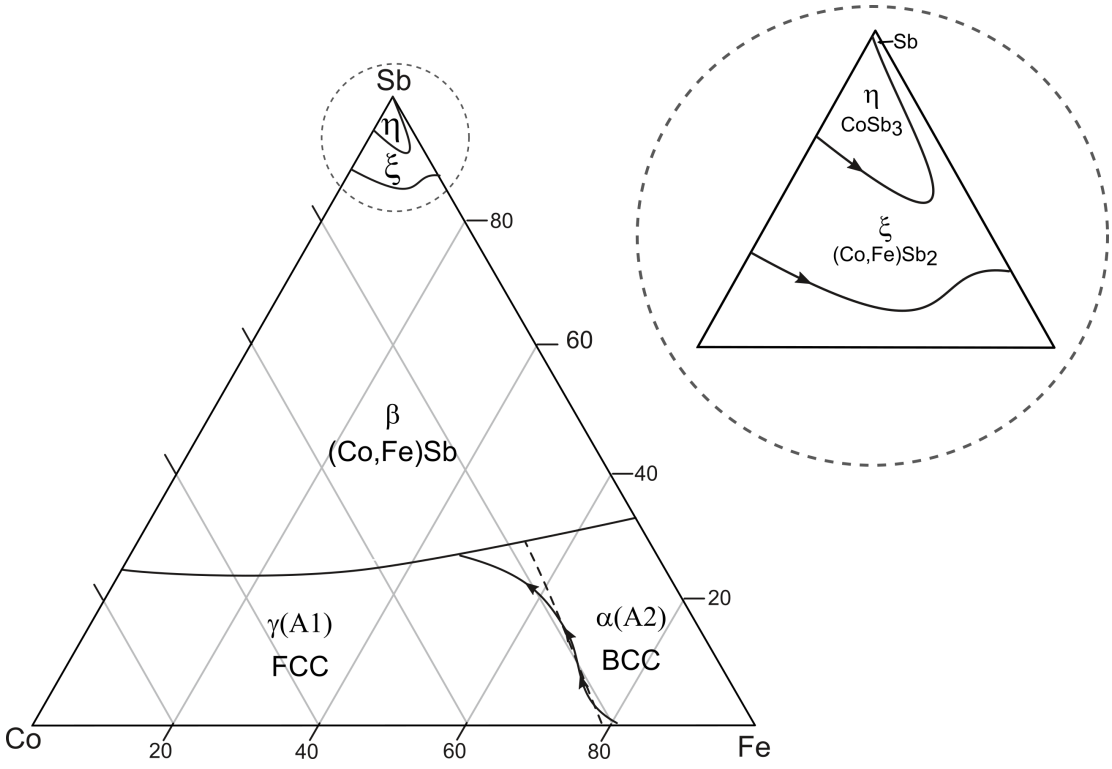

Figure 2.4: Liquidus projection of the ternary Co-Fe-Sb system illustrating the six primary crystallization regions. Dotted circle shows a magnification of the Sb-rich region which is the main target in the present work. Adapted from Ref. [65].

2.3 The Co-Sb system

2.3.1 Phase diagram

The most recent phase diagram for the binary Co-Sb system has been published by H. Okamoto [48] (see Figure 2.5). This phase diagram is based on the work done by K. Ishida and T. Nishizawa [67] and G. Hanninger [68]. Seven solid phases are known to be present in the whole composition range of the Co-Sb system: (i) two solid solution phases (αCo) and (ϵCo) in the Co-rich side, (ii) four intermetallic compounds (β-CoSb, γ'-$CoSb_2$, γ-$CoSb_2$, δ-$CoSb_3$), and one solid solution (Sb) in the Sb-rich side.

In the Co-Sb phase diagram there is one congruently melting phase, CoSb, and two peritectically melting compounds, $CoSb_2$ and $CoSb_3$. CoSb forms at 1220 °C from a congruent melt and has a wide homogeneity range between 43.5 - 52 at.% Sb [48], 48 - 51 at.% Sb [67], or 46 - 52.5 at.% Sb [68]. $CoSb_2$ decomposes peritectically at 936 °C

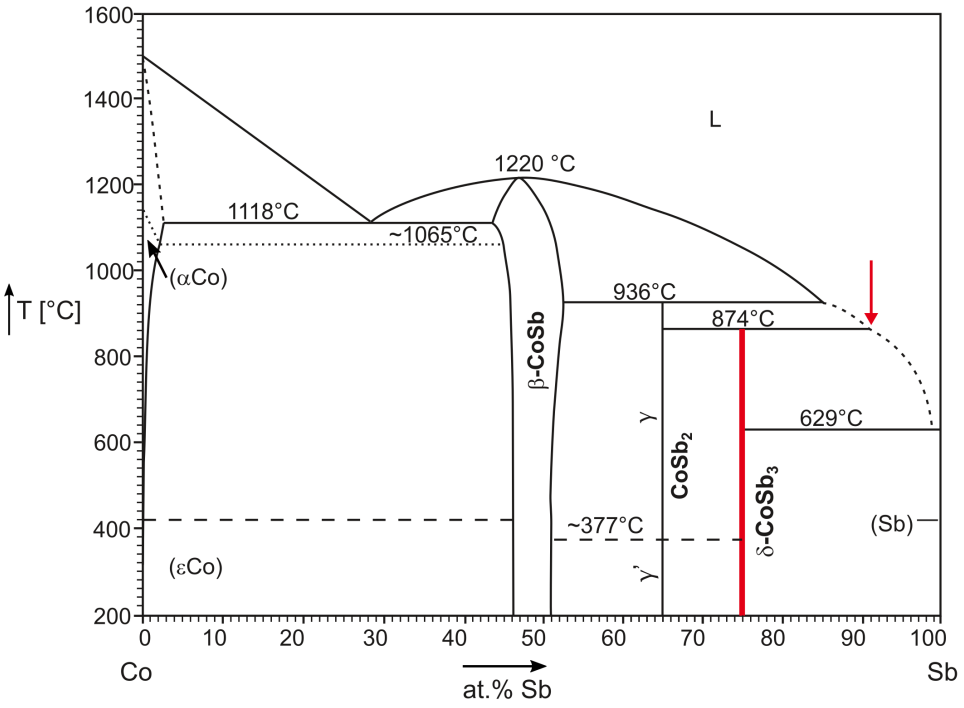

Figure 2.5: Phase diagram of the binary Co-Sb system. Dotted parts of liquidus and solid curves indicate the not well determined solubility lines, horizontal dashed lines denote the structural phase transitions for Co and $CoSb_2$, and dashed lines point the magnetic transitions at Curie temperature. Red arrow highlights the possible starting melt to grow the $CoSb_3$ phase. This figure has been adapted from Ref. [48].

($CoSb_2 \rightleftharpoons CoSb + L$). Additionally, this compound undergoes a structural phase transition from orthorhombic structure (γ-phase) at high temperature to the monoclinic structure (γ'-phase) at low temperature (~377 °C) [69].

In the case of the $CoSb_3$ compound, represented as a line compound (red line), the following peritectic reaction takes place,

$$CoSb_2 + L \rightleftharpoons CoSb_3 \qquad \text{at} \qquad T_P = 874\,^{\circ}C \tag{2.2}$$

Similar to $FeSb_2$ (see Section 2.1), the liquidus curve 629 °C < T < 874 °C describes the equilibrium of $CoSb_3$ with an Sb-rich solution. Hence, like $FeSb_2$, $CoSb_3$ has to be grown below the T_P from Sb-rich solutions of more than 91 at.% Sb as indicated with the red arrow in the Co-Sb phase diagram.

2.3.2 Crystal structures

CoSb

The crystal structure of the intermetallic CoSb exhibits a hexagonal (NiAs type) space group $P6_3/mmc$ (No. 194) and Pearson symbol $hP4$. Its unit cell parameters are $a = 3.880(4)$ Å and $c = 5.172(8)$ Å. The density ρ is 8.90 g/cm^3. In Figure 2.6(a) one can see that 6 Co (neighbor) atoms are arranged in a trigonal prism around Sb. Here, Co atoms occupy the Wyckoff position $2a$ (0, 0, 0) and Sb atoms the position $2c$ (1/3, 2/3, 1/4) [70].

$CoSb_2$

Regarding $CoSb_2$ compound, only the high temperature γ-phase will be considered in this work. $CoSb_2$ has a monoclinic structure with space group $P2_1/c$ (No. 14) and Pearson symbol $mP12$. Its unit cell parameters are $a = 6.5077(3)$ Å, $b = 6.3879(4)$ Å, $c = 6.5430(3)$ Å, $\beta = 117.660(4)^\circ$ [71]. Sb atoms form a polyhedron with Co atom in the center, as it can be seen in the Figure 2.6(b). Co atoms occupy the Wyckoff position $4e$ (0.27, 0, 0.28), while Sb atoms occupy the positions $4e$ (0.35, 0.354, 0.168) and $4e$ (0.162, 0.638, 0.368), named as Sb1 and Sb2 respectively.

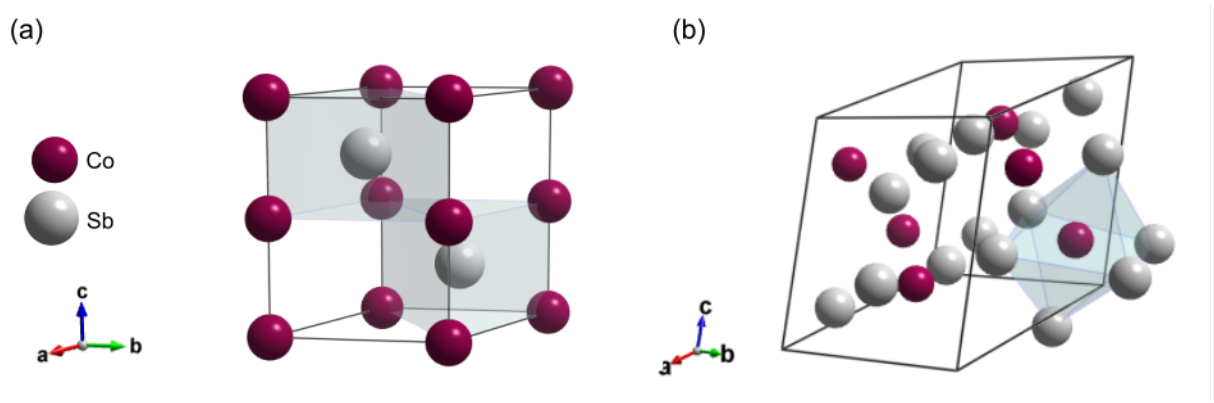

Figure 2.6: Crystal structures of (a) the hexagonal CoSb and (b) the monoclinic $CoSb_2$ compound. The trigonal prism around Sb atoms and $CoSb_6$ polyhedra are highlighted for each crystal structure. The graphs have been designed using VESTA software [63].

$CoSb_3$

$CoSb_3$ is the skutterudite-$CoAs_3$ phase of the binary skutterudites. The general formula of the skutterudite compounds is MX_3 where M corresponds to a transition metal atom from the group 9 (Co, Rh, Ir) and X to a pnictogen atom from the group 15 (P, As, Sb). These compounds crystallize in a body-centered cubic structure with space group $Im\bar{3}$ (No. 204) and Pearson symbol $cI32$. In particular, $CoSb_3$ compound has a lattice parameter $a = 9.0385(5)$ Å, and each Co atom is octahedrally surrounded by Sb atoms forming a tilted $CoSb_6$ octahedron, see Figure 2.7(a). Co atom is located on the Wyckoff position $8c$ (1/4, 1/4, 1/4) and Sb atoms occupy the position $24g$ (0, 0.33537, 0.15788).

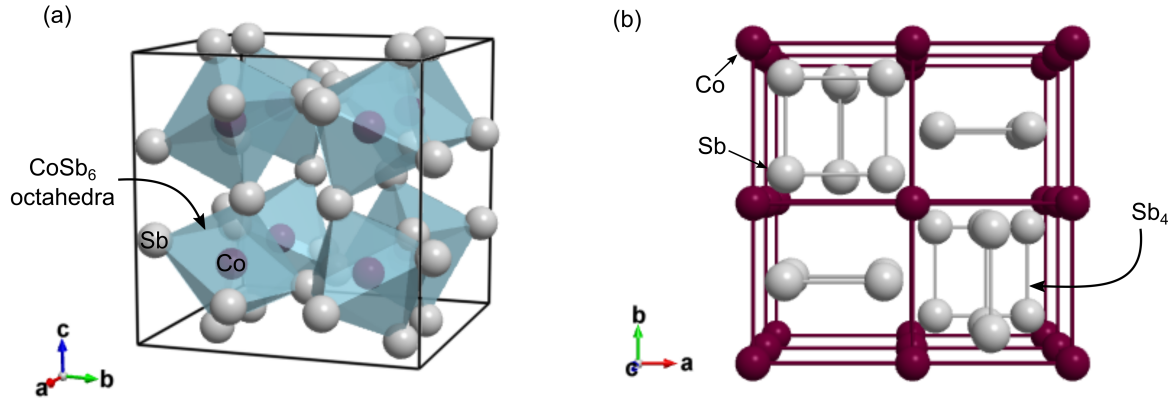

Figure 2.7: Different representations of the crystal structure of $CoSb_3$ (a). Polyhedral representation: Co atoms surrounded by Sb atoms forming eight tilted $CoSb_6$ octahedra (shown in light blue). (b) Ring representation: top view of the $CoSb_3$ structure parallel to the crystallographic c-axis which illustrates the Sb_4 rings. The graphs have been designed using VESTA software [63].

Furthermore, the cubic framework of Co in the $CoSb_3$ structure consists of eight small cubes in the unit cell, where six of them are centered by Sb_4 rings (almost square). Each Sb_4 ring is mutually perpendicular to its neighbor rings and parallel to the cubic crystallographic axes (see Figure 2.7(b)). The distances between two neighboring Sb atoms are 2.9854 Å and 2.976 Å [72]. The remaining two small cubes are empty cages with sufficient size to accommodate a guest atom (filler) R with an ionic radius lower than the cage radius (see Figure 2.8(a)).

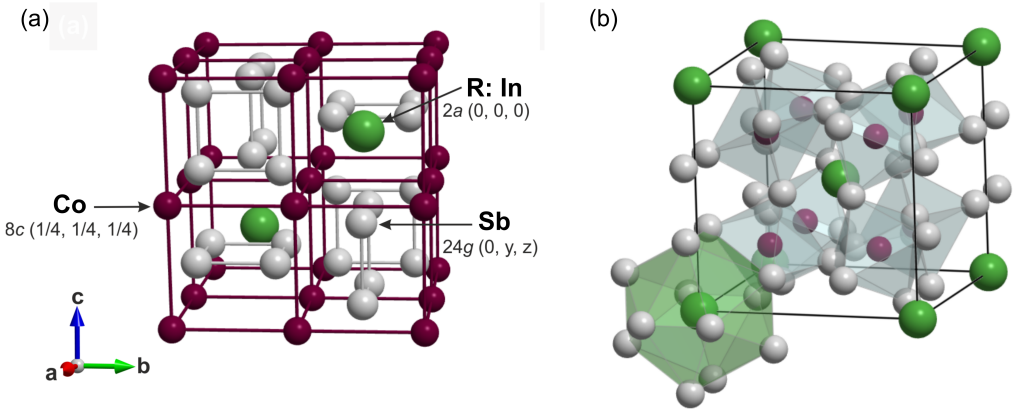

Figure 2.8: Different representations (origin shifted) of the filled-skutterudite structure with general formula RCo_4Sb_{12}. (a) Wyckoff position of each atom is indicated. (b) The filler atom, R, is enclosed in a cage formed by Co_8Sb_{12} dodecahedron (shown in green color) and the Co atoms by a $CoSb_6$ octahedron (shown in light blue color). The graphs have been designed using VESTA software [63].

Thus, when a third kind of atom is incorporated into the cage the chemical formula of the skutterudite compounds becomes $R_xM_4X_{12}$, where x defines the filling fraction and ranges between 0 and 1. This generates a so-called *filled skutterudite*. The filled skutterudite shares similar crystal structure with the binary skutterudite and is characterized by large lattice constants a = 7.8 - 9.3 Å. The filler atom R is located at the position $2a$ (0, 0, 0), the transition metal M at $8c$ (1/4, 1/4, 1/4), and the pnictogen X occupies the position $24g$ (0, y, z) where the parameters y $\sim$ 0.35 and z $\sim$ 0.16 depend on the particular chemical composition. The variation in the values of y and z is due to the fact that the pnictogen rings are not perfect squares and that the MX_6 octahedron is distorted. Each R atom is the center of an dodecahedron and is surrounded by 12 nearest X-atoms (see Figure 2.8(b)). The filler atoms R can be usually rare-earth metals, alkaline metals and/or alkaline-earth metals [31]. These filler elements have different physical and chemical characteristics (e.g., electronegativity, ion valence, and ionic radius), showing different filling adaptability and different influence on the thermoelectric properties. In particular, for the $R_xCo_4Sb_{12}$ base compound, many researchers focused on filling the cage with different atoms such as Ba, Ca, Ce, Yb, among others [32–38]. However, up to our knowledge, limited work has been reported by using In atoms as filler ones. This is one the main scientific goals of the present work.

2.4 The In-Co-Sb system

For the $In_xCo_4Sb_{12}$ compound, there are two main aspects that still generate controversy: (*i*) occupancy of the empty cages, Co sites or Sb sites and (*ii*) the solubility limit of In in $CoSb_3$. Thus, because of the relatively small ionic radius of indium In^{3+} (0.76, 0.94 and 1.06 Å with coordination numbers 4, 6 and 8, respectively), in comparison with the void size in $CoSb_3$ which is around 1.9 Å, the In atoms may move out from the cage site due to, e.g., thermal vibrations at a finite temperature. Based on this assumption, and knowing the electronegativity difference between In and Sb, X. Shi *et al.* [38] theoretically concluded that In atoms can not occupy the voids of the $CoSb_3$ structure. However, performing a similar study, K. Akai *et al.* [73] found that In atoms can be used as filler atoms in this compound. Besides this theoretical contradiction, there is also some discrepancy in experimental results regarding In-filled $CoSb_3$ materials. T. He *et al.* [47] reported that the filling fraction limit of In in the $CoSb_3$ structure was $x\sim$ 0.22 (i.e., $In_{0.22}Co_4Sb_{12}$), and that there has been a secondary phase InSb in the sample with nominal composition $In_{0.25}Co_4Sb_{12}$. This result was later corroborated by Y. Du *et al.* [74]. On the contrary, R. M. Mallik *et al.* [75, 76] reported the synthesis of the $In_xCo_4Sb_{12}$ ($0 \leq x \leq 0.3$) compound but without any secondary phase.

These previous studies provided a limited knowledge of thermodynamic equilibrium phases of the In-Co-Sb ternary system [47, 75, 76, 78]. Consequently, A. Grytsiv *et al.* [79] constructed the first phase diagram for the In-Co-Sb system in the range from 375 °C to 800 °C. They identified two solubility limits of In $x = 0.22$ and $x = 0.09$, which depend on the Co/Sb ratio. The maximum solubility $x = 0.22$, that is consistent with [47], is found when the compound is in equilibrium with $CoSb_2$ and InSb. When the compound coexists in equilibrium with InSb and (Sb) the solubility is reduced to $x = 0.09$. More recent assessments of the In-Co-Sb ternary phase diagram were published by Y. Tang *et al.* [77] and, most recently, by S. Tseng *et al.* [80]. They provided the isothermal section at 850 °C and 650 °C, their respective equilibrium phases, and the liquidus projection of the In-Co-Sb system. In particular, Y. Tang *et al.* [77] determined the phase diagram of the In-Co-Sb system near the $CoSb_3$ phase region, as it can be seen in Figure 2.9. It was also reported an increment of the maximum solubility to $x = 0.27$ due to the stability of In in dual sites, i.e., in the cage site and at Sb site.

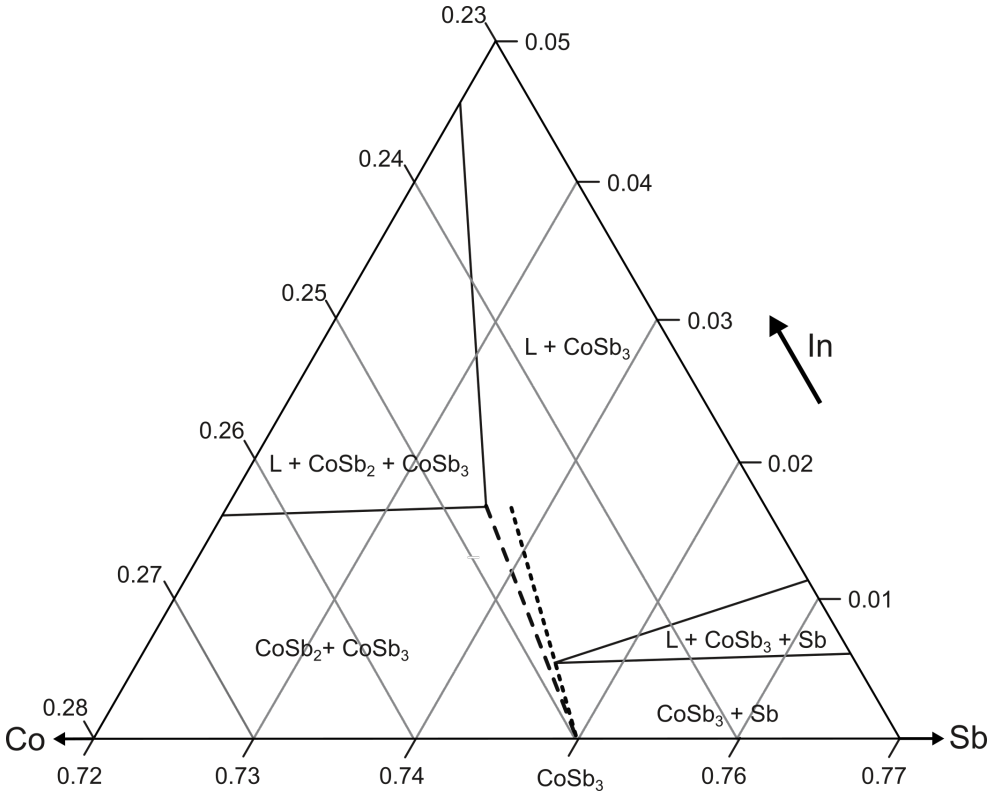

Figure 2.9: Isothermal section of a tiny part of the In-Co-Sb phase diagram at 600 °C enlarged near $CoSb_3$. The region of indium solubility is extended in the direction of $In_{2x/3}Co_4Sb_{12-x/3}In_{x/3}$ (dashed line) and $In_xCo_4Sb_{12}$ (dotted line) up to $x = 0.27$. This figure has been adapted from Ref. [77].

Chapter 3

Theory of crystal growth

In this chapter, the basic theories of nucleation and crystal growth are briefly discussed. This will help us to have a better understanding of the results obtained in this work which will be presented in the next chapters. Thus, the first section presents the thermodynamics of nucleation, whereas the second section deals with the kinetics of both processes.

3.1 Thermodynamics and nucleation

Growth of single crystals can be considered as a phase transformation into an specific solid phase from any other phase. In dealing with phase transformations at constant pressure, thermodynamics describes the behavior of Gibbs free energy G of all possible phases with respect to the temperature. For example, if a liquid (melt or solution) is undercooled below the melting temperature by a temperature variation of ΔT, there will be a decrease in the free energy $\Delta G = G^l - G^s$ upon crystallization, as shown in Figure 3.1.

This reduction in free energy ΔG provides the driving force for crystallization. Knowing that the Gibbs free energy is defined in terms of the enthalpy H and the entropy S of each phase, the change of energy per unit volume, ΔG_v, as a function of the temperature T is expressed as,

$$\Delta G_v = \Delta H - T\Delta S \; . \tag{3.1}$$

At the equilibrium melting temperature T_m, the Gibbs free energy is the same for both, liquid and solid phases, i.e., $\Delta G = 0$. Consequently, $\Delta G_v = \Delta H_m - T_m \Delta S_m = 0$. This

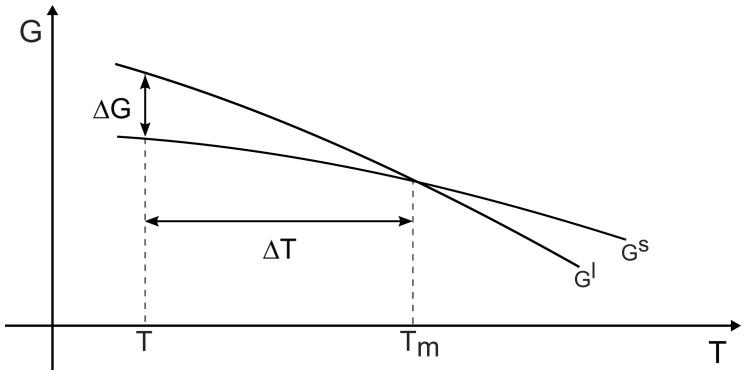

Figure 3.1: Free energy of a pure component as a function of temperature for solid and liquid phases. The change of free energy ΔG indicates the decrease in free energy due to undercooling of the melt.

implies that,

$$\Delta G_v = \Delta H_m - \frac{T}{T_m}\Delta H_m = \frac{\Delta H_m}{T_m}\Delta T \ . \tag{3.2}$$

where ΔH_m is the latent heat of crystallization and $\Delta T = T_m - T$ is called undercooling, with T_m being the melting temperature and T the actual temperature. The liquid phase becomes supersaturated when T decreases below T_m ($T < T_m$). Hence, the undercooling represents the thermodynamics driving force for the change of state, from liquid (melt or solution) to solid phase, and is also known as supersaturation.

For the formation of a three-dimensional (3D) nucleus of a new phase an interface must be formed. This starts with the formation of a small cluster of the solid phase within the liquid phase (melt or solution). This process is called nucleation, where nuclei of a new phase may appear or disappear as a result of statistical fluctuations. Depending on the degree of supersaturation there is always a certain statistical probability that some neighboring particles gain sufficient energy necessary to form a stable nuclei of the crystalline phase. Three types of nucleation are generally distinguished: primary nucleation, which can be either homogeneous or heterogeneous, and secondary nucleation. *Homogeneous nucleation*, happens spontaneously where nuclei are formed within the liquid without any aid of an external factor. *Heterogeneous nucleation*, is induced by foreign particles where nuclei are formed on some pre-existent external surface (e.g., impurity particles, ampoule wall) which acts as a substrate for the formation of the nuclei.

3.1.1 Homogeneous nucleation

As mentioned earlier, the formation of a nucleus is accompanied by the appearance of an interface between the mother phase and the new phase. A specific energy is needed to form this interface based on the surface energies of the two phases. Nucleation was treated from thermodynamic viewpoint by M. Volmer and A. Weber [81]. In a supersaturated homogeneous solution, the change of Gibbs free energy necessary to form a new solid nucleus of volume V_s with a surface area A_s can be written as the contribution of two energies (see Figure 3.2(a)): (i) to form the volume (bulk) of the new phase and (ii) to build up an interface:

$$\Delta G = -V_s \Delta G_v + A_s \gamma_{sl} \ . \tag{3.3}$$

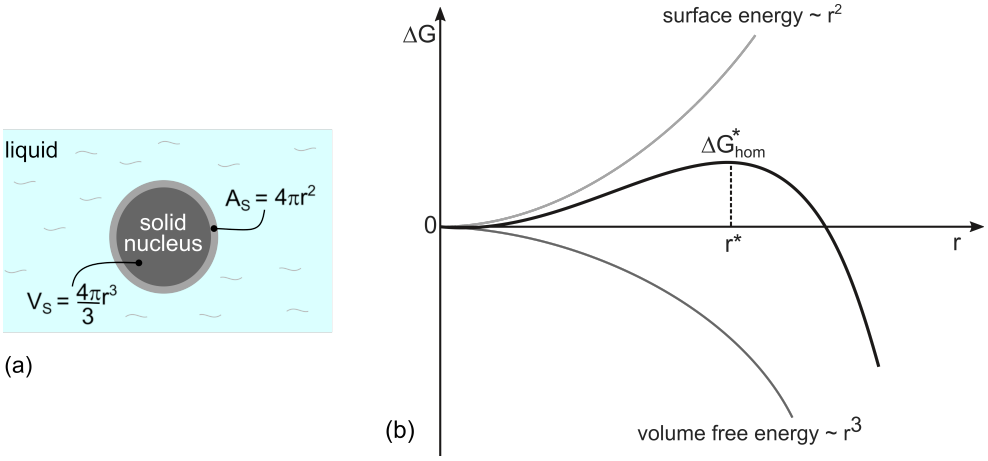

Figure 3.2: (a) Formation of a spherical nucleus of radius r within the liquid phase. (b) Free energy change ΔG for homogeneous nucleation as a function of the nucleus radius, r. Contribution of both surface and volume energies to ΔG are also shown. Only those nuclei which radius is greater than r^* and overcome ΔG^*_{hom} grow into crystal.

The negative term expresses that the volumes contribution lowers the free energy, while the surface of the nucleus increases the total. Considering a spherical nucleus of radius r, ΔG is given by

$$\Delta G = -\frac{4}{3}\pi r^3 \Delta G_v + 4\pi r^2 \gamma_{sl} \ , \tag{3.4}$$

where ΔG_v is the Gibbs free energy change per unit volume and γ_{sl} is the interfacial free energy between the nucleus (s: solid) and the melt (l: liquid). Figure 3.2(b) shows

the contribution of the two free energy curves as a function of r as well as the sum of both. Notice that the contribution from the surface energy varies as r^2 while the contribution from the free energy of the bulk phases varies as r^3. This implies that if the nucleus has a small radius, the surface energy dominates and the overall free energy actually increases due to the formation of the solid nucleus. The free energy change ΔG increases with radius r until a maximum r^* is reached. Thus, for a given value of undercooling ΔT, the critical nucleus radius r^* can be obtained from $d(\Delta G)/dr = 0$:

$$r^* = \frac{2\gamma_{sl}}{\Delta G_v} \tag{3.5}$$

and the corresponding energy barrier or action energy:

$$\Delta G^*_{hom} = \frac{16\pi\gamma^3_{sl}}{3\Delta G^2_v}. \tag{3.6}$$

If $r < r^*$, the nucleus is unstable and dissolves in order to lower its free energy; whereas if a nucleus is equal or larger $r \geq r^*$, spontaneous growth occurs. By substituting ΔG_v in Equations (3.5) and (3.6), the critical nucleus and activation energy can be also written in terms of the undercooling ΔT:

$$r^* = \left(\frac{2\gamma_{sl}T_m}{\Delta H_m}\right)\frac{1}{\Delta T} \tag{3.7}$$

$$\Delta G^*_{hom} = \left(\frac{16\pi\gamma^3_{sl}T^2_m}{3\Delta H^2_m}\right)\frac{1}{\Delta T^2}\ . \tag{3.8}$$

Therefore, these quantities can be controlled by the melting temperature T_m, undercooling ΔT, and interfacial energy γ_{sl}. In particular, the activation energy rapidly decreases after increasing the undercooling ΔT, i.e., undercooling plays an important role in the homogeneous nucleation. Any process that modifies these parameters will have an effect on the possible viability of the nucleation process.

3.1.2 Heterogeneous nucleation

In heterogeneous nucleation the critical nucleus is not formed directly in the liquid phase (melt or solution), but on a existing substrate like the surface of an impurity particle or at the ampoule walls. Therefore, in first approximation, the heterogeneous nucleus is considered to be a spherical cap of the nucleating solid on a flat surface. The cap

represents a segment of a sphere with radius of curvature r and obeys the equilibrium condition expressed by the Young relation:

$$\gamma_{lS} = \gamma_{sS} + \gamma_{sl} \cos\vartheta \tag{3.9}$$

where γ_{lS}, γ_{sS}, and γ_{sl} are the interfacial free energies between the liquid-Substrate, solid-Substrate, and solid-liquid, respectively; with ϑ being the contact angle (see Figure 3.3).

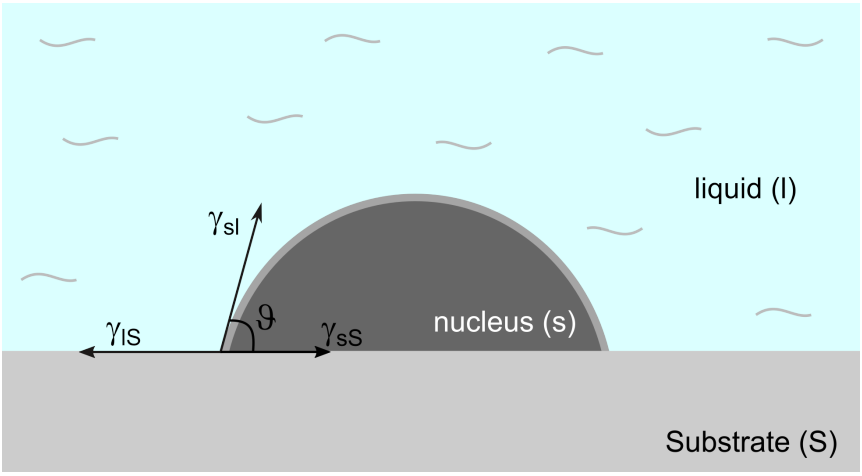

Figure 3.3: Spherical cap-shaped nucleus of radius r of the solid crystalline phase (s) on a foreign substrate (S), within a liquid solution (l). The interface energies γ are also shown which define the contact angle ϑ in the heterogeneous nucleation.

The change of free energy for the formation of a heterogeneous nucleus of radius r on the substrate is governed by,

$$\Delta G_{het} = -V_s \Delta G_v + A_{sl}\gamma_{sl} + A_{sS}\gamma_{sS} - A_{sS}\gamma_{lS} \tag{3.10}$$

where A_{sl}, A_{sS}, and A_{lS} are the surface areas between the solid-liquid, solid-Substrate, and liquid-Substrate, respectively. Replacing Equation (3.9) in the above expression results in

$$\Delta G_{het} = \left(-\frac{4}{3}\pi r^3 \Delta G_v + 4\pi r^2 \gamma_{sl}\right) f(\vartheta) \tag{3.11}$$

with

$$f(\vartheta) = \frac{1}{4}(2 + \cos\vartheta)(1 - \cos\vartheta)^2. \tag{3.12}$$

The function $f(\vartheta)$ is known as a shape factor and is purely dependent on the contact angle. $f(\vartheta)$ is always smaller than 1 for every contact angle $\vartheta < 180°$. Thus, the activation energy for heterogeneous nucleation can be written as,

$$\Delta G^*_{het} = \Delta G^*_{hom} \cdot f(\vartheta), \qquad 0 \leq f(\vartheta) \leq 1. \tag{3.13}$$

Here, it becomes clear that the heterogeneous nucleation requires less activation energy than the homogeneous nucleation. However, the critical radius remains the same as for the homogeneous nucleation, see Equation (3.5). It is also obvious from Figure 3.3 that the volume of a heterogeneous nucleus of critical size r^* is smaller than that of a homogeneous nucleus of the same critical radius.

Thus, from Equations (3.9) and (3.13), the nature of the heterogeneous nucleation can be determined by the contact angle ϑ, indicating three interesting cases:

- $\vartheta = 180° \Rightarrow \Delta G^*_{het} = \Delta G^*_{hom}$; this case is equivalent to homogeneous nucleation, i.e., the nucleus has no affinity for the substrate.
- $0° < \vartheta < 180° \Rightarrow \Delta G^*_{het} < \Delta G^*_{hom}$; the nucleation is easier to achieve because the overall excess free energy required is less than that for homogeneous nucleation.
- $\vartheta = 0° \Rightarrow \Delta G^*_{het} = 0$; there is no nucleation barrier, i.e., no nuclei have to be formed in the solution. An example is when the crystal itself is the substrate (equivalent to crystal growth on a seed).

3.2 Crystal Growth

The crystal growth process begins once a solid nucleus of the crystal is formed, either by homogeneous nucleation or heterogeneous nucleation. These processes are determined by mass and heat transport and by the intrinsic kinetic processes [82, 83]. In general, the stages that lead to the formation of a crystal can be thought to consist of the following steps:

- Transport of growth units in solution.
- Adsorption of growth units on the surface of the growing crystal.

- Diffusion of growth units on the surface.
- Attachment of growth units to surface site.

These four processes can be classified into two distinct categories. The first process belongs to the transport process category, while the rest belongs to the surface process category. Since these steps usually proceed in a sequential manner, the slowest of the four processes will govern the overall crystal growth and is called the rate-limiting step. For instance, if the first step is the slowest one, the crystal growth process can be considered as transport-controlled. On the contrary, if any of the other three processes are slower than the first one, the growth is kinetically controlled [84].

3.2.1 Kinetic processes and growth mechanisms

The first approach to understand the crystal growth process is using the most simple model to describe a crystal which is well known as Kossel crystal [85]. This model considers the crystal as a periodic arrangement of small cubic blocks. These may represent single atoms, ions, or molecules. According to the Kossel model there are different growth sites (or positions) with distinct binding energies (attachment energy) based on the number of nearest neighbors [86]. Figure 3.4 shows some of these sites such as the step (or ledge) and a kink site positioned within the terrace, and the ad-site on a surface.

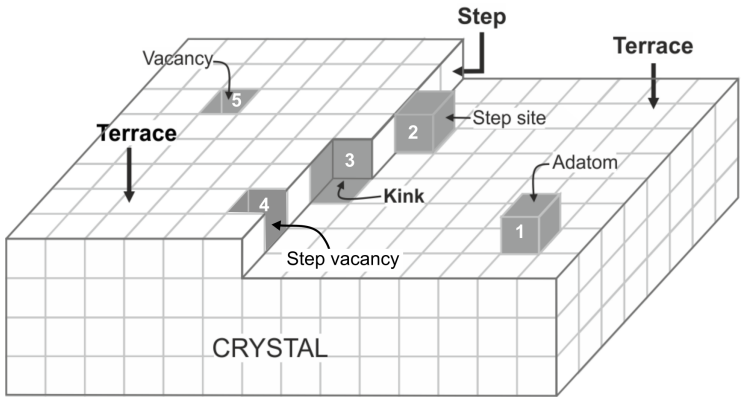

Figure 3.4: Surface of a simple cubic crystal (Kossel crystal) showing some possibilities of capture sites of atoms on the surface of a growing crystal. Building units at the surface may have one, two, three, four or five bonds. The kink position plays an important role in the growth process.

Thus, if a building unit is attached on top of the terrace (e.g., an isolated adsorbed atom or adatom), it will form one bond, which is directly beneath it. Likewise, the atom attached into the step site has two bonds, one below and the other on the side. However, Kossel [85] and Stranski [86] recognized, simultaneously and independent from each other, the importance of the unique position on the crystal surface known as a kink. For example, in case a building unit is incorporated in the kink site, three bonds would be formed. This means that exactly one half of the bonds are attached at the already existing crystal being by far the best position. Apart from the high gain in free energy that is obtained from the attachment at a kink position, its repeatability makes the kink position decisive for crystal growth. The kink position is also known as *repeatable step* (Kossel) and *Halbkristallage* (Stranski). All other alternative sites would qualitatively change the surface. Particularly, the highest gain in free energy of the vacancy site is favorable with five bonds but is non-repeating.

The Jackson factor α

From the above discussion, the atomic structure of the crystalline surface (i.e., the number of kink sites) plays an important role in the growth kinetics. The density of kinks on the interface depends on the roughness of the crystal surface, which is an intrinsic property of the crystal surface at equilibrium. K. A. Jackson [87] described the various states of surface roughness with the occupation factor x of surface sites being the ratio of the number of occupied positions to the total number N of sites at the surface. The Helmholtz free energy change ΔF of the contribution of a specific surface (hkl) is given by,

$$\Delta F = N k_B T \left[x(1-x)\alpha + x \ln x + (1-x)\ln(1-x) \right] \tag{3.14}$$

with

$$\alpha = \frac{\Delta H_{trans}}{k_B T} \xi_{hkl} \tag{3.15}$$

with k_B as the Boltzmann constant, T the temperature at the surface, ΔH_{trans} the transition latent heat, and ξ_{hkl} is an anisotropic factor, calculated from the ratio of bonds within the surface (hkl) compared to all bonds of growth units in the crystal. Thus, whether an interface is atomically smooth (flat) or atomically rough, can be determined by the value of α known as the Jackson factor. Accordingly, the interface will be atomically rough for $\alpha < 2$, i.e., it will have a large number of kink sites that allow the

easy attachment of crystallizing building units. On the contrary, if $\alpha > 2$, the interface is almost atomically smooth (flat or facet), i.e., there are no kinks.

The Kossel-Stranski-Volmer theory

The classic step growth theory was developed by Kossel, Stranski, and Volmer [88]. They found that the crystal surface on the atomic scale is not smooth, and any discontinuity allows sites for nucleation thus for the crystal growth. According to KSV model, crystal growth takes place by the adsorption of matter, which is produced layer by layer on the crystal surface. In a growing phase the building units collide with the surface, diffuse, migrate and, finally, get absorbed onto the sites where its energy becomes minimum. The adsorbed atoms (adatoms) will migrate over the surface randomly until they get either absorbed at a suitable position or detached from the surface, i.e., they return into the mother phase. Figure 3.5(a) shows the possible attachment sites for the adatoms at the growth surface: terrace, step, and kink site. As mentioned before, the binding energy is maximum for adatoms at the kink site. Consequently, the adatoms on the crystal surface migrate towards a step and move along it to a kink site and get incorporated. This step growth will continue until the whole layer is completed. Thus, the growth rate will be dependent on the step density.

In this case of a rough surface, the growth rate is proportional to the driving force (ΔT) near the kink sites and, since the kinks are everywhere, ΔT is practically the same all over the surface. Therefore, a linear relationship between the growth rate and the undercooling, approximately given by $v \approx K_T \Delta T$, is characteristic for atomically rough growth surfaces. Here, the kinetic coefficient K_T is a well defined quantity for rough surfaces. This relation is known as *continuous growth* which needs only a very small supercooling ΔT [83].

Two-Dimensional nucleation

Once the surface is atomically flat, without steps, the crystal growth process needs a two-dimensional (2D) nucleus or island monolayer of a certain diameter to initiate a next layer. The conditions to form a stable 2D nucleus at the top layer of the crystal can be treated in a way like 3D nucleation. After the formation of the nucleus of the new layer, it can be assumed that lateral growth of the new layer will immediately occur and soon be completed since the undercooling that was accumulated for nucleation is high enough

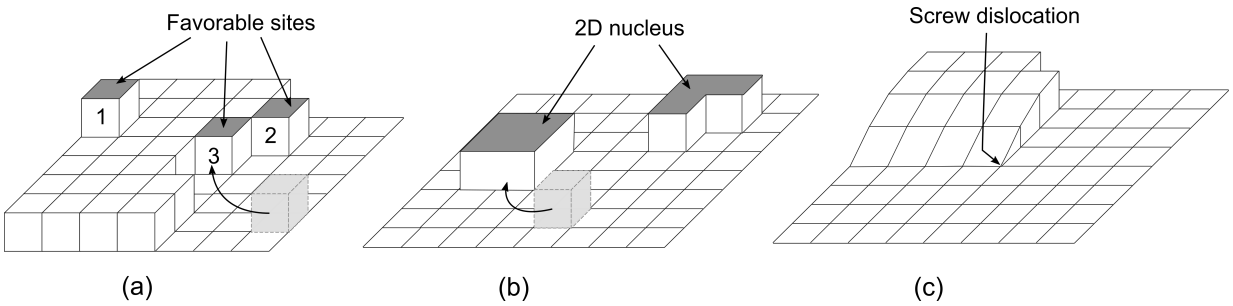

Figure 3.5: Crystal growth models in terms of attachment of the adsorbed atoms (grey cube) at the crystal surface: (a) KSV theory, favorable sites 1: terrace site, 2: step site, 3: kink site. (b) 2D nucleation, presence of small islands or holes may act as a 2D nucleus. (c) BCF theory, nucleation sites at the surface step produced by an emergent screw dislocation.

for step growth (see Figure 3.5(b)). Then, the rate of surface nucleation and, hence, of crystal growth, will depend on undercooling ΔT according to $v \propto \exp(-A/\Delta T)$, with A being a constant factor coming from the specific surface. 2D growth, therefore, has a high probability but only at high enough supersaturation values.

The Burton-Cabrera-Franck (BCF) theory

The KSV model assumes the pre-existence of steps on a crystal surface. Because of this, one of the major drawbacks of early nucleation theories was that, once the available step sites and kink sites available are consumed in the crystal, it could not longer provide favorable sites. In such situation, crystal growth will not take place unless new steps are created, e.g. by 2D nucleation. The Burton, Cabrera, and Franck [89] theory shows that screw dislocations can provide a continuous source of steps which can propagate across the surface of the crystal (see Figure 3.5(c)). Due to the end of the step is pinned at the dislocation, the shape of the step becomes spiral, and its shape is similar to an Archimedian spiral. Such growth caused by a screw dislocation is also called *spiral growth*.

The advantage of spiral growth is that the step does not disappear, leading to never ending steps. This fact overcame the problem of the 2D growth. Although the BCF theory assumed the existence of dislocations in the crystal in order to enhance the growth of a surface, the growth rate does not depend on the concentration of these dislocations. Burton, Cabrera, and Frank established a new relationship between growth rate and

supersaturation based on the spiral growth mechanism, resulting in $v \propto \Delta T^2$ for small undercooling. In general, high dislocation densities are very common defects of crystals in almost all solidification processes, and spiral growth is therefore very likely to occur at smooth interfaces.

In brief, with a parabolic or an exponential dependence which is the case of spiral growth or two-dimensional nucleation, respectively, the growth rate can never exceed that one of the continuous growth. Moreover, at a very high supercooling, the density of steps and kinks at a formerly smooth interface will become as high as in the case of an atomically rough one, and growth will proceed in a continuous way.

3.2.2 Mass and heat transport

As discussed in the previous section, the crystal growth is possible through the transport of atoms from the environment (liquid phase) by bulk and surface diffusion followed by incorporation of atoms at the step sites and, then, at the kink sites.

Assuming that the crystal grows in the z direction with constant velocity v, the temperature fields in the melt (L: liquid) and the crystal (S: solid) are governed by the equations

$$\nabla^2 T_L + \frac{v}{\kappa_L}\frac{\partial T_L}{\partial z} = \frac{1}{\kappa_L}\frac{\partial T_L}{\partial t}; \qquad \nabla^2 T_S + \frac{v}{\kappa_S}\frac{\partial T_S}{\partial z} = \frac{1}{\kappa_S}\frac{\partial T_S}{\partial t}, \tag{3.16}$$

where κ_L and κ_S are thermal diffusivities, considered to be constant and isotropic for cubic crystals. Thus, the mass concentration in the liquid and solid will follow the next expressions,

$$\nabla^2 C_L + \frac{v}{D_L}\frac{\partial C_L}{\partial z} = \frac{1}{D_L}\frac{\partial C_L}{\partial t}; \qquad \nabla^2 C_S + \frac{v}{D_S}\frac{\partial C_S}{\partial z} = \frac{1}{D_S}\frac{\partial C_S}{\partial t}, \tag{3.17}$$

where D_L and D_S are solute diffusivities, also considered to be constant and isotropic. Typically, $D_S \ll D_L$ thus the diffusion in the solid is ignored. D_L will be simply written as D from now on. Generally, heat transport works in parallel with the transport of matter, which usually is the rate-limiting process in solution growth. Mass transport is largely determined by the interactions of diffusion and convection near the liquid-crystal interface. At a growing crystal surface, the equilibrium partitioning of a solute between solid and fluid phases coupled with diffusion and convection results in segregation, i.e., the inhomogeneous distribution of a solute in a grown crystal.

3.2.3 Segregation

When growth proceeds from high temperature solutions, whose equilibrium segregation coefficient $k_0 = C_S/C_L$ is lower than unity, only part of the solute can be incorporated into the solid phase and the rest is continually being rejected into the melt at the liquid-crystal interface [90]. As a consequence, an enriched solute boundary layer of thickness δ is formed in front of the interface (see Figure 3.6) and δ can be used to quantify its thickness. The width of this boundary layer is determined by the growth rate v and by the diffusive and convective transport in the melt, which is very often difficult to predict. The diffusion boundary layer can be reduced if strong convection occurs, e.g. if forced convection is applied.

Neglecting convection in the liquid and other stirring mechanism in the vicinity of the interface other than diffusion, the concentration profile $C_L(z)$ in the melt adjacent to an interface moving with the rate v is given by,

$$C_L(z) = C_0 \left[1 + \frac{1-k_0}{k_0} \exp\left(-\frac{v}{D}z\right)\right]. \tag{3.18}$$

with C_0 being the melt composition in a given distance z to the interface (also denoted as C_L^{∞}); D the diffusion coefficient in the liquid; and k_0 the equilibrium segregation coefficient. From this, Burton *et al.* [90, 91] defined the effective segregation coefficient k_{eff} as,

$$k_{eff} = \frac{k_0}{1 + (1-k_0)\exp\left(-\frac{v\delta}{D}\right)} \tag{3.19}$$

According to this equation, k_{eff} will tend to k_0 at low values of v (and/or δ) and to unity at high values of growth rate (and/or δ). Thus, the segregation behavior during solidification at the liquid-solid interface is governed by a convective transport in the liquid phase as well as diffusive transport of the components. Consequently, the equilibrium segregation coefficient k_0 has to be replaced by an effective segregation coefficient, k_{eff}. Assuming a perfect mixing in the liquid phase to maintain a homogeneous melt, and not subsequent diffusion in the solid phase; both G. Gulliver [93] and E. Scheil [94] solved the mass conservation problem of interfacial segregation under local equilibrium. As a result, the Gulliver-Scheil segregation distribution for perfect mixing in the melt, as a function of the fraction of the molten charge solidified, is given by

$$C_S(z) = kC_0 \left(1 - \frac{z}{L}\right)^{k_0 - 1} \tag{3.20}$$

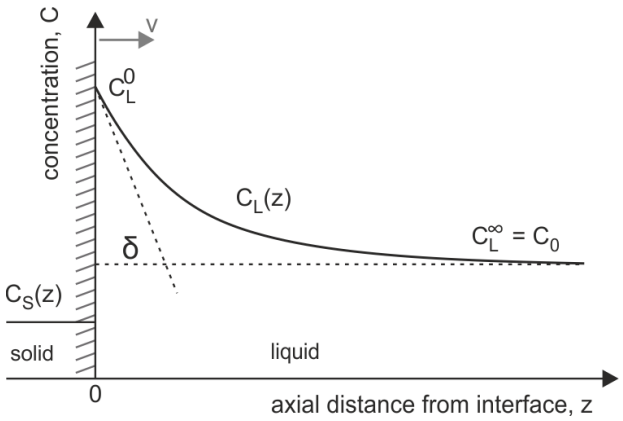

Figure 3.6: Solute concentration distribution near an advancing solid-liquid interface for $k_0 < 1$. δ follows the interpretation given by Wilson [92].

with z being the axial position and L the total length of the ingot.

3.2.4 Constitutional supercooling

One of the most critical and important transport-related phenomena that may affect the crystal quality is the constitutional supercooling appearing within the region of diffusion boundary layer. As the crystal grows, one of the compound component (in our case Sb) is rejected by the growing surface. Consequently, the gradient of concentration in the liquid $C_L(z)$ immediately ahead of the interface becomes appreciably higher than the one of the melt in some distance to the growing crystal (see Figure 3.7(a)). This accumulation of the impurities results in a depression of the liquidus temperature $T_L(z)$ as illustrated in Figure 3.7(b) [84]. Here, according to the liquidus curve of the phase diagram and assuming a linear slope, $m = -dT_L/dC_L$, the position-dependent liquidus temperature of the melt can be calculated. Since the highest gradient of the liquidus temperature occurs at the phase boundary ($z = 0$), the stability criterion may be expressed as:

$$\mathrm{grad}T_{exp} \geq \frac{dT_L}{dz} \,, \tag{3.21}$$

where T_{exp} is the position-dependent experimental temperature in front of the growth interface. With Equation (3.18) and the slope of the liquidus curve, Equation (3.21) turns to:

$$\frac{\mathrm{grad}T_{exp}}{v} \geq \frac{mC_0(1-k_0)}{Dk_0} \,. \tag{3.22}$$

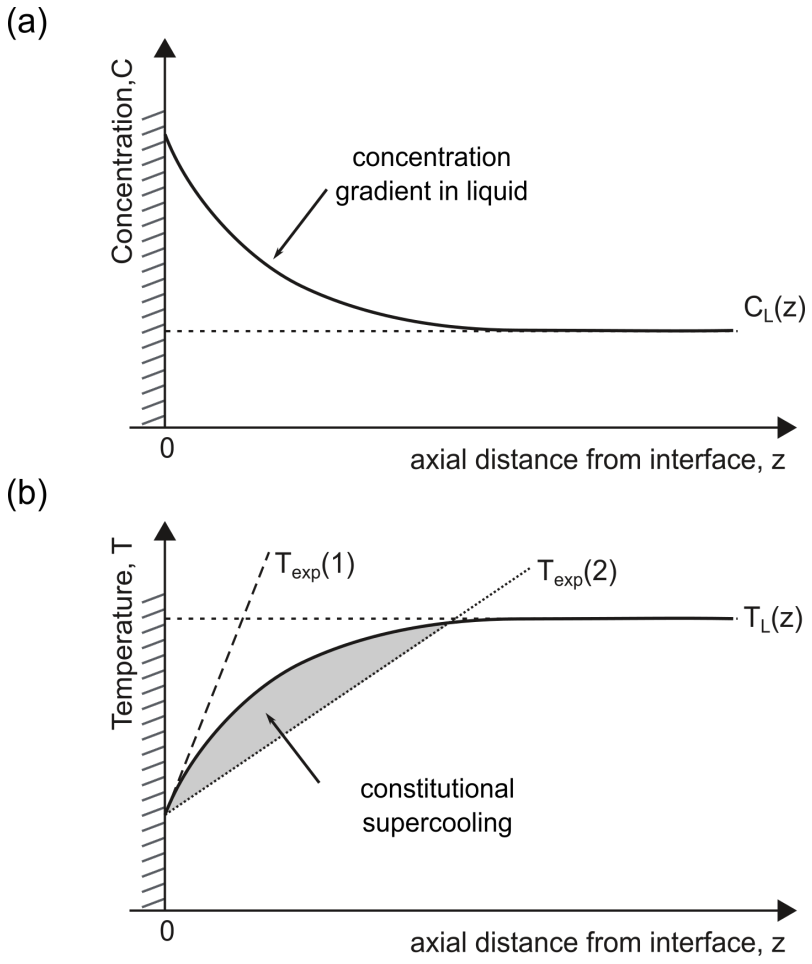

Figure 3.7: Graphs of (a) concentration distribution $C_L(z)$ and (b) liquidus temperature $T_L(z)$ to illustrate constitutional supercooling. $T_{exp}(1)$ and $T_{exp}(2)$ represent different experimental temperature gradients that obey or violate the constitutional supercooling criterion.

This expression, which is the condition to avoid constitutional supercooling and derived theoretically by W.A. Tiller *et al.* [95], is known as constitutional supercooling criterion. It serves as a rough limit for the highest possible growth rate of a crystal to be solidified from a multi-component melt composition C_0. In Figure 3.7(b), $T_{exp}(1)$ indicates the minimum desired temperature gradient to avoid constitutional supercooling leading to a stable growth. But, if the actual temperature in the melt is $T_{exp}(2)$ an unstable growth is predicted to occur because the melt just ahead of the interface remains below its equilibrium liquidus, $T_L(z)$, and, therefore, is slightly supercooled.

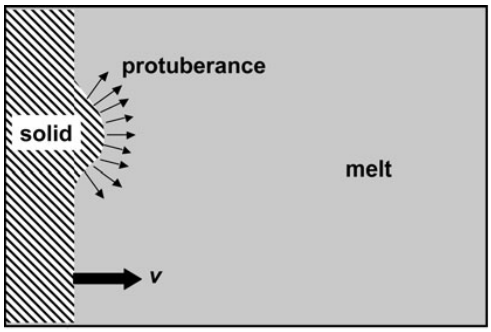

Figure 3.8: A disturbance on an unstable solid-liquid interface projects a small distance into supercooled melt. The metastable liquid is supersaturated relative to the solid, so the protuberance can grow farther, releasing latent heat and rejecting solute (small arrows) into the surrounding melt. Image taken from [96].

These perturbations of the interface, perhaps due to any variety of fluctuations occurring in the temperature, composition, or pressure, can cause the formation of a small forward-pointing projection of solid as is illustrated in Figure 3.8. If a projection caused by an instability of the growing interface crystallizes faster than the rest of the interface, a part of the melt may form a liquid solution drop (inclusion) captured by the matrix that has already been crystallized [96].

Chapter 4

Experimental

In this chapter, the solidification strategy to get large single crystals is discussed together with the different crystal growth methods used in the present work. The characterization methods are also presented. The majority of the text contained in this chapter was previously published in our paper [97].

4.1 Growth strategy

As it was discussed in the Chapter 2, the binary phase diagrams Fe-Sb (Figure 2.1) and Co-Sb (Figure 2.5) display some similar properties, e.g. both phases of interest are peritectically melting, $CoSb_3$ at 874 °C and $FeSb_2$ at 750 °C, respectively. In fact, $FeSb_2$ and $CoSb_3$ can not be crystallized from congruent melts. Instead, in both cases there is a branch of the appropriate liquidus curve starting at the individual peritectic temperature and ending in the eutectic point next to pure Sb that describes the binary equilibria with $FeSb_2$ or $CoSb_3$. This is the main reason why high-temperature solution growth from a Sb-rich solution is the only mechanism to crystallize these two compounds from a liquid phase. Moreover, because of the relatively high Sb vapor pressure, crystal growth in closed ampoules seems to be the best synthesis method in comparison with more powerful techniques such as Czochralski growth [60] that can only be used if additional modifications of the growth process like in the liquid-encapsulated technique are applied.

In crystal growth from high-temperature solutions, slow cooling is the usual mechanism to get a supersaturated solution and, then, to initiate crystallization. As a consequence of the incongruent solidification, during crystal growth the solution becomes permanently

enriched in the solvent and, hence, the growth temperature has to be lowered according to the decreasing liquidus temperature. In other words, materials transport, which is anyway the limiting process in high temperature solution growth, becomes even worse with respect to two parameters:

- The concentration difference at the growing interface (C_L - C_S), that describes the amount of material offered in the liquid (C_L) but not incorporated into the crystal (C_S being the composition in the crystal) is rejected at the interface and increases during the growth process.
- With increasing Sb concentration of the liquid C_L, the equilibrium temperature gets lower making materials transport even slower, e.g., due to the exponentially decreasing diffusion coefficient.

Hence, prior to the first crystal growth experiments, it was clear that materials transport will be the decisive factor of the growth experiments. Liquid inclusion formation will probably be the most difficult problem to solve. However, these effects were not mentioned in the work on vertical Bridgman growth of $FeSb_2$ published by Y. Cao *et al.* [53]. In vertical ampoules with temperature gradients antiparallel to the vector of gravity, buoyancy-driven convection is extremely slow and various mechanisms of forced convection have been suggested to assist materials transport. Among them, accelerated crucible rotation technique (ACRT) [84] is considered one of the most powerful tools, but it always introduces some periodicity into the solidification process that might be detrimental. Notice that a horizontal arrangement of the Bridgman growth ampoule, that would remarkably increase buoyancy-driven convection, cannot be applied in the Sb-containing systems because Sb condensation at the cold end of the ampoule would dissolve the already crystallized $FeSb_2$ or $CoSb_3$.

Therefore, in this thesis, we have chosen an inclined arrangement of the Bridgman method with a tilting angle that ensures to have always the crystal being embedded in the liquid (see Figure 4.1). Here, in order to further increase convective motion, the whole ampoule is rotated along its axis. During this process, the already grown crystal rotates together with the ampoule, while the liquid solution filling only a part of the empty space in the ampoule tries to maintain its horizontal surface level due to gravity forces. Consequently, a very effective relative motion can be expected between the

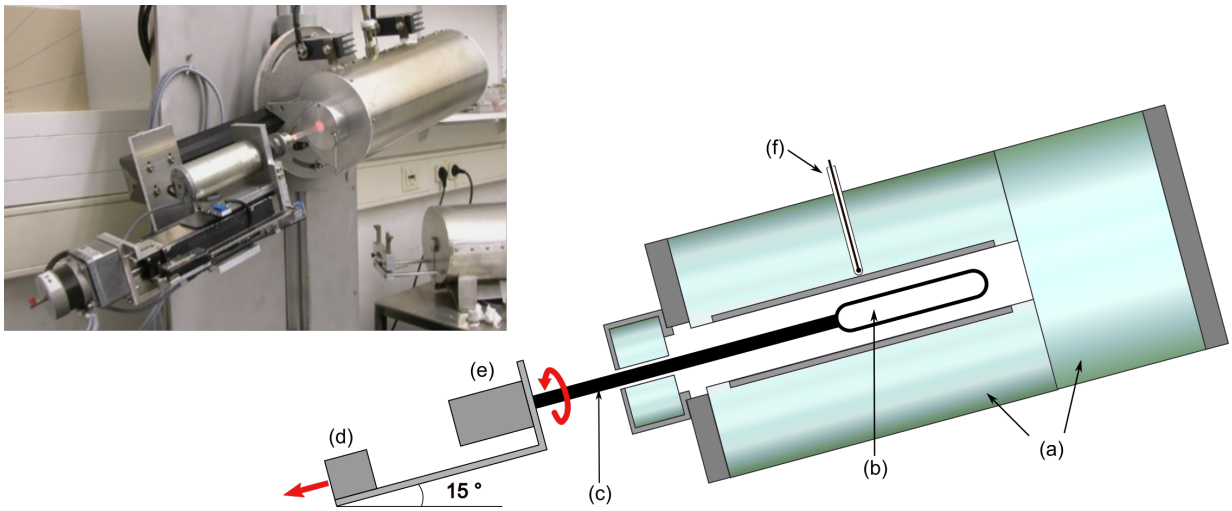

Figure 4.1: Photograph and schematic sketch of the used apparatus in the inclined Bridgman arrangement: (a) Fiber insulation (Fibrothal tube element RAC 40/200, Kanthal Hallstahammar, Sweden), (b) fused silica ampoule, (c) silica rod, (d) translational motor, (e) rotational motor, (f) thermocouple.

rotating solids (ampoule with growing crystal) and the solution. This is very relevant at the crystal/solution interface where permanent release of the liquid excess component Sb occurs. This approach to forced convection is similar to mixing techniques that have been suggested in crystal growth literature for several purposes in a closed container [98–101].

4.2 Growth conditions

4.2.1 Synthesis

Preparation of ampoules

The fused silica ampoules tubes for the growth anpoules were bought from Qsil GmbH company (Germany). Their thermal expansion coefficient is 5.5×10^{-7} K^{-1} (between 20-300 °C) [102]. Specific ampoules for the various types of the growth experiments were prepared by Gaβner Glastechnik Company (Munich) according to the authors design drawings. Here, five types of silica fused ampoules with different dimensions and shaped tips were used, see Figure 4.2. Before starting each experiment, the ampoules were washed with water, etched with a mixture of hydrogene fluoride and nitric acid , and rinsed with distilled

water several times to remove any possible contamination. Then, they were dried and baked in vacuum at 1050 °C for 12 h. Additionally, to prevent the sticking of the Fe-Sb melt on the ampoule wall, a graphitization was carried out in ampoules 3-5 using pyrolysis of ethanol-saturated nitrogen at approx. 1000 °C.

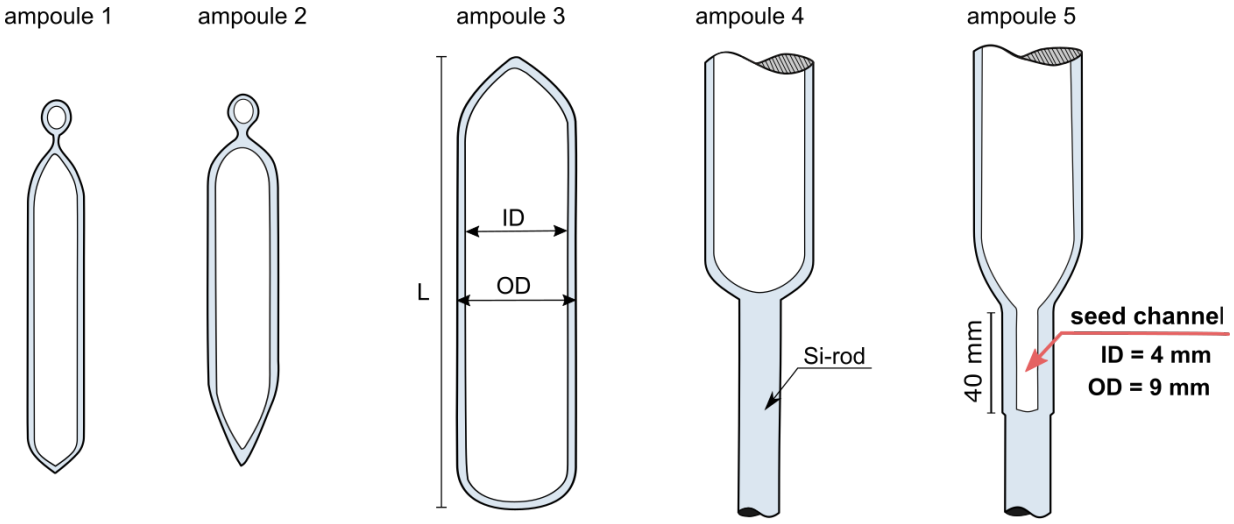

Ampoule	ID (mm)	OD (mm)	L (mm)
1	8	11	80
2	12	15	80
3	20	23	100
4	15	18	100
5	16	19	100

ID : Inner diameter
OD: Outter diameter
L : Length

Figure 4.2: Types of ampoules used in the synthesis and crystal growth of the Sb-based compounds.

Raw materials and etching process

The high-purity raw materials used in the experiments were: Iron (Fe) and Cobalt (Co) rods of 5 mm diameter (4N-grade and 3N-grade, respectively) and 5N-grade Antimony (Sb) granules within 1-1.5 mm diameter. Fe and Co rods help avoiding too high specific surfaces of powders. All materials were bought from CrysTech Berlin, Germany. To remove any possible contaminants (e.g., oxide layers and organic impurities) the Fe and Co pieces were cleaned using the etching process based on recipes suggested by P. Dreier [103]. The chemicals used to carry out this process are nitric acid HNO_3, hydrochloric acid HCl,

acetone and distilled water H_2O. The mixing ratio of the acids is different for each metal.

Fe pieces were etched in three different acid solutions: first in 1:1 HNO_3 (the mass is here reduced); then in 1:1 HCl (that reduces oxides and to some extent the mass) and, finally, in 1:3 HCl (removes residual oxides and produces a shiny surface). After each step the Fe pieces were rinsed with H_2O; only in the last step they were rinsed three times in H_2O, twice in acetone and once in acetone p.a.. The etching time in each step varied within 30 - 60 s. Similarly, this process was done for Co pieces: conc. HNO_3, 1:1 HNO_3 and aqua-regia were used as etching solutions with destilled H_2O in between. Sb granules were used without further treatment. Moreover, InSb single crystals obtained in previous work were used as source on Indium doping in the $CoSb_3$ compounds.

Starting melt composition

The ampoule was filled with a total charge of mass around 5 - 6 g or 50 - 80 g according to the growth technique used for the solidification process. The starting melt compositions to grow $FeSb_2$, $Fe_{1-x}Co_xSb_2$, $CoSb_3$, and $In_xCo_4Sb_{12}$ are listed in the Tables 4.1, 4.2, 4.3, and 4.4, respectively. Masses of each raw material and total charge are also shown. x and x_0 refer to the mole fraction of each component in the solid-phase (crystal) and the starting compositions.

Table 4.1: Starting compositions and masses to grow $FeSb_2$ from a liquid solution $Fe_{1-x_0}Sb_{x_0}$ with $x_0 = 0.905$ or 0.91.

Sample code	Starting solution	Sb (g)	Fe (g)	Total mass (g)
QX566	$Fe_{0.095}Sb_{0.905}$	38.35542	1.84670	40.20212
QX580	$Fe_{0.095}Sb_{0.905}$	59.60321	2.87002	62.47323
QX595	$Fe_{0.095}Sb_{0.905}$	57.32576	2.76003	60.08579
QX601	$Fe_{0.09}Sb_{0.91}$	60.34030	2.73756	63.07786
QX605	$Fe_{0.09}Sb_{0.91}$	50.79496	2.30425	53.09921
QX609	$Fe_{0.09}Sb_{0.91}$	55.01831	2.49569	57.51400

Table 4.2: Starting compositions and masses to grow $Fe_{1-x}Co_xSb_2$ from a liquid solution $(Fe_{1-x_0}Co_{x_0})_{0.10}Sb_{0.90}$ with $0.1 \leq x_0 \leq 0.5$.

Sample code	Starting solution	Sb (g)	Fe (g)	Co (g)	Total mass (g)
QX539-A	$(Fe_{0.9}Co_{0.1})_{0.10}Sb_{0.90}$	4.58531	0.21259	0.02215	4.82005
QX546-A	$(Fe_{0.8}Co_{0.2})_{0.10}Sb_{0.90}$	6.11834	0.24908	0.06619	6.43361
QX546-B	$(Fe_{0.7}Co_{0.3})_{0.10}Sb_{0.90}$	5.59273	0.20018	0.08954	5.88245
QX546-C	$(Fe_{0.5}Co_{0.5})_{0.10}Sb_{0.90}$	5.48554	0.13992	0.14739	5.77285
QX545	$(Fe_{0.9}Co_{0.1})_{0.10}Sb_{0.90}$	47.39501	2.17770	0.25103	49.82374

Table 4.3: Starting compositions and masses to grow $CoSb_3$ from a liquid solution $Co_{1-x_0}Sb_{x_0}$ with $0.915 \leq x_0 \leq 0.950$.

Sample code	Starting solution	Sb (g)	Co (g)	Total mass (g)
QX590-A	$Co_{0.085}Sb_{0.915}$	5.14991	0.23154	5.38145
QX590-B	$Co_{0.08}Sb_{0.92}$	5.10602	0.21465	5.32067
QX590-C	$Co_{0.075}Sb_{0.925}$	4.82020	0.18917	5.00937
QX593-B	$Co_{0.073}Sb_{0.927}$	7.77962	0.29661	8.07623
QX593-C	$Co_{0.071}Sb_{0.929}$	7.95412	0.29424	7.95412
QX586-A	$Co_{0.07}Sb_{0.93}$	5.65000	0.20586	5.85586
QX586-B	$Co_{0.06}Sb_{0.94}$	5.55000	0.17146	5.72146
QX586-C	$Co_{0.05}Sb_{0.95}$	6.62000	0.16876	6.78876
QX591	$Co_{0.07}Sb_{0.93}$	68.80259	2.50682	71.30941
QX620	$Co_{0.07}Sb_{0.93}$	67.9884	2.47681	70.46525
QX625	$Co_{0.07}Sb_{0.93}$	73.31154	2.67091	75.98245

Table 4.4: Starting compositions and masses to grow $In_xCo_4Sb_{12}$ from a liquid solution $(In_{x_0}Co_{1-x_0})_{0.06}Sb_{0.94}$ with $0.05 \leq x_0 \leq 0.2$.

Sample code	Starting solution	Sb (g)	InSb (g)	Co (g)	Total mass (g)
QX534-A	$(In_{0.0741}Co_{0.9259})_{0.06}Sb_{0.94}$	6.37287	0.00979	0.19459	6.57725
QX534-B	$(In_{0.2169}Co_{0.7831})_{0.06}Sb_{0.94}$	9.23706	0.04158	0.27570	9.55434
QX534-C	$(In_{0.2857}Co_{0.7143})_{0.06}Sb_{0.94}$	6.44744	0.03821	0.19029	6.67594
QX531	$(In_{0.1463}Co_{0.8537})_{0.06}Sb_{0.94}$	73.90060	0.22389	2.23096	76.35545
QX537	$(In_{0.0741}Co_{0.9259})_{0.06}Sb_{0.94}$	71.07376	0.10907	2.17031	73.35314

Synthesis

The appropriate compositions of raw materials were filled in cleaned silica ampoules. The ampoules were then sealed under a vacuum of approx. 10^{-6} mbar (in order to prevent oxidation of material). Syntheses were done by heating the ampoules in a horizontal tubular furnace to a maximum temperature of 800 °C for $Fe_{1-x_0}Sb_{x_0}$ and $(Fe_{1-x_0}Co_{x_0})_{0.10}Sb_{0.90}$ or 930 °C for $Co_{1-x_0}Sb_{x_0}$ and $(In_{x_0}Co_{1-x_0})_{0.06}Sb_{0.94}$; with a heating rate of 2 K/min. After 12 h at maximum temperature, cooling to room temperature was done at a rate of 10 K/min. Temperatures slightly above the liquidus temperature were used in order to ensure the homogenization of the charge. Finally, depending on which growth method was chosen, the ingots were transferred within the ampoule to the growth apparatus or were crushed before completely filling the material into the special growth ampoules.

4.2.2 Vertical Bridgman method

In this thesis, the vertical growth experiments were only performed to complete the following tasks:

- Small amount of different starting compositions $Co_{1-x_0}Sb_{x_0}$ with $0.915 \leq x_0 \leq 0.950$ compositions were crystallized in low-diameter fused silica ampoules (ampoule 1 in Figure 4.2) to determine the first-to-freeze (FTT) phase and, thus, to check the peritectic melt composition in the published Co-Sb phase diagram.
- A tapered silica ampoule (see ampoule 2 in Figure 4.2) was used to grow $FeSb_2$ from a $Fe_{0.095}Sb_{0.905}$ liquid for comparison with the inclined geometries.

- Preliminary tests with small amounts of $(In_{x_0}Co_{1-x_0})_{0.06}Sb_{0.94}$ $(0.05 \leq x_0 \leq 0.2)$ and $(Fe_{1-x_0}Co_{x_0})_{0.10}Sb_{0.90}$ $(0.1 \leq x_0 \leq 0.5)$ compositions were prepared to find an appropriate amount of In and Co doping in these ternary systems.

The sketch of the vertical Bridgman furnace is shown in Figure 4.3(a). This home-made 80 cm long furnace is based on Kanthal A1 resistance wire (Kanthal Hallstahammar, Sweden) wound on an alumina tube. It has an approximately parabolic temperature profile with axial temperature gradients increasing from 10 K/cm to 15 K/cm within the operation distance of approx. 200 mm. The temperature profile of the used furnace is shown in Figure 4.3(b) for a set-point (SP) temperature of 800 °C and 900 °C together with the starting position of the ampoule.

Since in these experiments no seed crystal was used, the above described synthesis was done in the growth ampoules (ampoule 1 in Figure 4.2) but in a horizontal furnace in

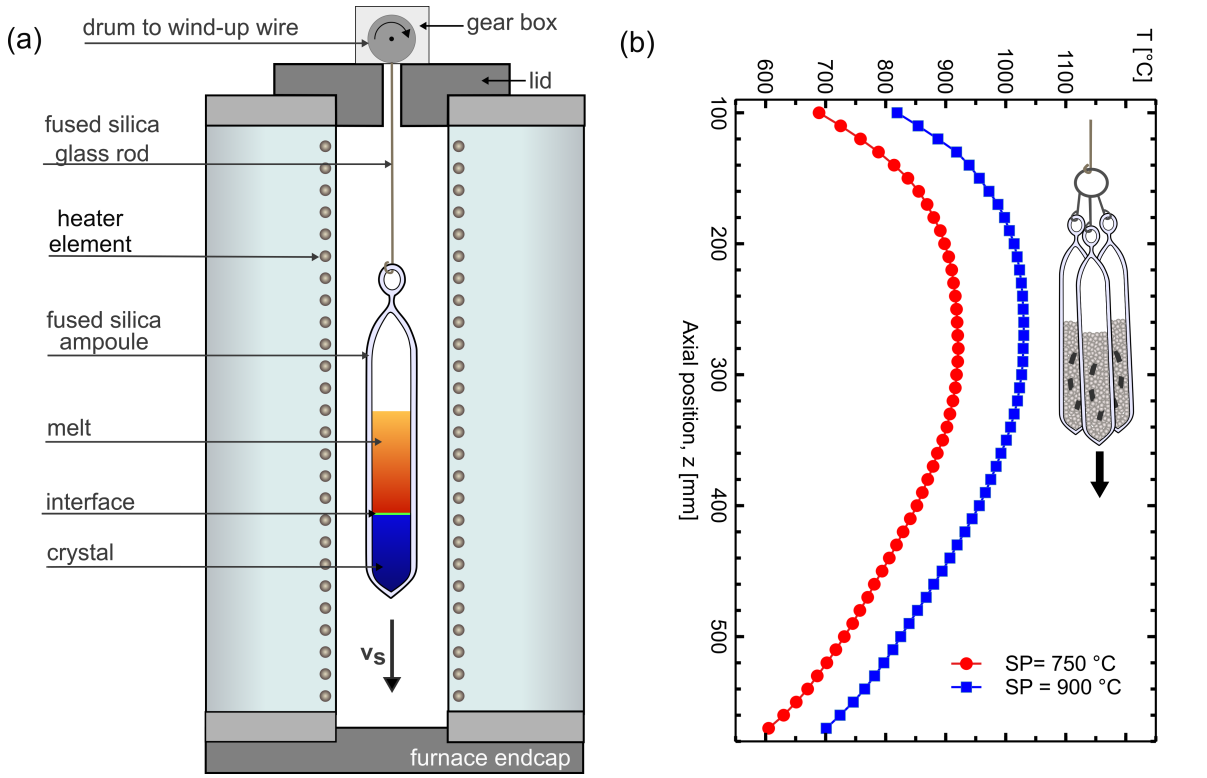

Figure 4.3: (a) Schematic sketch of the apparatus used for the Vertical Bridgman experiments. (b) Temperature profile in the vertical Bridgman furnace for different set points (SP) of temperature, where three small ampoules are used simultaneously in each experiment.

order to achieve perfect mixing during the synthesis. After cooling down, the ampoules were transferred to the vertical Bridgman furnace without opening them in between. For convenience, in the latter experiments three ampoules with different starting composition were introduced in the vertical furnace at the same time, as it can be seen in Figure 4.3(b), ensuring that the tip of each ampoule is at the same height. Each ampoule of the same run was labeled as A, B or C (see Tables above). For the crystal growth the following procedure was carried out: (i) The ampoule was heated up to a set point (SP) of 900 °C or 800 °C according to the corresponding liquidus temperatures of the specific starting charge and kept for 24 hours in the upper hot zone of the furnace; (ii) crystallization was initiated by lowering the ampoule using a constant translation rate of 2 mm/d; (iii) after an overall translation of 45 days that corresponds to 90 mm of displacement the furnace was cooled down to room temperature at a rate of approx. 100 K/h. The necessary travel distance was calculated in order to allow complete crystallization of the eutectic rest that is close to pure Sb.

4.2.3 Inclined Bridgman method

The ampoule for inclined Bridgman growth experiments for the growth of $FeSb_2$ was prepared in the same way as the vertical ones with an inner diameter of 15 mm and a total length growth chamber of 100 mm (ampoule 4 in Figure 4.2). Native seeding was not tried in this series of experiments. Synthesis with similar parameters as described above was done in the inclined Bridgman growth facility with the oven in horizontal position. After 12 h of homogenizing the melt, the whole arrangement of ampoule and furnace was tilted by 15° with respect to the horizontal, the set point temperature was decreased by 50 K to 750 °C and the translation of the ampoule was started without cooling the ampoule in between. An ampoule translation rate 2.4 mm/d was chosen. After an overall translation period of approx. 35 days that corresponds to 80 mm of displacement, the furnace was cooled down using a rate of 15 K/h. In this experiment the ampoule was kept without rotation in order to compare the final product with the results obtained by the other growth methods. For this purpose, only the crystal QX601 with starting composition $Fe_{0.09}Sb_{0.91}$ (see Table 4.1) was prepared with this method.

4.2.4 Inclined Rotary Bridgman (IRB) method

Inclined Rotary Bridgman experiments were always done with a 15° inclination of the ampoule and the furnace with respect to the horizontal. Also, the rotation rate was kept constant at 100 rpm. The sketch of the equipment is shown in Figure 4.4. When doing the experiments without external seeding, the procedure was the same like described in Section 4.2.3 but, in this case, translation and rotation were started at the same time after synthesizing the material.

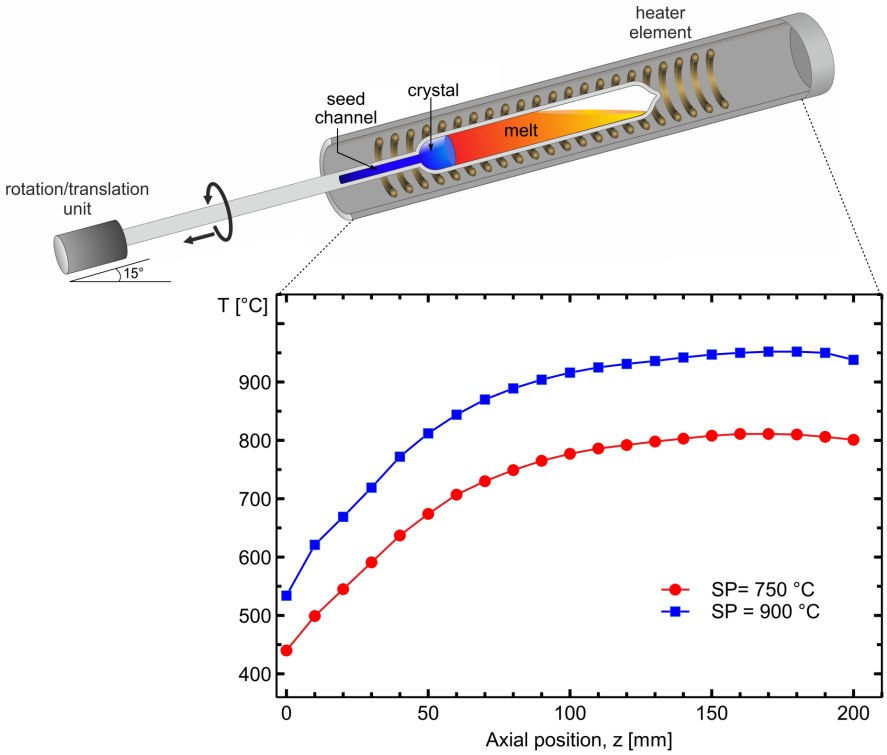

Figure 4.4: Schematic sketch of the growth ampoule (with seed channel) and apparatus used for the Inclined Rotary Bridgman experiments showing the temperature profile over the length of the IRB furnace with different set points (SP) of temperature.

In the final series of Inclined Rotary Bridgman (IRB) experiments the ampoule 5 was used (see Figure 4.2). Here, native seeds (4 mm diameter × 15 mm) or fine-grained stoichiometric $FeSb_2$ or $CoSb_3$ powders (approx. 2.5 g) obtained from former experiments were introduced into the seed channel. In these cases, the syntheses could not be combined with the growth experiment but was done in separate ampoules like described in Section

4.2.1. The crashed material was filled into the growth ampoule, sealed at approx. 10^{-6} mbar and heated up to the starting temperature. Rotation of the ampoule was only started after homogenizing again the synthesized material for several hours. During the whole crystal growth process, rotation as well as translation rates were kept constant at rates of 100 rpm and 0.1 mm/h (2.4 mm/d), respectively. Rotation was stopped before cooling down the material to room temperature. Cooling was done with a rate of 100 K/h.

4.3 Cutting and surface preparation

The crystals were cut using the wire saw WS 22 (KD UNIPRESS) with a 50 μm tungsten wire and a slurry of 800 mesh boron carbide powder in glycerol. For optical micrographs and EPMA measurements the surface first was prepared by lapping followed by polishing. The lapping process was made over a boron silicate glass disk using Al_2O_3 powder of 3 - 6 μm grain size, which was previously diluted with a bit of distilled water to form a paste. For the polishing, an diamond paste of decreasing grain sizes of 3, 1 and 0.25 μm was used, obtaining completely smooth, scratch-free, and shining surfaces.

4.4 Characterization methods

4.4.1 X-ray powder diffraction (XRD)

This technique was mainly used to investigate the lattice parameters of the grown crystals. X-ray powder diffraction measurements were performed in two configurations: the Bragg-Brentano geometry and the Debye-Scherrer geometry. The equipment used in Bragg-Brentano geometry is a GE XRD3003TT diffractometer with a Cu-$K_{\alpha 1}$ radiation (λ = 1.5406 Å) at 40 kV and 40 mA. The data was collected in the 2θ range of 10° - 120° with a step size of 0.013° and a exposure time/step of 150 s, using a divergence slit of 1 mm and a threshold of 7.5 keV. The threshold was set, as Fe fluoresces by Cu-$K_{\alpha 1}$ radiation and, hence, background and peak height will be affected. The sample was spread as evenly flat as possible with ethanol on a zero-background quartz sample holder and then dried. During the measurement, it rotated with 1 Hz.

In the case of Debye-Scherrer geometry, a STOE diffractometer equipped with a Ge(111) monochromator to produce Mo-$K_{\alpha 1}$ radiation (λ = 0.7093 Å) at 50 kV and 30 mA was

used. Here, the powders were contained in glass capillaries of 0.5 mm inner diameter kept in rotation for better statistic. Data was collected in the 2θ range of 5° - 60° with a step size of 0.1° and an exposure time/step of 10 s. All the measurements were performed with an internal standard NIST Si640c to accurately determine the lattice parameters at room temperature by Rietveld refinement using the program package FULLPROF [104].

4.4.2 Laue X-ray diffraction

Laue X-ray diffraction in the backscattering mode was used for two purposes: (i) to check if the grown crystals are single crystals or contain sub-grains; and (ii) for orienting the single crystals prior to cutting them in certain crystallographic directions, e.g., for seed crystal preparation or further physical property measurements. The crystals are placed in a polychromatic X-ray beam at a fixed distance (approx. 50 mm) to a photographic plate detecting backscattered reflections of the sample. Thus, imaging and re-orienting procedures are repeated until the desired crystal orientation is obtained in the pattern. The measurement was done operating the generator at 45 kV and 33 mA with a exposure of 15 min for each image.

4.4.3 Measurement of experimental density

The experimental density of the grown crystal was determined using the buoyancy method. This method is based on the Archimedes principle, where a mass body apparently loses just as much in weight as it displaces in amount of liquid. The unknown density of a sample is determined over at least 10 measurement cycles, which consist of three individual measurements. The experimental setup of the three individual measurements is shown in Figure 4.5.

The density of the buoyant fluid (ρ_L) is calculated using the equation:

$$\rho_L = (\rho_x - \rho_0)\frac{m_2 - m_3}{m_1} + \rho_0 \ , \tag{4.1}$$

where $\rho_0 \approx 0.001109$ g/cm^3 is the air density[1], m_{1-3} are the masses according the description in Figure 4.5, ρ_x is the density of the sample (or standard). Rewriting Equation

[1] Ambient pressure and temperature are included in δ_0.

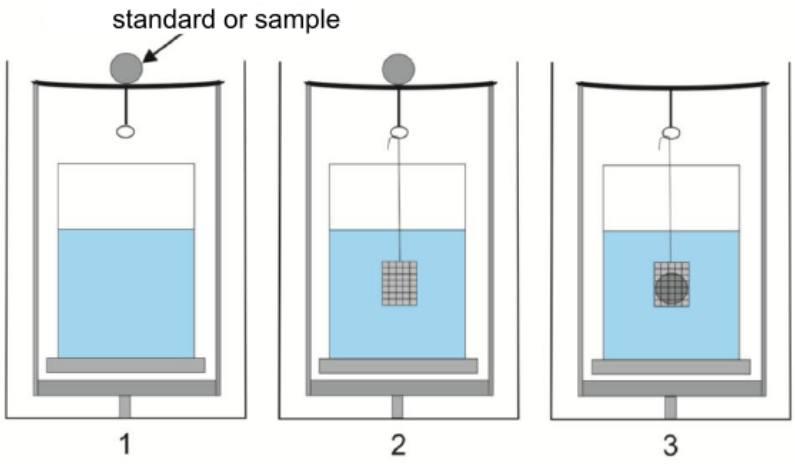

Figure 4.5: Sketch of the individual measuring processes of a precision density measurement: (1) weighing standard/sample, (2) weighing standard/sample including empty wire cage, (3) weighing the sample placed in the wire cage.

4.1, the experimental density of the sample (or standard) can be determined by:

$$\rho_x = (\rho_L - \rho_0)\frac{m_1}{m_2 - m_3} + \rho_0 \ . \tag{4.2}$$

The experimental results are then compared with the theoretical density ρ_{calc} which is defined as follows:

$$\rho_{calc} = \frac{Z \cdot M}{V \cdot N_A} \ , \tag{4.3}$$

with Z as the atomic number and M as the molar mass of the formula units per elementary cell. V is the volume of the unit cell of a phase which can be determined from the X-ray analysis and N_A is the Avogadro constant ($6.022137\times\ 10^{23}$ mol^{-1}).

4.4.4 Electron probe micro analysis (EPMA)

Chemical compositions of the crystals were determined by electron probe micro analysis (EPMA) using a Cameca SX100 equipped with a LaB_6 cathode. Here, to assure electrical contact between crystal and sample holder, conductive silver lacquer was used. The crystals were measured with a voltage of 15 keV and a beam current of 40 nA. Calibration was done using standards of elemental pure Co and Fe, and binary InSb (50 at.% In, 50% at.% In) for Sb and In.

Chapter 5

Growth of $FeSb_2$ and $Fe_{1-x}Co_xSb_2$ crystals

In this chapter, the efficiency of the Inclined Rotary Bridgman (IRB) method to obtain large single crystals of $FeSb_2$ and $(Fe, Co)Sb_2$ is proved and discussed. Prior to this, we will use the vertical Bridgman method and the inclined Bridgman method (without ampoule rotation) to grow $FeSb_2$ in order to compare the results with the IRB method.

5.1 $FeSb_2$

5.1.1 Vertical Bridgman experiment

The $FeSb_2$ ingot (crystal QX566) prepared by the vertical Bridgman method using a starting composition $Fe_{0.095}Sb_{0.905}$ is shown in Figure 5.1(a). From its outer appearance the interface between the two phases can be seen, with $FeSb_2$ being the lower and Sb-rich eutectic fabric which is practically pure Sb. The first part of the $FeSb_2$ ingot was longitudinally cut as is shown in Figure 5.1(b). Here we found a high number of large inclusions (bright grey parts) whose amount increases in the growth direction. The inclusions consist of a large amount of pure Sb and a very small fraction of $FeSb_2$ as can be seen at higher magnification in Figure 5.1(c), which is expected from the binary phase diagram (see Figure 2.1). In general, these Sb-rich inclusions can be explained by the incongruent crystallization conditions with a large excess of Sb in the liquid phase that is rejected at the interface during crystallization of $FeSb_2$.

In addition, small cracks were observed near to the Sb-inclusions. The formation of cracks in $FeSb_2$ may be related to the excess of thermomechanical stress due to different reasons: (i) the different thermal expansion coefficients between the orthorhombic $FeSb_2$ ($\alpha_a = 4.2 \times 10^{-6}$ K^{-1}, $\alpha_b = 13.0 \times 10^{-6}$ K^{-1} and $\alpha_c = 34.0 \times 10^{-6}$ K^{-1}) [105] and the hexagonal Sb-inclusions ($\alpha_a = 8.4 \times 10^{-6}$ K^{-1} and $\alpha_c = 16.2 \times 10^{-6}$ K^{-1}) [106]. The mismatch between the linear expansion coefficients of the two phases can exert additional force in the lattice which may cause cracks during the cooling processes. (ii) The different orientation of individual $FeSb_2$ grains with the anisotropy of thermal expansion.

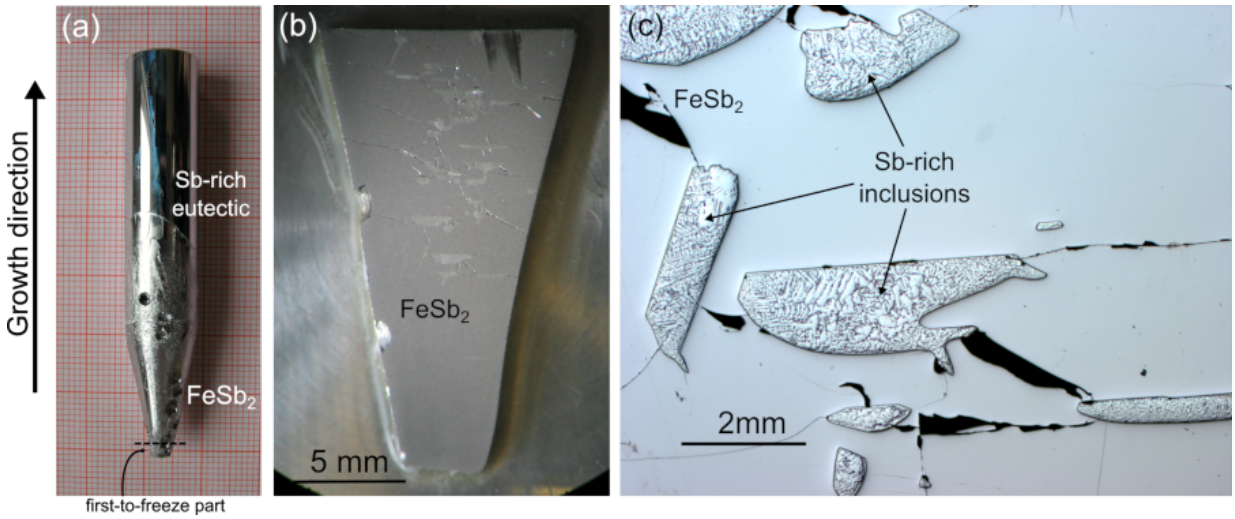

Figure 5.1: (a) Ingot of $FeSb_2$ obtained by the vertical Bridgman method from a starting composition $Fe_{0.095}Sb_{0.905}$ (crystal QX566). (b) Photograph of the longitudinal section of QX566 corresponding to $FeSb_2$ phase. Bright grey parts are crystallized Sb-liquid inclusions. (c) Magnification under incident light microscopy showing large Sb-inclusions and cracks.

5.1.2 Inclined Bridgman experiment

The $FeSb_2$ ingot (crystal QX601) obtained by the inclined Bridgman method, i.e. *without rotation of the ampoule* and grown from a starting composition $Fe_{0.09}Sb_{0.91}$ is shown in Figure 5.2(a). One can clearly see the interface between the $FeSb_2$ and Sb-rich eutectic phases, where the former has a mirror-like surface. Only approx. 22% of the total volume of the ingot consists of $FeSb_2$ crystal. A longitudinal cut of the first part of the $FeSb_2$ ingot

is shown in Figure 5.2(b). Large and numerous cracks that seem to originate from the edge of the crystal were observed in the polished surface of $FeSb_2$. At higher magnification, much smaller and fewer Sb-inclusions (20 - 45 μm) have been found compared to those observed in crystals grown by using the vertical Bridgman technique (see Figure 5.2(c)). This result shows that the increase of the buoyancy-driven convection produced by the inclination of the furnace decreases the Sb-inclusion formation considerably.

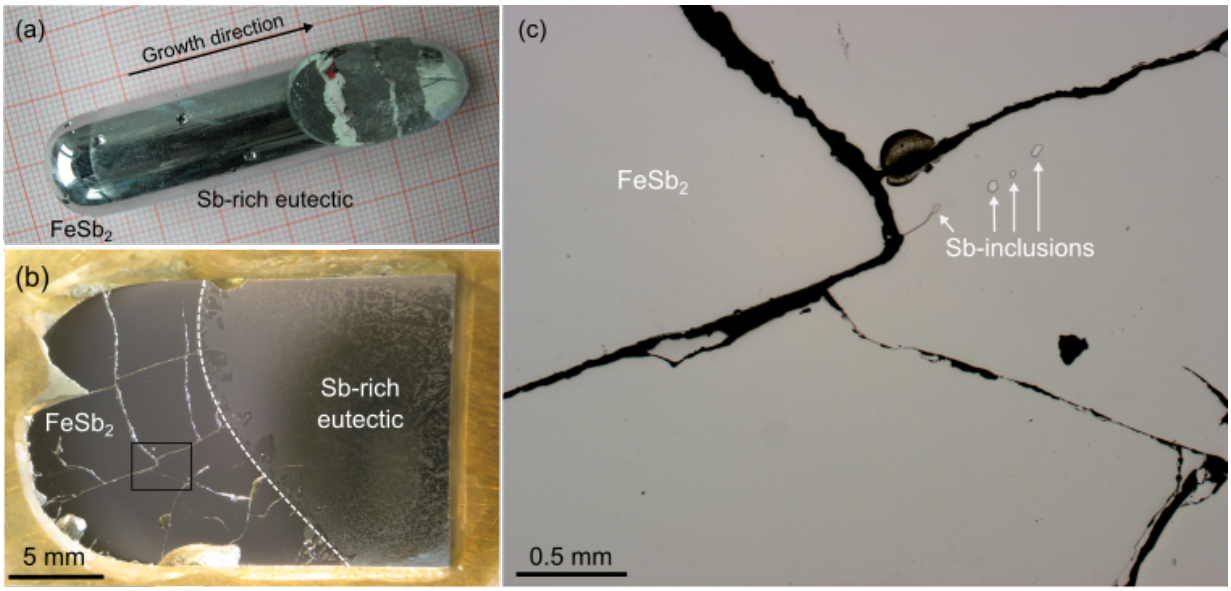

Figure 5.2: (a) Ingot of $FeSb_2$ (crystal QX601) obtained by Inclined Bridgman method from a starting composition $Fe_{0.09}Sb_{0.91}$. (b) Photograph of the longitudinal section of the first part of QX601. White dashed line marks the interface between the $FeSb_2$ and Sb-rich eutectic phases. (c) Magnification under incident light microscopy shows small Sb-inclusions indicated by arrows. Large cracks can be also observed.

5.1.3 Inclined Rotary Bridgman experiments

From the two previous experiments using the vertical Bridgman method and the inclined Bridgman method we can concluded that: (i) Inclusions are trapped liquids that partly crystallize upon cooling. They always end at the eutectic composition that can be detected at room temperature. (ii) Cracks occur in polycrystalline $FeSb_2$ due to anisotropic thermal expansion coefficients hypothesis: no crack will form, once we obtained single crystals.

Thus, in this section we will focus mainly on finding the adequate conditions to obtain $FeSb_2$ single crystals by using the IRB method either through spontaneous nucleation or crystallization on a seed. To do this, four crystal growth experiments with a starting composition of $Fe_{0.095}Sb_{0.905}$ and $Fe_{0.09}Sb_{0.91}$ (see Table 4.1 for more details) were prepared. These are described as:

- QX580: grown without native seeding,
- QX605: grown using $FeSb_2$ powder in the seed channel,
- QX609: grown using a $FeSb_2$ polycrystalline solid seed,
- QX623: grown using a [100]-oriented $FeSb_2$ single-crystalline seed.

The obtained $FeSb_2$ ingots are shown in Figure 5.3. Here, they are presented with the inclination angle of 15° with respect to the horizontal direction according to the experimental setup. Also, the horizontal surface perpendicular to the gravity vector can be observed in the last approx. 30 mm of each ingot.

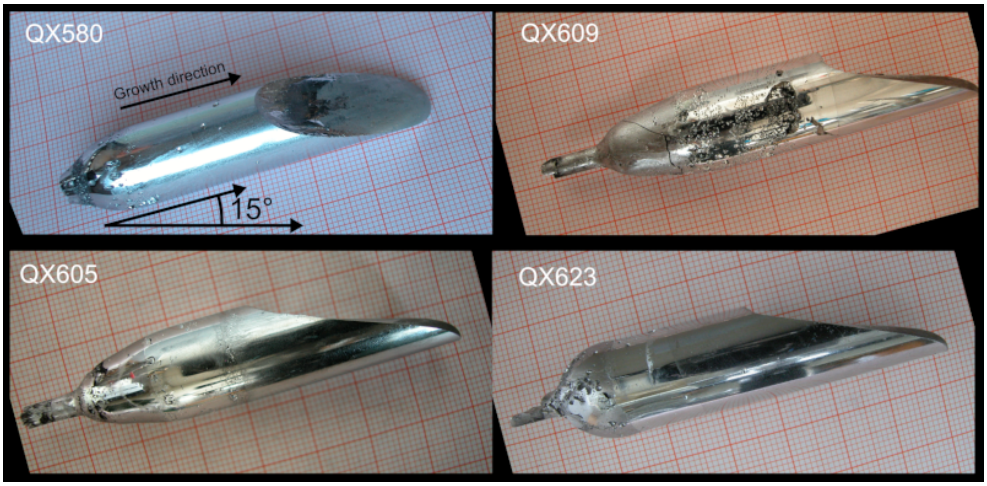

Figure 5.3: Ingots of $FeSb_2$ obtained by the Inclined Rotary Bridgman method without using a seed (QX580) and grown with some kind of seeds (QX605, QX609, and QX623). All ingots are inclined 15° with respect to the horizontal according to the experimental setup.

The length of all the ingots is around 70 mm with a diameter of 15 mm. In the crystals grown by using a seed or some substitute, it can be seen that a part of it remains with the

main body of the ingot. From their outer appearance, the interface between the $FeSb_2$ and the Sb-rich eutectic phases can be distinguished. In the following sections, the first part of each ingot will be analyzed with optical microscope and the structural characterization by XRD of the first-to-freeze will be carried out in some of them.

QX580: IRB without a seed

The longitudinal section of the first part of the ingot QX580 is shown in Figure 5.4. The interface separating the $FeSb_2$ and Sb-rich eutectic phases is slightly concave (see dashed line). Dark colors on the right side of the interface are $FeSb_2$ as well. This results from the termination of the experiment which was done a bit too early before the eutectic composition of the residual melt was exactly reached. Small Sb-inclusions have been found in the upper part of the $FeSb_2$ crystal and near to the interface, but not in the other parts of the crystal. The $FeSb_2$ crystal has a large crack which seems to originate from the bottom edge of the crystal following the growth direction. Other small cracks are also observed. Additionally, in order to have stoichiometric $FeSb_2$ material to be used as seed substitute in further IRB experiments, a second crystal QX595 was prepared by the IRB method under analogous conditions than QX580. From both experiments, large $FeSb_2$ polycrystalline grains were obtained indicating that spontaneous nucleation cannot be used.

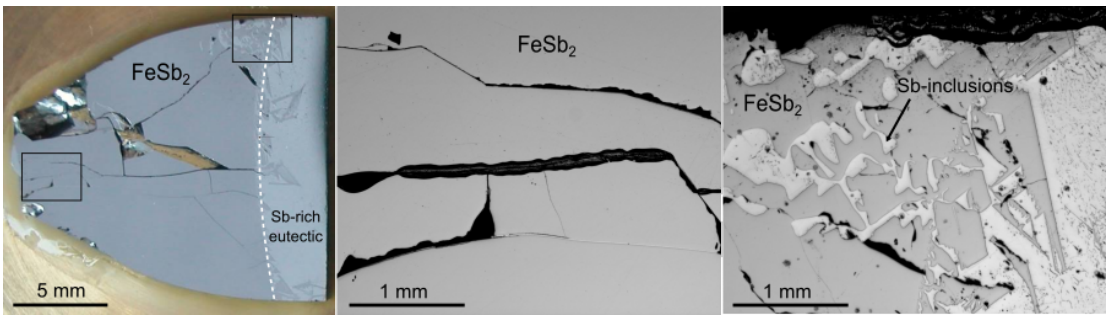

Figure 5.4: Photograph of the longitudinal cut of QX580 with higher magnifications (marked by the black rectangles) at different parts of the crystal. Few amount of small Sb-inclusions have been found in the upper part of the $FeSb_2$ crystal near to the interface. Cracks are also visible.

QX605: IRB with powder seed

For the crystal growth of QX605 with starting composition $Co_{0.09}Sb_{0.91}$ we used $FeSb_2$ powder obtained from the crystal QX595 to fill completely the seed channel in order to start with large grains right from the beginning of growth. The total mass of $FeSb_2$ powder introduced was about 3.2 g. This amount was tested in a separate small tube with the same dimensions than the seed channel since it was not possible to see the actual fill through the carbon layer of the growth ampoule. The first part of the ingot QX605 was axially cut to obtain a slice of 2 mm thickness which was subsequently lapped as shown in Figure 5.5(a), where a part of the seed can also be seen. The seed/crystal interface position is highlighted by the white line. The initial position of this seed/crystal interface was assumed to be at the top of the seed channel but we found that it is around 4 mm below this position. Two large grains instead of one have been grown (see black dashed line). This fact was confirmed with X-ray Laue diffraction images in some of these grains. Their orientations are indicated schematically with different symbols (and colors) in Figure 5.5(a).

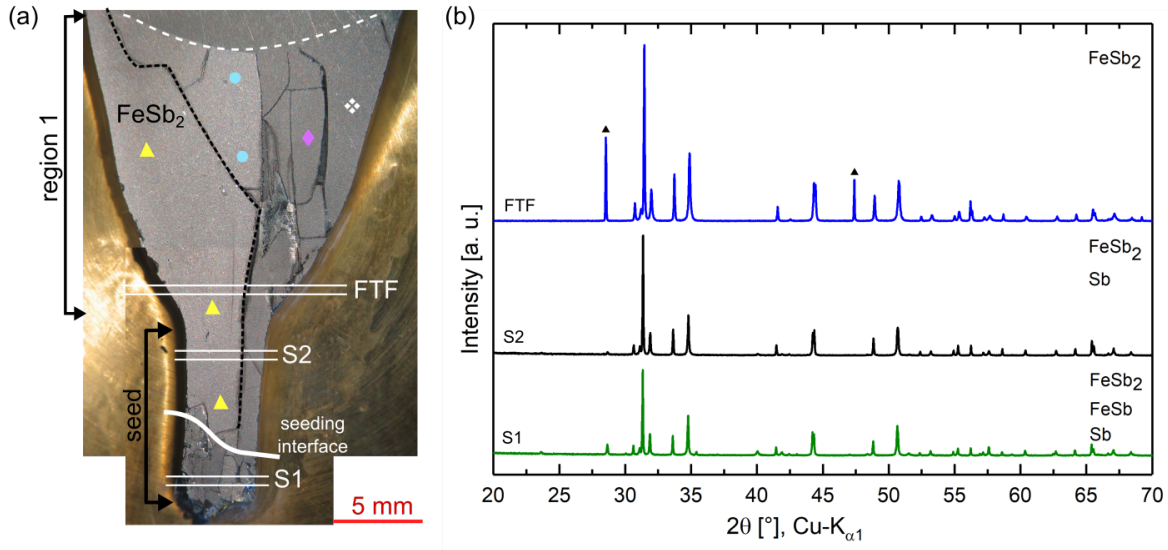

Figure 5.5: (a) Photograph of the axial-longitudinal section of QX605 showing large grains with different orientations as indicated schematically with small symbols in some of them. Large cracks can also be seen. (b) XRD pattern of samples collected from the seed and the region 1. ▲: Si640c internal standard.

Although, we did not get a single crystal of $FeSb_2$ the information of the seed/crystal interface position helped us for further experiments using bulk seeds. Three samples labeled as S1, S2 and FTF (first-to-freeze) were cut from QX605 in order to analyze their phase compositions, see Figure 5.5(b). Apart from the expected $FeSb_2$ phase, S1 sample is composed additionally by FeSb and Sb while S2 sample by only Sb as a second phase. In region 1, FTF sample was identified as single-phase $FeSb_2$.

QX609: IRB with solid seed

For the crystal growth of QX609 with starting composition $Fe_{0.09}Sb_{0.91}$, we use a stoichiometric $FeSb_2$ solid seed which was obtained from the previous experiment (QX605). In particular, it has been used the large single grain from region 1 (see Figure 5.5(a)) such that we practically have a monocrystalline seed with 3.7 mm in diameter and 12 mm in length for this experiment. Since the length of the seed channel is 40 mm, the first part of the seed channel was filled with $FeSb_2$ stoichiometric powder also obtained from QX605. The seed/crystal interface was positioned based on the previous results of QX605.

Figure 5.6 shows the successful growth of a $FeSb_2$ large single crystal with a size of approximately 15 mm in diameter and 15 mm length. No visible cracks as previously reported were observed in this single crystal.

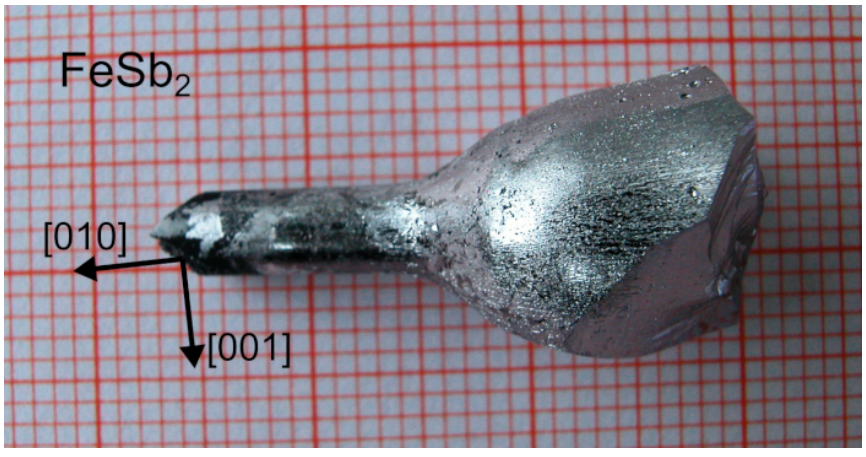

Figure 5.6: Large single crystal of $FeSb_2$ obtained by Inclined Rotary Bridgman method using a solid seed.

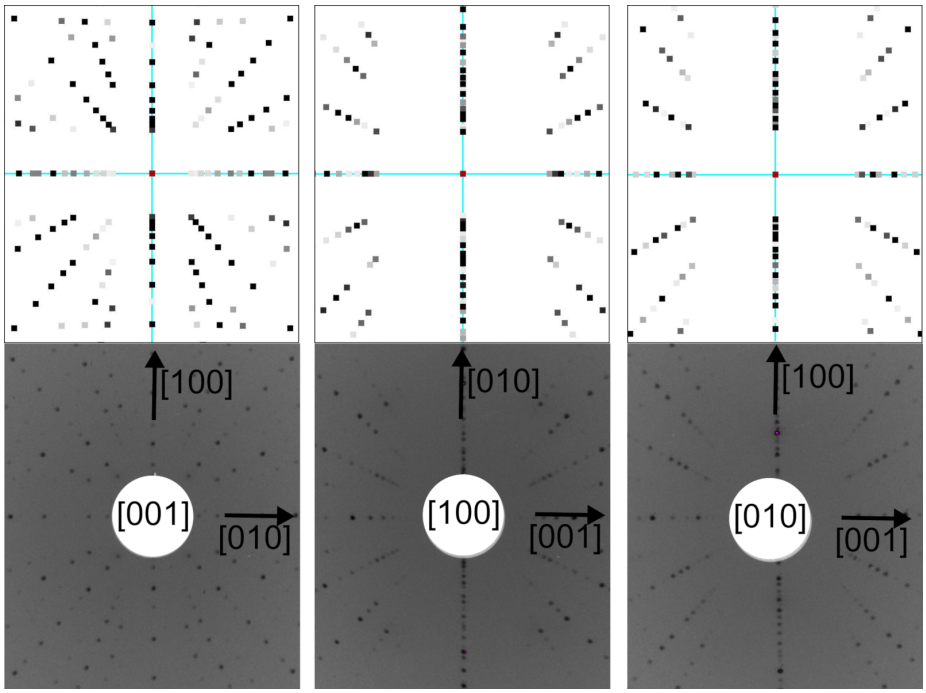

Figure 5.7: Simulated (top) and measured (bottom) X-ray Laue back-scattering diffraction patterns of the large single crystal $FeSb_2$ grown by IRB method. Each primary beam parallel to the [001], [100] and [010] directions.

This may be regarded as a hint, that cracks were the results of different grain orientation in the polycrystals. The single large grain was confirmed with several Laue back-scattering images in the whole crystal and showed that it follows the same orientation than the seed. In figure 5.7, the measured and simulated Laue back-scattering patterns parallel to the main directions of the large single crystal $FeSb_2$ are shown. Further analysis in QX609 was performed on the (010) surface from the single crystal (see inset Figure 5.8). The single crystallinity of $FeSb_2$ is easy to see from the lapped surface. A higher magnification after surface polishing shows the presence of some small Sb-inclusions with irregular shapes.

A sample cut from the first-to-freeze part of QX609 was analyzed by XRD and confirmed the $FeSb_2$ single phase. Further Rietveld analysis of the XRD pattern diffraction (see Figure 5.9) revealed lattice parameters of $a = 5.83082(3)$ Å, $b = 6.53713(6)$ Å, and $c = 3.19831(3)$ Å. These values are very close to the reported by H. Holseth *et al.* [62]. The calculated mass density (Equation 4.3) using these X-ray data, $\rho_{cal} = 8.155(1)$ g/cm^3, was in complete accordance with the experimentally obtained value (Equation 4.2) of $\rho_x = 8.155(3)$ g/cm^3.

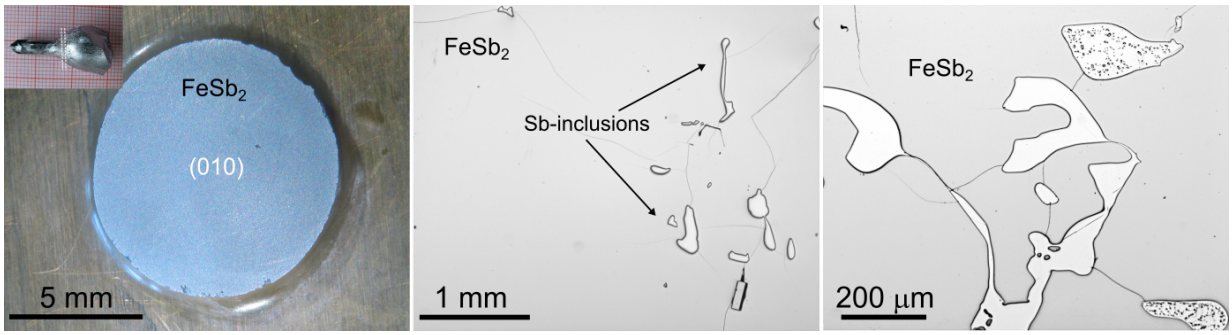

Figure 5.8: (010)-Oriented $FeSb_2$ slice cut of QX609 and light microscope images a different magnifications. Smalls Sb-inclusions and cracks are observed.

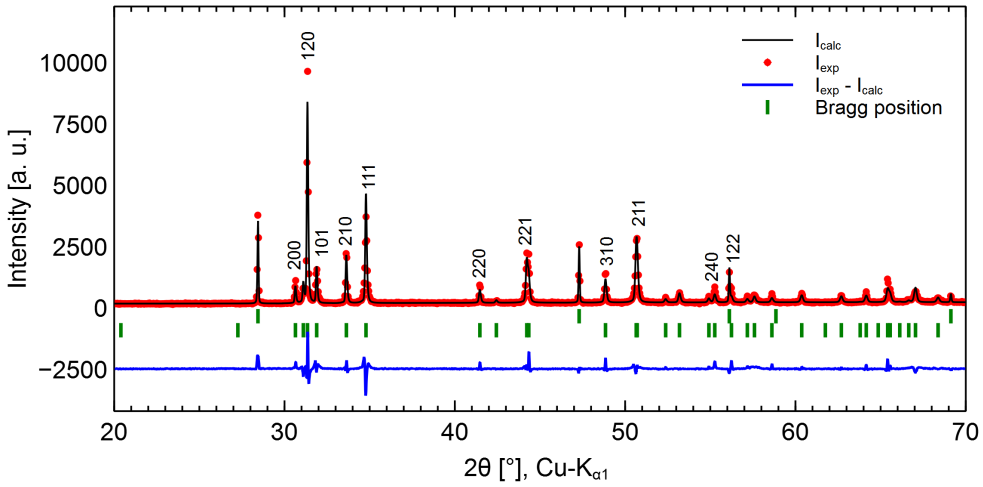

Figure 5.9: Rietveld refinement of the XRD pattern of sample FTF (first-to-freeze) cut from QX609. Only a $FeSb_2$ single phase was found. Observed: red circles, calculated: black line, and difference: blue line at the bottom. Green thick marks indicate the *hkl* reflections for the $FeSb_2$ phase and Si640c internal standard. Rietveld R-factors: $R_p = 27$, $R_{wp} = 23.6$, $R_e = 13.37$, and $\chi^2 = 3.11$.

QX623: IRB with oriented seed

The crystal growth of QX623 was performed under the analogous conditions than QX609 but with an [100] oriented $FeSb_2$ single-crystalline native seed. To check the single-crystallinity of QX623, X-ray Laue back-scattering images were taken in several positions (e.g., M1, M2 and M3) and showed different grain orientations as it can be seen

in Figures 5.10(a) and (b). The different grain orientations in QX623 are sketched in Figure 5.10(c). From these results we can conclude that the reproducibility of seeding for single crystal growth of $FeSb_2$ was difficult. This might be related to the fact that the oriented seed was not completely inserted inside the seed channel due to some $FeSb_2$ powder, used to fill the first part of the channel, stuck in the channel. As a consequence, when the solid seed is remelted these powder can also act as nuclei generating more than one $FeSb_2$ grains. This problem can be solved when reducing a bit more the diameter of the solid seed for further experiments.

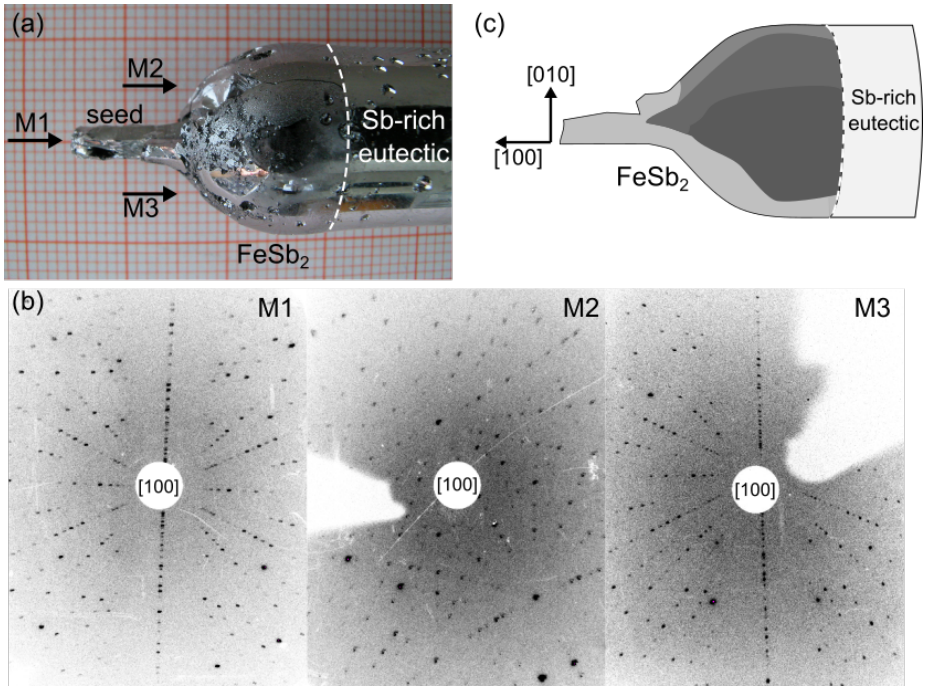

Figure 5.10: (a) Part of the ingot QX623 showing the $FeSb_2$ crystal together with a small portion of the [100] oriented seed. (b) X-ray Laue back-scattering images measured at different positions of the crystal. (c) Schematic sketch of the poly-grains in $FeSb_2$. The gradient of colors means different grain orientations.

In brief, the Inclined Rotary Bridgman (IRB) method showed a much better performance comparing to the other Bridgman arrangements for producing $FeSb_2$ single crystals with few Sb-inclusions and cracks-free. Specially, the efficiency of this method was found to be optimal when we used a $FeSb_2$ polycrystalline solid seed. Consequently, based on the experience gained with the growth of $FeSb_2$, in the next section, we will study the influence of Co doping in $FeSb_2$ compounds by using IRB method.

5.2 $Fe_{1-x}Co_xSb_2$

To determine a convenient starting composition for the crystal growth of the solid solution $(Fe, Co)Sb_2$, small-scale vertical Bridgman experiments were carried out at different concentrations of cobalt.

5.2.1 Vertical Bridgman experiments

Four crystals with starting compositions $(Fe_{1-x_0}Co_{x_0})_{0.10}Sb_{0.90}$, $0.1 \leq x_0 \leq 0.5$, were prepared by the small-scale vertical Bridgman method. The as-grown ingots shown in Figure 5.11 have smooth and shiny metallic-like surfaces, without a notable difference in their outer appearance if compared to the binaries The ingots were 8 mm in diameter and around 25 mm in length. Here, the interface between $(Fe, Co)Sb_2$ and the Sb-rich eutectic fabric is easy to be seen. To study the phases formed in the crystals, the first-to-freeze part was cut out from each ingot and analyzed by X-ray diffraction. The microstructure and EPMA analysis were carried out in the rectangle area indicated in Figure 5.11 after cutting the ingots in half along the growth direction with subsequent polishing process.

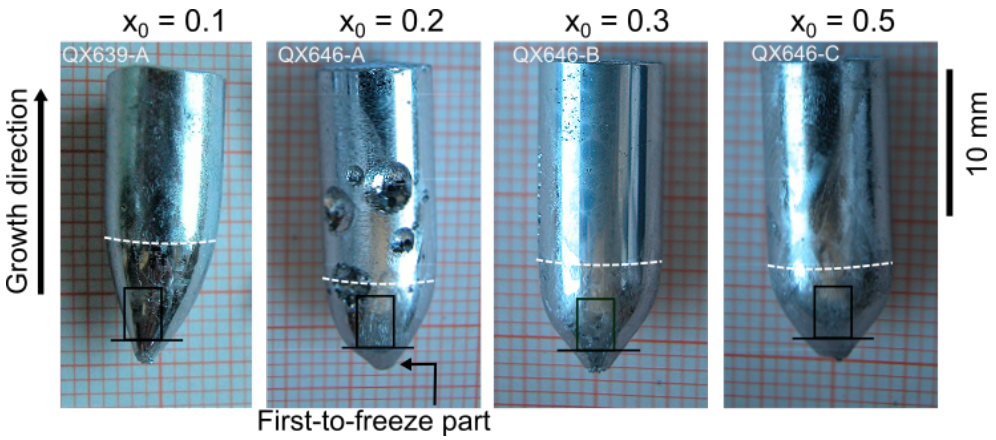

Figure 5.11: Ingots of $Fe_{1-x}Co_xSb_2$ obtained by small-scale vertical Bridgman method from starting compositions $(Fe_{1-x_0}Co_{x_0})_{0.10}Sb_{0.90}$, $0.1 \leq x_0 \leq 0.5$. White dashed lines (below) and rectangle areas mark the analyzed regions. Small bubbles for $x_0 = 0.2$ comes from the vapor trapped during crystallization.

Microstructure and EPMA

Figure 5.12 shows the microstructures of the polished surface of $Fe_{1-x}Co_xSb_2$ in combination with EPMA measurements. The microstructures mainly consist of a large dark grey areas that are separated by a lot of cracks, which decrease with the increment of Co and nearly disappear for the highest content of Co ($x_0 = 0.5$) in the starting melt composition.

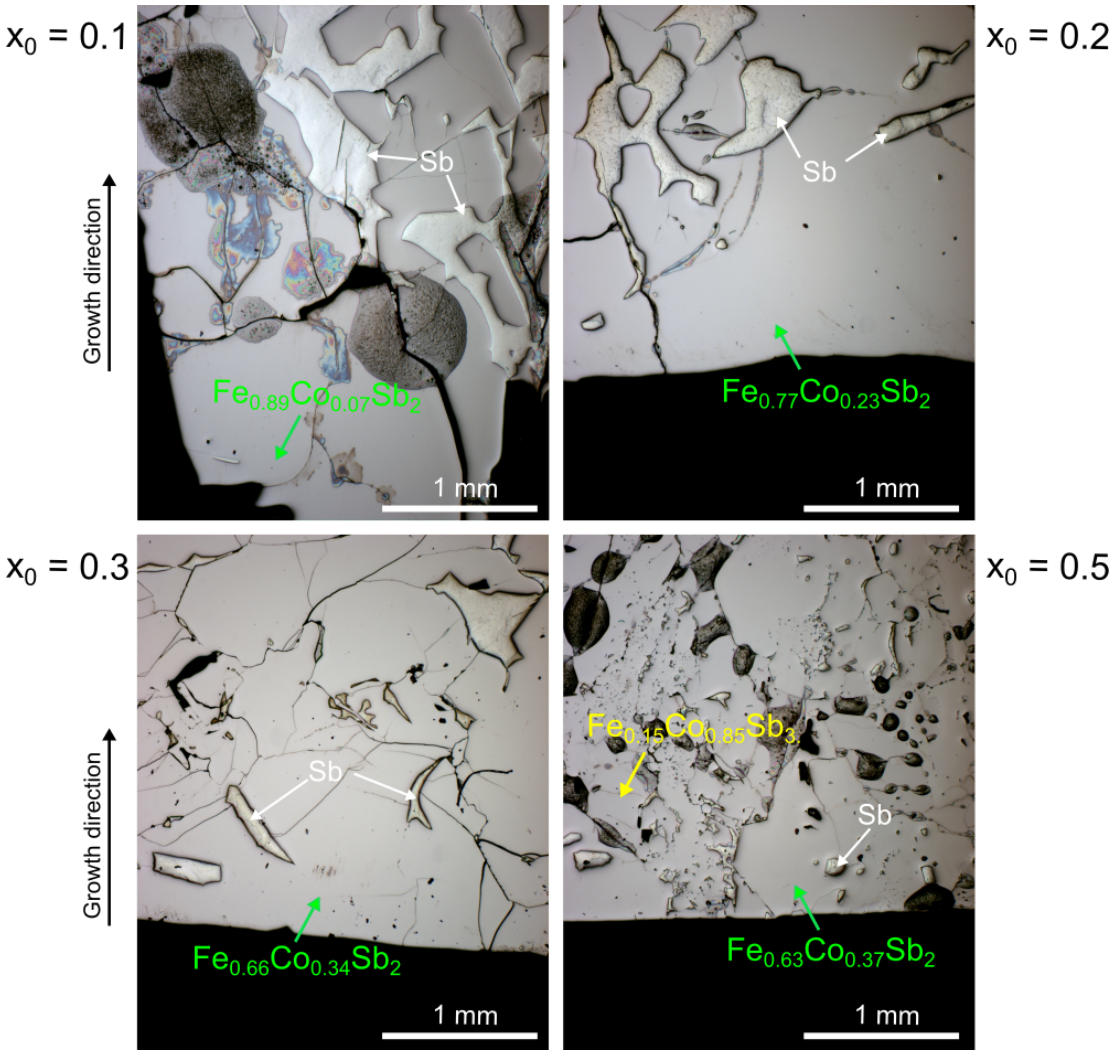

Figure 5.12: Light microscope images of part of the longitudinal sections of $Fe_{1-x}Co_xSb_2$ with starting compositions $(Fe_{1-x_0}Co_{x_0})_{0.10}Sb_{0.90}$, $0.1 \leq x_0 \leq 0.5$, grown by vertical Bridgman method. White arrows indicate Sb-inclusions. Compositions of the first-to-freeze phases are also shown for each case.

In addition, we found a few light grey areas that were identified as Sb-inclusions. The different shades on these light grey areas are related to a very small amount of about 0.02 at.% of Fe(Co) in their structure (see Appendix Figure A.1). The chemical composition in the large dark grey areas were analyzed by EPMA in point mode by averaging over 5 to 15 different points. The resulting first-to-freeze phases as well as the starting melt compositions are shown in Figure 5.12 and summarized in Table 5.1.

Table 5.1: Composition of the first-to-freeze phases of $Fe_{1-x}Co_xSb_2$ determined by EPMA. Starting melt compositions $(Fe_{1-x_0}Co_{x_0})_{0.10}Sb_{0.90}$ for each crystal are also shown

Sample code	Starting melt	Fe [at.%]	Co [at.%]	Sb [at.%]	First-to-freeze phase*
QX639-A	$(Fe_{0.9}Co_{0.1})_{0.10}Sb_{0.90}$	29.8	2.5	68.0	$Fe_{0.93}Co_{0.07}Sb_2$
QX646-A	$(Fe_{0.8}Co_{0.2})_{0.10}Sb_{0.90}$	24.7	7.5	67.8	$Fe_{0.77}Co_{0.23}Sb_2$
QX646-B	$(Fe_{0.7}Co_{0.3})_{0.10}Sb_{0.90}$	21.3	11.1	67.6	$Fe_{0.66}Co_{0.34}Sb_2$
QX646-C	$(Fe_{0.5}Co_{0.5})_{0.10}Sb_{0.90}$	20.5	12.0	67.6	$Fe_{0.63}Co_{0.37}Sb_2$
		3.6	21.2	75.2	$Fe_{0.15}Co_{0.85}Sb_3$

*Normalized to Sb = 2 for $(Fe, Co)Sb_2$, and Sb = 3 for $(Fe, Co)Sb_3$. (Fe + Co) = 1.

X-ray analysis

X-ray diffraction patterns of the first-to-freeze part of all $Fe_{1-x}Co_xSb_2$ crystals are shown in Figure 5.13. For comparison, data of $FeSb_2$ ($x = 0$) corresponding to QX609 is included. These results are in agreement with the ones obtained by EPMA, confirming the primary crystallization of a single-phase of the solid solution $(Fe, Co)Sb_2$ for $0.1 \leq x_0 \leq 0.3$. Decomposition into two phases for $x_0 = 0.5$ identified as the solid solutions $(Fe, Co)Sb_2$ and $(Fe, Co)Sb_3$ was observed. It means that the limit of substitution of Fe by Co in $(Fe, Co)Sb_2$ is lower than 0.5. A closer look around the two main peaks of the X-ray diffraction patterns within the 2θ range 11° - 18° (see right panel Figure 5.13) allows us to observe better the effect of incorporation of Co in the crystal structure of $FeSb_2$. Three things are worth to mention here: first, the shift of the peaks 120 and 210 toward the higher angle, which indicates the decrease of the lattice

parameters in $FeSb_2$. Second, the merge of the peaks 120 and 101. Similar tendency was observed in most of the peak doublets (e.g. at $2\theta = 29°$ and $2\theta = 34°$). Third, for $x_0 = 0.5$ the former peaks 011 and 210 merge completely indicating a change of crystal structure. In addition, new peaks appear which were identified as a solid solution $(Fe, Co)Sb_3$.

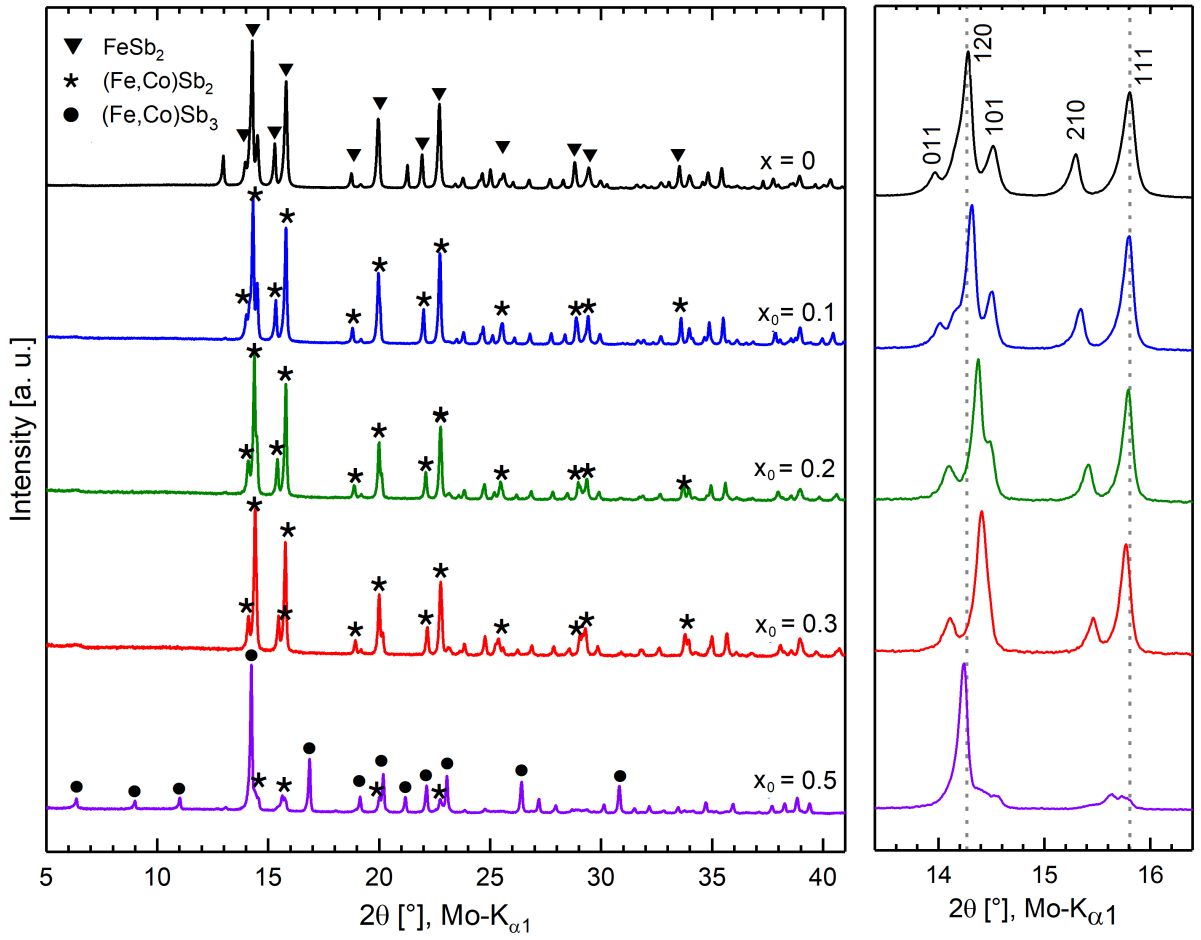

Figure 5.13: (Left) X-ray diffraction patterns of the crystals $Fe_{1-x}Co_xSb_2$ for different starting concentrations of Co. The first reflection in $x = 0$ corresponds to the Si640c standard. A single-phase $(Co, Fe)Sb_2$ solid solution was found for $0.1 \leq x_0 \leq 3$. (Right) Local zoom around the two main peaks of the XRD patterns.

To gain insight into the structural changes of $FeSb_2$ after Co doping, a Rietveld refinement analysis was performed in the XRD patterns of Figure 5.13. Rietveld

refinements were performed using the orthorhombic $FeSb_2$ phase (m-type structure) for the solid solution $(Fe, Co)Sb_2$ and the cubic $CoSb_3$ phase for the solid solution $(Fe, Co)Sb_3$. The refined cell parameters as well the weighted-profile R-factors and χ^2 are listed in Table 5.2 (see Figure A.2 for fitted patterns).

Table 5.2: Summary of the refinement parameters for the crystal $Fe_{1-x}Co_xSb_2$ with starting compositions $(Fe_{1-x_0}Co_{x_0})_{0.10}Sb_{0.90}$, $0.1 \leq x_0 \leq 0.5$, obtained by vertical Bridgman method.

x_0	0.1	0.2	0.3	0.5
Cell parameters				
a (Å)	5.8131(1)	5.7911(2)	5.7712(2)	5.7412(6)
b (Å)	6.5221(1)	6.5064(2)	6.4923(2)	6.4631(6)
c (Å)	3.2052(1)	3.2188(1)	3.2290(1)	3.2504(4)
V (Å^3)	121.52	121.33	120.98	120.6
ρ (g/cm^3)	8.190	8.214	8.243	8.269
Rietveld factors				
R_p	10.8	15.7	18.4	18.8
R_wp	10.8	16.3	17.9	20.4
R_e	7.98	13.06	15.01	11.40
χ^2	1.85	1.57	1.43	3.21

The c-parameter increases slightly but the a- and b-parameters decrease strongly, resulting in an overall decrease of the unit cell volume (see Figure 5.14). Additionally, the smooth linear dependence of the lattice parameters as function of the Co concentration, demonstrates that Co atoms successfully substitute the Fe atoms in the entire solid solution range. These results are in agreement with the literature [26, 105]. The higher standard deviation of the refined cell parameters for $x = 0.5$ indicates that the initial orthorhombic $FeSb_2$ model is not the correct one to fit this data. Thus, a structural transformation from orthorhombic $Pnnm$ to the pseudo-marcasite monoclinic $P2_1/c$ structure of $CoSb_2$ is confirmed for $x_0 = 0.5$.

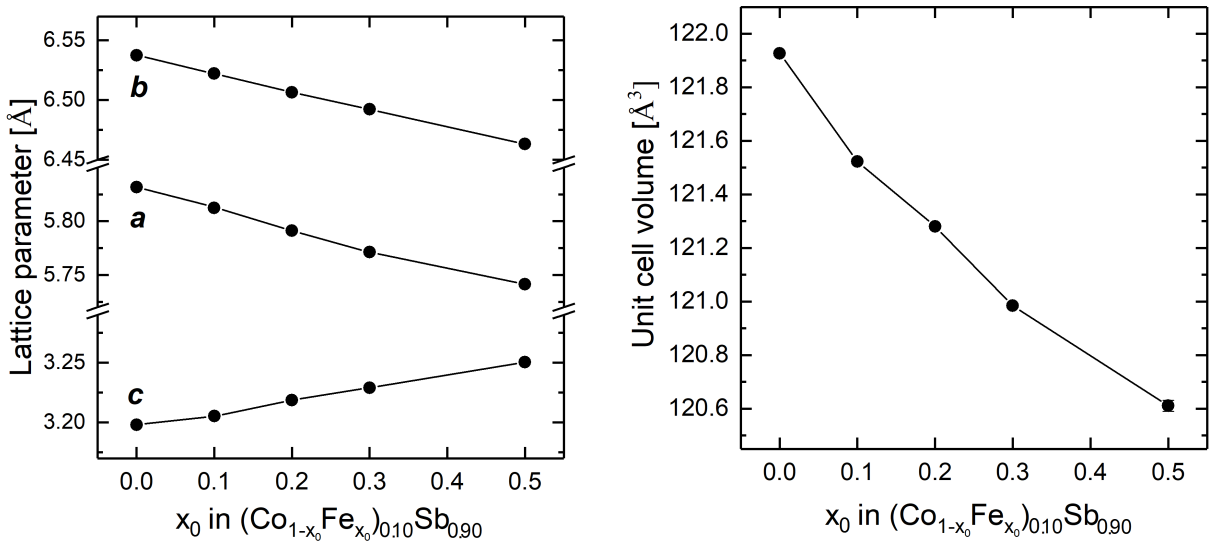

Figure 5.14: Refined lattice parameters and unit cell volume of $Fe_{1-x}Co_xSb_2$ versus mole fraction x_0 in the starting composition $(Fe_{1-x_0}Co_{x_0})_{0.10}Sb_{0.90}$. Error bars are smaller than the width of the plotted symbols.

5.2.2 Inclined Rotary Bridgman experiment

Once having found the limit of substitution of Fe by Co in $(Fe, Co)Sb_2$, we decided to grow the solid solution $(Fe, Co)Sb_2$ from a starting composition $(Fe_{0.9}Co_{0.1})_{0.10}Sb_{0.90}$, i.e., $x_0 = 0.1$, by using the Inclined Rotary Bridgman method. Based on the previous experience using IRB method (see Section 5.1.3), we used $FeSb_2$ powder seed substitute to grow this crystal. Figure 5.15 shows the as-grown ingot of $Fe_{1-x}Co_xSb_2$ obtained from a starting composition $(Fe_{0.9}Co_{0.1})_{0.10}Sb_{0.90}$ (crystal QX645). After taking the ampoule out of the furnace, we observed that the ampoule was cracked (see Figure 5.15(a)). This effect is due to the anisotropy of the thermal expansion of $FeSb_2$. The crack in the ampoule can be avoided if the growth ampoules are covered with carbon layer.

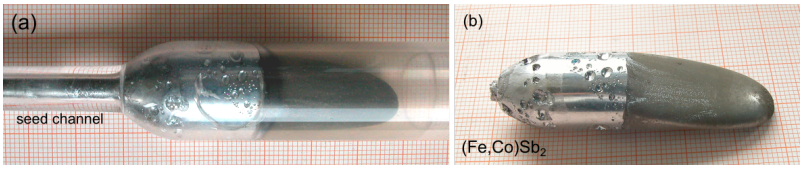

Figure 5.15: Ingot of $Fe_{1-x}Co_xSb_2$ in (a) and (b) out of the growth ampoule. Small cracks can be observed in the ampoule.

Microstructure and EPMA

The first part of the as-grown ingot ($\sim$ 25 mm) was cut off and sectioned longitudinally into two halves. One of them was lapped (see Figure 5.16(a)) and from the other half a 2 mm thick slice was cut out (see Figure 5.16(b)).

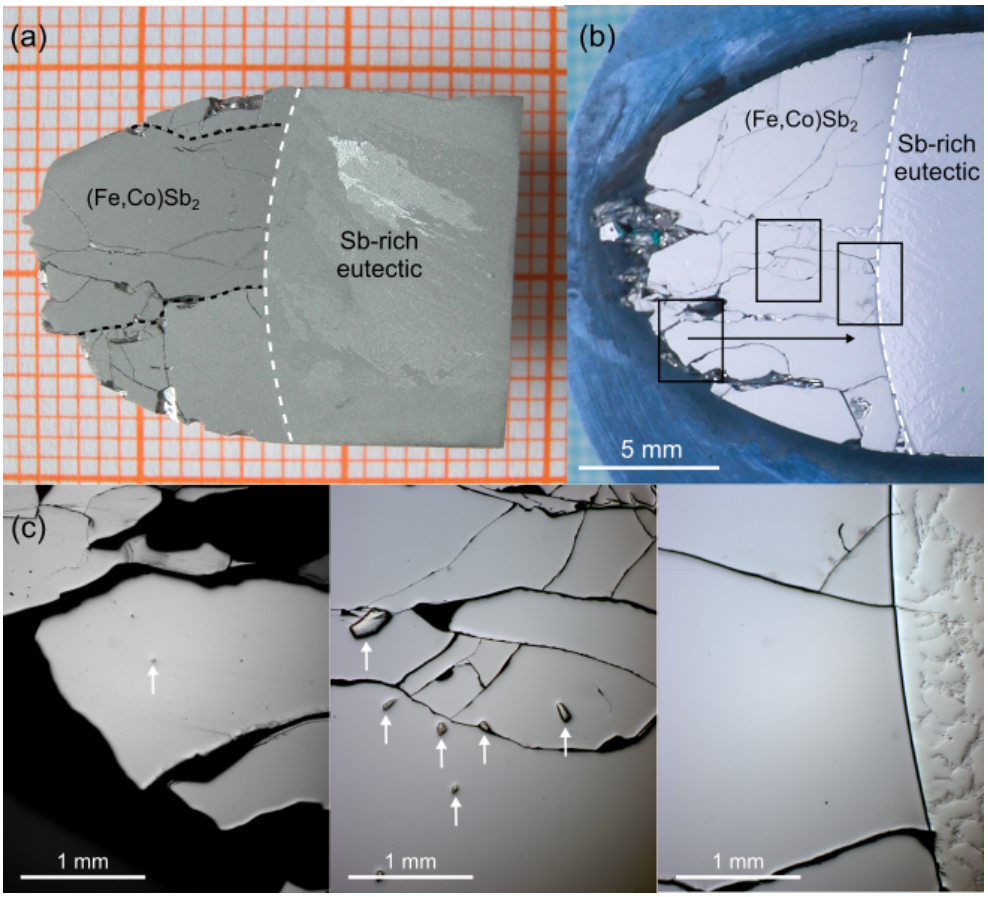

Figure 5.16: Photographs of the longitudinal section of the (a) lapped and (b) polished surfaces of $Fe_{1-x}Co_xSb_2$ obtained from a starting composition $(Fe_{0.9}Co_{0.1})_{0.10}Sb_{0.90}$. Three large grains with a lot of cracks are evident in the lapped surface. (c) Light microscope images showing the Sb-inclusions indicated with white arrows and the composition of the crystals.

From the lapped surface of the sample $Fe_{1-x}Co_xSb_2$, three big grains can clearly be identified which are separated by large cracks that are nearly parallel to the growth direction (see dashed black lines). Each of these grains contain small single crystals also separated by cracks that are observed in the corresponding light microscope images of the

other half side in Figure 5.16(c). Indeed, X-ray Laue diffraction measurements of some of these grains confirm this observation. The interface indicated with white dashed lines is slightly concave, and from the magnification it can be observed that it is well defined. This means that all the Co and Fe atoms were consumed for the grown crystal.

The chemical composition of the solid solution $Fe_{1-x}Co_xSb_2$ obtained from a starting melt composition $(Fe_{0.9}Co_{0.1})_{0.10}Sb_{0.90}$ was analyzed by EPMA in line profile mode, from the bottom of the crystal to the interface as is indicated by the black arrow in the same Figure 5.16(b). The results are shown in Figure 5.17, and it can be seen that Co substitutes for Fe while Sb concentration remains unchanged.

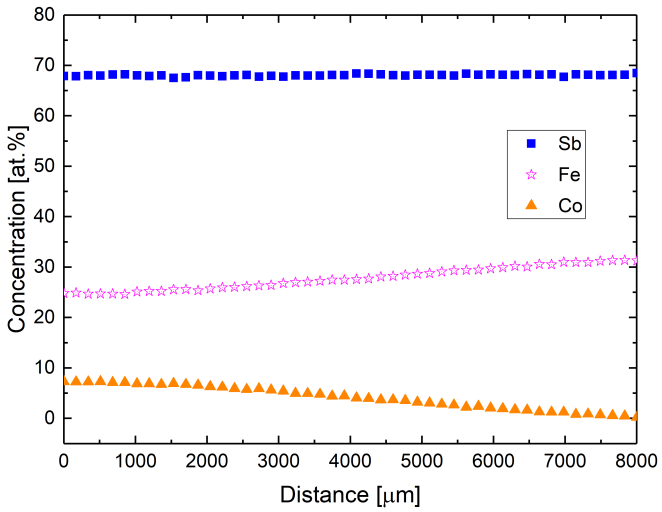

Figure 5.17: EPMA line profiles of Co, Fe and Sb concentrations obtained for the crystal $Fe_{1-x}Co_xSb_2$ with starting melt composition $(Fe_{0.9}Co_{0.1})_{0.10}Sb_{0.90}$. Decreasing Co composition along the growth.

X-ray analysis and Rietveld refinement

The X-ray powder diffraction pattern of a sample taken from near to the first-to-freeze part of the crystal is shown in Figure 5.18. Here, only single-phase solid solution $(Fe, Co)Sb_2$ was found, corroborating the results obtained by the vertical Bridgman experiment. All the peaks were indexed according to the orthorhombic $FeSb_2$ *m*-type crystal structure. Inset of Figure 5.18 shows the comparison of both XRD patterns of the solid solution $(Fe, Co)Sb_2$ and $FeSb_2$ (obtained in former experiments) around the two main peaks. We observed a slight shift of some peaks toward higher angles, which indicates the decreasing

of the cell parameters due to the incorporation of Co into the crystal structure of $FeSb_2$. A Rietveld analysis of the XRD data was performed and the result of the refined cell parameters, weighted-profile R-factors and χ^2 are listed in Table 5.3. Here, the refined lattice parameters and the cell volume were quite comparable with the values obtained in the crystal with nominal Co content $x_0 = 0.2$ grown by VB method.

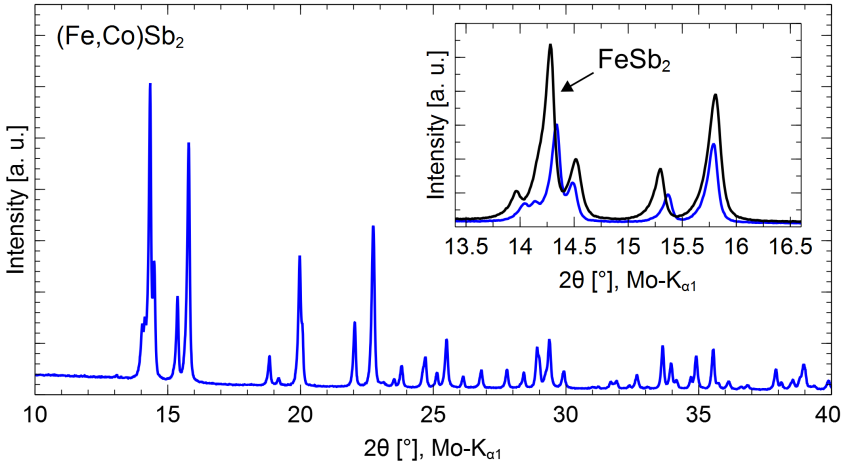

Figure 5.18: X-ray diffraction pattern of $(Fe, Co)Sb_2$ crystal obtained from a starting composition $(Fe_{0.9}Co_{0.1})_{0.10}Sb_{0.90}$ by the IRB method. Inset shows the comparison with $FeSb_2$ around the two main peaks.

Table 5.3: Refined cell parameters obtained from the Rietveld refinement of the solid solution $(Fe, Co)Sb_2$ (crystal QX645) grown by the Inclined Rotary Bridgman method from a starting composition $(Fe_{0.9}Co_{0.1})_{0.10}Sb_{0.90}$.

Parameters	QX645
a (Å)	5.8054(1)
b (Å)	6.5177(1)
c (Å)	3.2128(1)
V (Å^3)	121.56
ρ_{calc} (g/cm^3)	8.283
R_p	11.9
R_{wp}	12.2
R_e	6.92
χ^2	3.11

Chapter 6

Large $CoSb_3$ and In-doped $CoSb_3$ single crystals

In the previous chapter, the efficiency of the Inclined Rotary Bridgman method for growing single crystals was shown. Thus, in the present chapter, we will use this knowledge to grow $CoSb_3$ and In-doped $CoSb_3$ compounds, which present potential applications in the thermoelectric industry. Hence, the electrical and magnetic properties of both compounds will be also presented and discussed.

6.1 $CoSb_3$

6.1.1 Vertical Bridgman experiments

In the Section 7.2, it will be shown that in vertical Bridgman configurations, there is only a very weak buoyancy-driven convection but this was not enough to ensure homogeneous mixing in the melt leading to inclusion formation of Sb-rich melt in the grown crystal. Thus, inclusion formation is here not a matter of concern. Hence, we discuss only the starting compositions for $CoSb_3$ first-to-freeze that can be independent of Sb-rich inclusions. As it is known prior to experiments only small part can be crystallized as $CoSb_3$ and the rest will be an eutectic structure of almost pure Sb (see phase diagram Figure 2.5). However, in order to get a microstructural insight of the as-grown ingots some of them were axially cut along the growth direction obtaining slices of 2 mm thickness.

Preliminary small-scale vertical Bridgman experiments were carried out to determine

the correct starting composition to obtain $CoSb_3$ single-phase material. In total, eight crystals with starting compositions $Co_{1-x_0}Sb_{x_0}$ ($0.915 \leq x_0 \leq 0.950$) were prepared, and some of them are shown in Figure 6.1. The ingots are 8 mm in diameter and around 20-30 mm in length with shiny surfaces and metallic-like. The white/green layer observed in the ingots with starting composition > 93 at.%Sb is due to reaction of these ingots with the glass ampoule. This layer was identified as low-cristoballite SiO_2. Here, the oxygen may come from a bad etching process of the Co metal. Nevertheless, these crystals were also studied after removing the white/green layer.

The first-to-freeze part (region below the dashed lines in Figure 6.1) was cut from each ingot to study the corresponding primarily crystallized phases by X-ray diffraction. Because of the bottom shape of the ingots (conical and round), the amount of material extracted from each first-to-freeze part is different. Thus, only qualitative analysis was done without further Rietveld refinement.

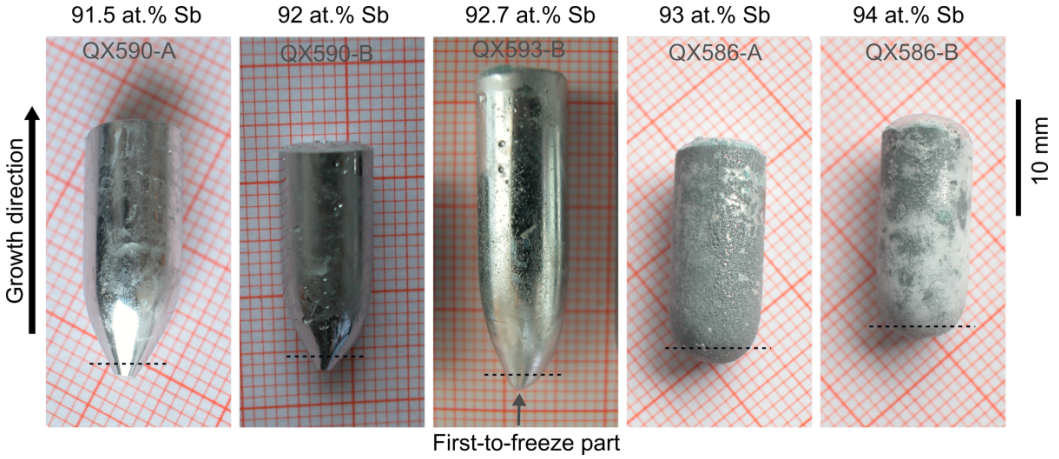

Figure 6.1: Some ingots of $CoSb_3$ with different starting compositions $Co_{1-x_0}Sb_{x_0}$ ($0.915 \leq x_0 \leq 0.950$) prepared by a small-scale vertical Bridgman method. First-to-freeze parts (region below the dashed lines) were cut for phases analysis.

Microstructure

Figure 6.2 (upper part) shows the axial cut of the polished surfaces of three crystal QX586-A, B, C which are independent crystals with $Co_{0.07}Sb_{0.93}$, $Co_{0.06}Sb_{0.94}$, $Co_{0.05}Sb_{0.95}$ starting compositions, respectively. As mentioned before, a large number of

Sb-inclusions are present in the $CoSb_3$ phase, which corresponds to the first 5-6 mm from the bottom of the ingots. The rest of the ingots corresponds to the Sb-rich eutectic phase, i.e., practically pure Sb. In general, only approx. 25 % of the total volume of the ingot consists of $CoSb_3$. Light microscope image of the ingots, see Figure 6.2 (lower part), shows significant differences in structure and grain boundaries. For the starting composition 93 at.% Sb, small and large $CoSb_3$ grains with round edges are surrounded by a matrix of Sb-inclusions. The large grains with columnar shapes are elongated in the growth direction. This transition from small to large grains is related to the constitutional supercooling. However, for 94 at.% Sb and 95 at.% Sb, grain coarsening leads $CoSb_3$ to form a densely packed structure trapping large Sb-inclusions with irregular shapes. In 95 at.% Sb the irregular Sb-eutectic structure is clearly observed.

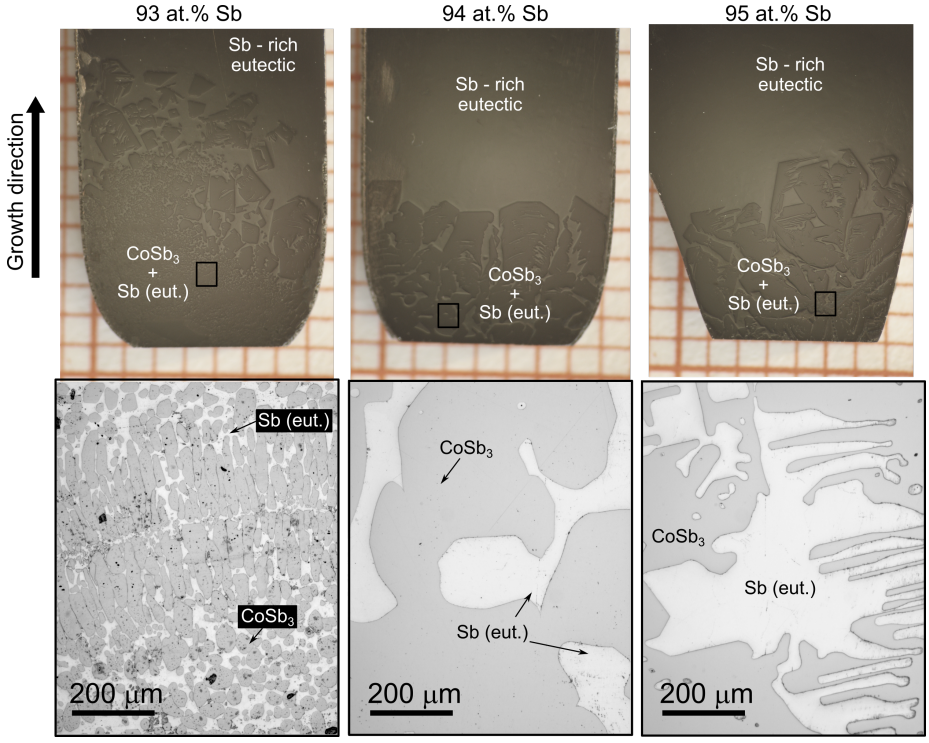

Figure 6.2: Optical micrographs (upper) and light microscope images (lower) of the polished surface of QX586 with starting compositions 93 at.% Sb, 94 at.% Sb and 95 at.% Sb. Sb-inclusions are observed in all crystals.

In general, similar to $FeSb_2$, these Sb-rich inclusions can be easily explained by the incongruent crystallization with a large excess of Sb in the liquid phase (see Co-Sb phase diagram in Figure 2.5) M. Akasaka *et al.* [56] also reported a high content of these Sb-rich

inclusions when growing $CoSb_3$ from Sb-rich solutions (with 90 at.% Sb) by normal freezing. They found a good correlation of the density of inclusions to the pulling rate which is expected from constitutional supercooling.

XRD analysis

Figure 6.3 shows the X-ray powder diffraction patterns of the first-to-freeze part of the starting compositions $Co_{1-x_0}Sb_{x_0}$. Three phases were identified with the ICSD N° 62110, 42614 and 9859 which correspond to $CoSb_3$, $CoSb_2$, and Sb, respectively.

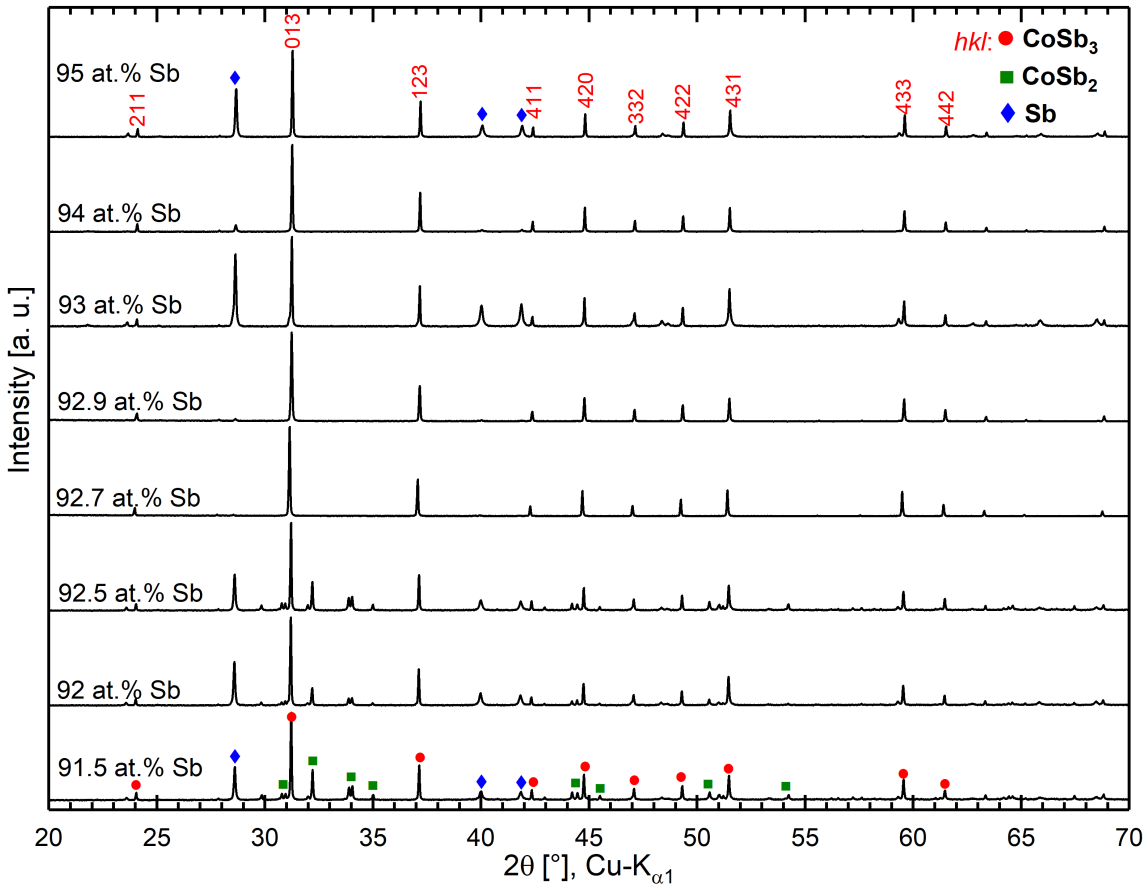

Figure 6.3: X-ray powder diffraction patterns of the first-to-freeze parts of the as-grown ingots crystallized from starting compositions $Co_{1-x_0}Sb_{x_0}$ ($0.915 \leq x_0 \leq 0.950$). Primary crystallization of $CoSb_3$ is obtained only with Sb contents higher than 92.5 at.%. Unavoidable pure antimony arising from Sb-rich inclusions can be found in all samples.

The appearance Sb can be ignored since it comes from the trapped Sb-rich inclusions. From the XRD data, it can be seen that traces of $CoSb_2$ are observed in the grown crystals with starting compositions less than 92.5 at.% Sb. Meanwhile, crystals with higher or equal concentration than 92.7 at.% Sb result in exclusively primarily crystallized $CoSb_3$. The presence of $CoSb_2$ in vertical Bridgman experiments can be explained by a primary solidification of $CoSb_2$ resulting from a starting composition corresponding to a liquidus temperature slightly above the peritectic one. According to the published phase diagram [48] (see Figure 2.5), the respective peritectic reaction $CoSb_2 + Liquid \rightleftharpoons CoSb_3$ occurs with a melt containing 90 at.% Sb at temperature of 874 °C. Instead, the corrected composition of the peritectic melt found in the present study is 92.7 at.% Sb.

6.1.2 Inclined Rotary Bridgman (IRB) experiment

Based on previous results, and to ensure that no $CoSb_2$ phase is formed, we used a starting composition of 93 at.% Sb ($Co_{0.07}Sb_{0.93}$) for all further growth experiments of $CoSb_3$. Similar to the procedure performed for the $FeSb_2$ compounds, three different types of growth experiments were carried out using the Inclined Rotary Bridgman method:

- Growth without a native seeding: QX591,
- Growth using a stoichiometric $CoSb_3$ powder as subtitute for a seed: QX620,
- Growth using a $CoSb_3$ polycrystalline seed: QX625.

In the following, we will show the results of the structural characterization of each crystal mainly focusing on the study of the longitudinal sections.

QX591: IRB without seed

The resulting ingot QX591 is shown in Figure 6.4. The ingot slid out from the ampoule without sticking to the walls. From its outer appearance and based on the daylight reflection, the approx. first 15 mm starting from the bottom of the ingot consists a single-phase material that was identified as $CoSb_3$ (see blue arrows); while the rest being the Sb-rich eutectic fabric. This crystal will be compared with crystal QX588, which was grown under the analogous conditions.

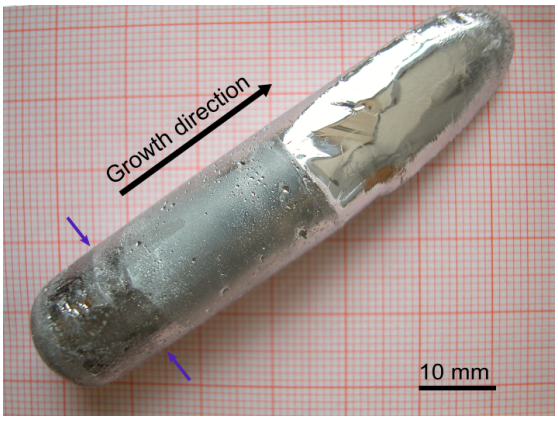

Figure 6.4: Ingot QX591 grown by the Inclined Rotary Bridgman method without using a native seed. Only approx. 25% of the total ingot consists of $CoSb_3$, see blue arrows position, and the rest is the Sb-rich eutectic fabric.

Microstructure

To have a look to their microstructures both ingots were first cut off perpendicular to the ingot's axis (5-10 mm above the blue arrows in Figure 6.4), and second, a 2 mm thick slice parallel to the growth direction was cut. The two slices were lapped as can be seen in Figure 6.5. From left to right three regions can be identified. Region 1, the very first part of the ingot (approx. 4 mm) starts with several small grains of $CoSb_3$.

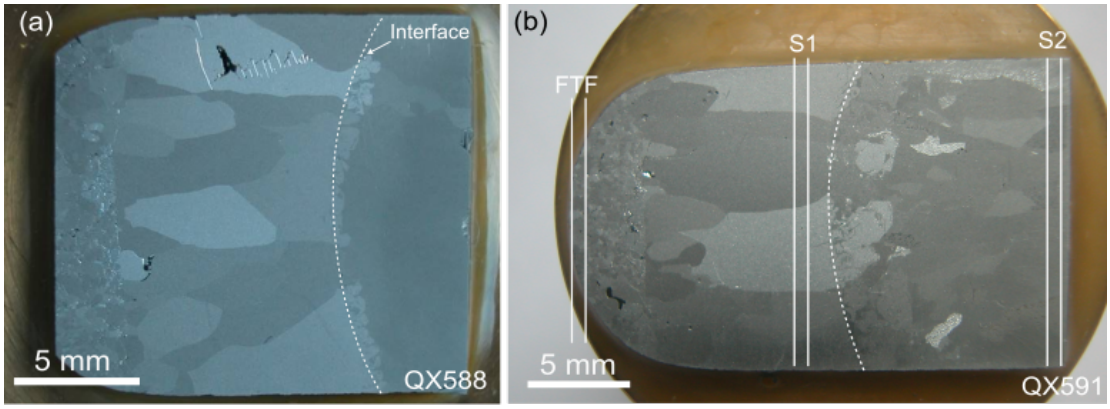

Figure 6.5: Photographs of the lapped surface of crystals (a) QX588 and (b) QX591 showing the fine- and large-grained structures of the polycrystalline $CoSb_3$. White dashed lines represent the interface between $CoSb_3$ and Sb-rich eutectic fabric.

Then, in region 2, larger columnar grains of about 2-9 mm length and 1-3 mm width begin to grow parallel to the growth direction but in different crystallographic orientations. This is due to sudden breakdown of supercooling of the starting melt after nuclei have formed by spontaneous nucleation. The clear boundary between fine- and large-grained structures marks the shape of the isotherm. In these regions neither cracks nor Sb-inclusions were found. Finally, the typical Sb-rich eutectic phase (region 3) is observed after the growth interface. The interface has a concave shape from the viewpoint of the crystal with a deflection about 1.8 mm and 1.5 mm for QX588 and QX591, respectively.

XRD analysis

X-ray powder diffraction measurements were carried out in three samples that were cut off from the first-to-freeze part, FTF, below the interface, S1, and above the interface, S2, of QX591 as indicated in Figure 6.5(b). The results are shown in Figure 6.6.

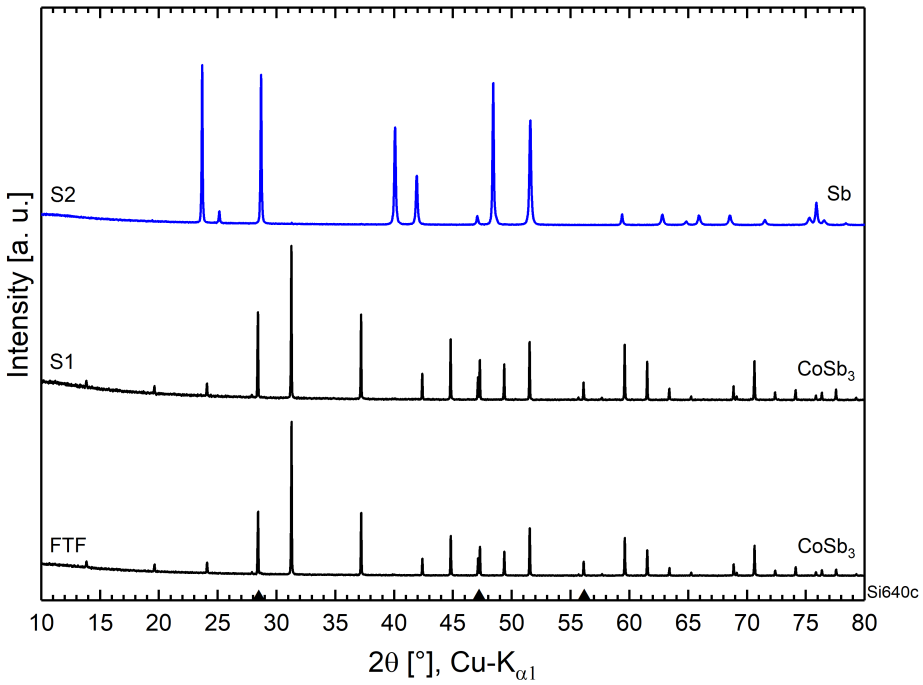

Figure 6.6: XRD patterns of samples cut from different positions of crystal QX591. No secondary phase such as Sb was observed in FTF and S1 samples. Black triangle marks the peak positions of Si640c internal standard.

The two first samples FTF and S1 confirmed the $CoSb_3$ single-phase status, while the sample S2 shows the Sb phase, as it is expected from the Sb-rich eutectic region. In the XRD patterns of FTF and S1 samples, the XRD peaks of the Si640c internal standard are indicated with the up-triangles symbols. To check if there is a difference between the lattice parameters of small and large grained $CoSb_3$, the XRD data of both samples FTF and S1 were analyzed by Rietveld refinement. Both lattice parameters are almost the same ($a = 9.0364(1)$ Å and $a = 9.0363(1)$ Å for FTF and S1, respectively) and are in good agreement with literature [72]. This indicates a weak effect if any of the grain size in our $CoSb_3$ crystal.

From the results it can be seen that we avoided any Sb-inclusion formation due to much stronger mixing of the melt produced by the hydrodynamic conditions of the inclination and rotation of the ampoule (see Section 7.2). However, spontaneous nucleation occurs due to the sudden breakdown of the supercooling. Consequently, a high number of oriented grains formed, growing polycrystalline $CoSb_3$. Therefore, in the next step we added a seed channel to the bottom of the growth ampoule. With powder in the seed channel, no nucleation is necessary, consequently no supercooling and no breakdown.

QX620: IRB with powder as a substitute for a seed

The preparation of the crystal growth experiment QX620 with starting liquid composition $Co_{0.07}Sb_{0.93}$ can be roughly summarized in two steps. First, the seed channel with 40 mm in length and 4 mm in diameter at the bottom of growth ampoule (see inset Figure 6.7(a)) was filled with stoichiometric $CoSb_3$ powder obtained in the previous experiment (i.e., from QX591). Second, the ingot obtained after the synthesis process was crushed, and pulverized and subsequently filled in the remaining volume of the growth ampoule (see Figure 6.7(a)). Figure 6.7(b) shows the ingot QX620. The extraction from the growth ampoule was done without any problem because the seed had broken off with only a very small part remaining on the body of the crystal. Similar to QX591, only approx. 25% of the total volume of the ingot is $CoSb_3$, while the rest is mainly Sb-rich eutectic fabric. This is due to the starting composition and the phase diagram (see Figure 2.5). To find the starting interface between the powder and the melt, we longitudinally cut the seed channel (see Figure 6.7(c)). We found the seed/crystal interface at 17 mm inside the seed channel. In addition, it can be seen that at the right side of the seed/crystal interface there are six grains that grew in different orientations which was confirmed by Laue-diffraction images).

However, only one of them occupies the whole diameter and covers the whole diameter at the top of the channel.

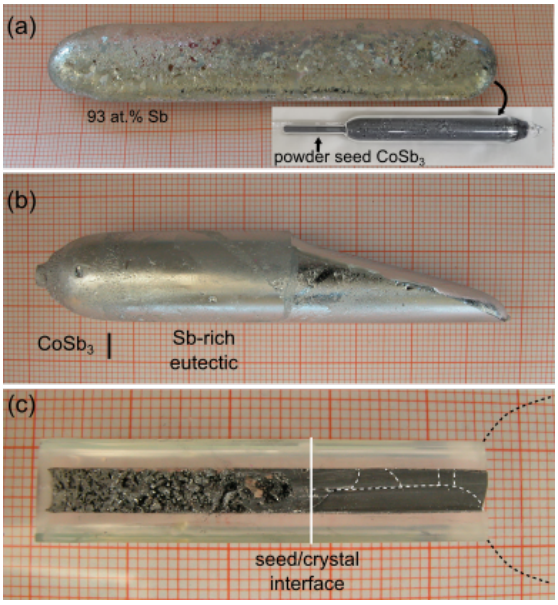

Figure 6.7: Ingot of QX620 after (a) synthesis and (b) after crystal growth by IRB method. Only approx. 25% of the total ingot consists of $CoSb_3$ the rest being the Sb-rich eutectic. (c) Seed channel axial-longitudinally cut after the crystal growth experiment.

Microstructure

From the axial cut of the ingot shown in Figure 6.8, we can see that the crystal growth of a large single grain of $CoSb_3$ was successful for the first time. The obtained crystal has a size of 15 mm in diameter and 15 mm in length. Here, the interface in the crystal (see white dashed line) is slightly concave with deflection of 1 mm. Bright grey regions on the right side of this interface are $CoSb_3$ as well. This results from the termination of the experiment which was done a bit too early before the eutectic composition of the residual melt was exactly reached.

Light microscope images of the polished surface of QX620 show that the $CoSb_3$ large single crystal is inclusion-free and crack-free (see Figure 6.9(a-b)). Very few small round-spherical voids are also to be observed near to the seed region. This is related to the evaporation of some liquid Sb-inclusions which were trapped during the crystallization process. Moreover, it can be seen that next to the interface (Figure 6.9(c))

and in the Sb-rich eutectic region (Figure 6.9(d)) there is still $CoSb_3$, which was not consumed by the grown crystal due to the early termination of the experiment.

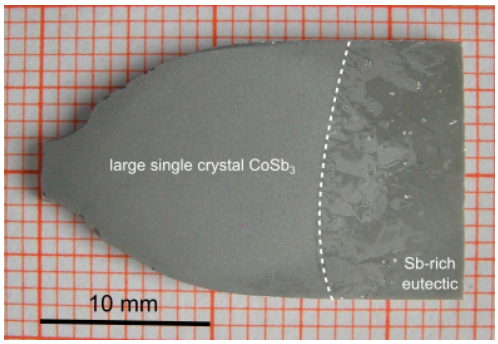

Figure 6.8: Optical micrograph of the lapped surface of the first part of QX620 grown by the Inclined Rotary Bridgman method using a polycrystalline powder seed of the same material. A large $CoSb_3$ single crystal of 15 mm in diameter and 15 mm in height has been obtained.

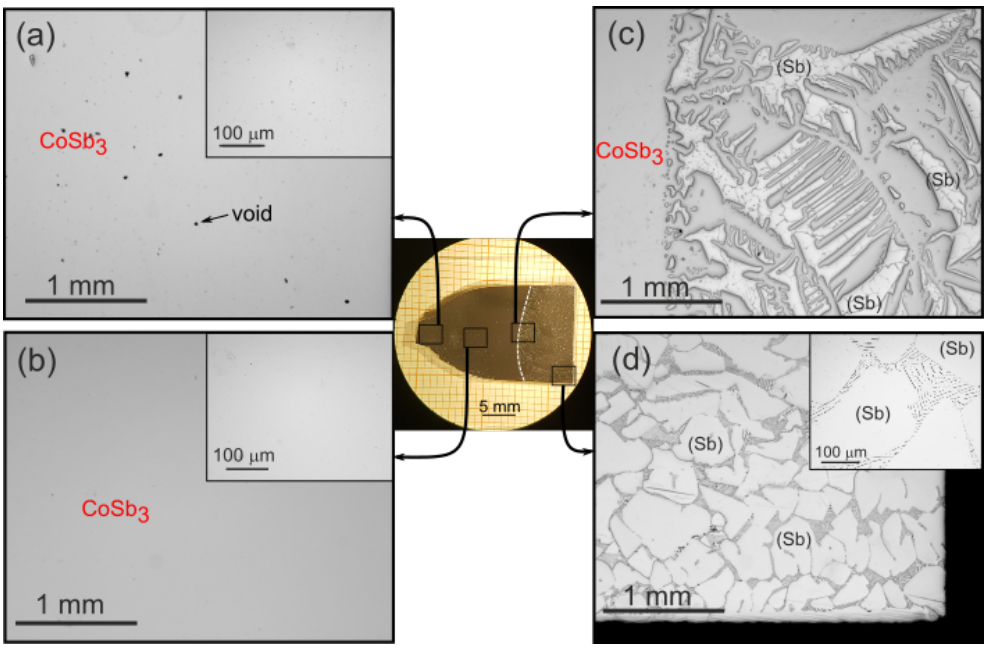

Figure 6.9: Incident light microscope images of the polished surface of QX620. (a-b) $CoSb_3$ large single crystal is inclusion-free. Above the interface line (c) and in the Sb-rich zone (d) there is still some $CoSb_3$ that was not incorporated in the grown crystal due to the early termination of the experiment.

XRD analysis and X-ray Laue diffraction

Figure 6.10 confirms the single-crystallinity of QX620 by means of X-ray Laue diffraction and X-ray powder diffraction. These measurements were carried out in the first cut of the as-grown ingot QX620 as shown schematically in Figure 6.10(a). The back-scattered Laue diffraction pattern of $CoSb_3$ obtained with the primary X-ray beam parallel to [100] direction is shown in Figure 6.10(b).

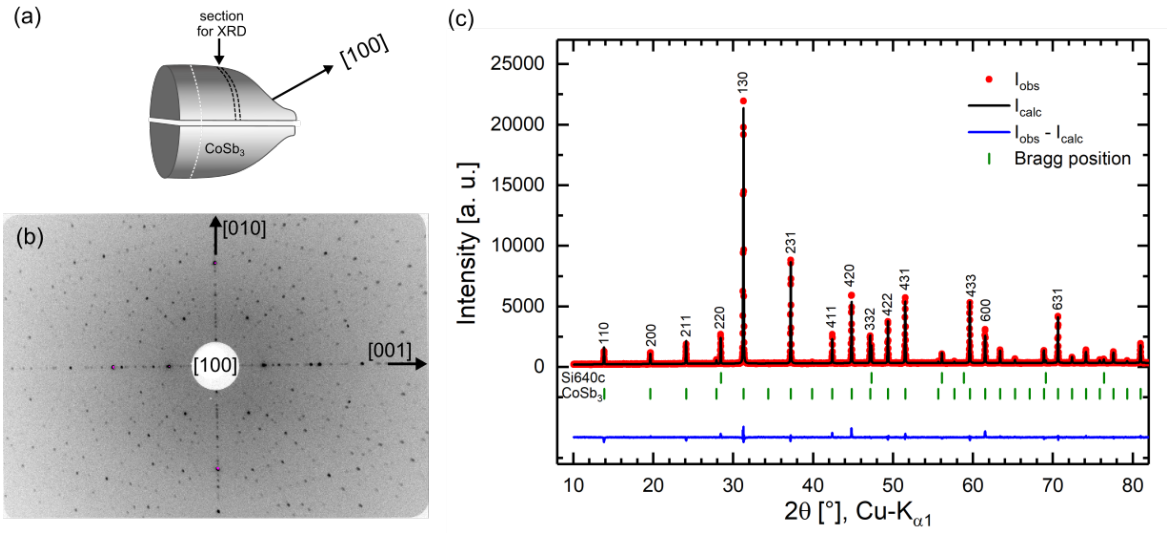

Figure 6.10: (a) Schematic orientation of QX620 indicating the [100] direction. (b) X-ray Laue back-scattering diffraction pattern of the grown $CoSb_3$ single crystal with the primary X-ray beam parallel to [100] direction. (c) Rietveld refinement of the X-ray diffraction pattern of QX620. Observed: red circles, calculated: black line, and difference: blue line at the bottom. Green thick marks indicate the *hkl* reflections for the $CoSb_3$ phase and Si640c internal standard.

The image has $2mm$ symmetry according to [100] direction of a crystal with Laue group $\frac{2}{m}\overline{3}$. By performing a Rietveld refinement on the XRD pattern, we corroborated the existence of single-phase $CoSb_3$ with no hint of a secondary phase (such as Sb). The refined parameters of the data are listed in Table 6.1. The obtained lattice parameter $a = 9.03638(5)$ Å matches with the value found for QX591 and that reported in literature [72]. With this experiment, we avoided the the spontaneous nucleation of the grown crystal, allowing for the formation of a large single grain of $CoSb_3$ selected from a few grains at the very beginning. Additionally, we determined the starting interface position for further experiments using a solid seed.

Table 6.1: Structural parameters obtained from the Rietveld refinement of X-ray diffraction pattern of QX620.

Parameters	QX620
a (Å)	9.0364(5)
Sb y	0.3337(1)
Sb z	0.1576(1)
ρ_{calc} (g/cm^3)	7.637
R_p	19.4
R_{wp}	14.2
R_e	11.95
χ^2	1.42

QX625: IRB with bulky seed

Similar to QX620, the preparation of the bulky crystal growth experiment of QX625 by the Inclined Rotary Bridgman method using a $CoSb_3$ bulky seed can be summarized in two steps. As a first step, a cuboid piece of 5 mm × 5 mm × 14 mm size was cut from QX591 (polycrystalline material). The diameter was reduced up to 3.8 mm forming a cylindrical seed shape (see Figure 6.11(a)). This was done to ensure that the seed fits into the seed channel.

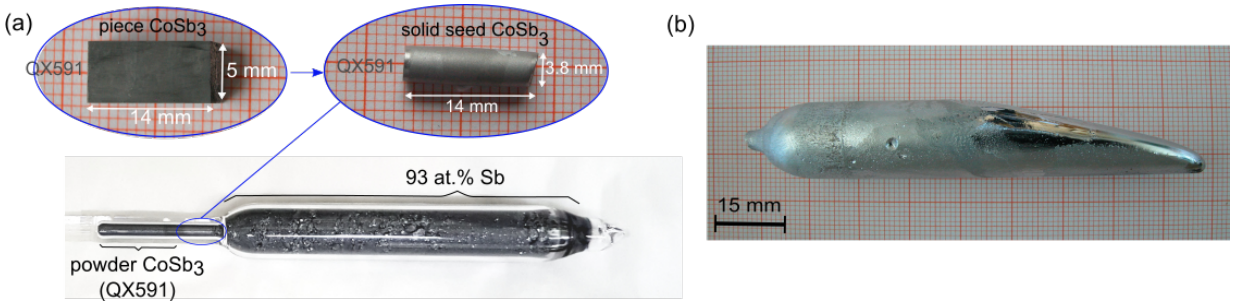

Figure 6.11: (a) Cylindrical bulky seed $CoSb_3$ prepared from a cuboid to be used for the growth of QX625 by the Inclined Rotary Bridgman method. Different grains can be distinguish in the surface of the seed. (b) As-grown ingot of QX625 obtained by Inclined Rotary Bridgman method using a solid seed.

The lower part (nearly 26 mm) of the seed channel was filled with $CoSb_3$ powder (similar to the previous experiment) then the remaining part of the channel was filled with the bulky (solid) seed. As a second step, and analogous to QX620, the remaining growth ampoule was filled with synthesized powder of QX625 with a starting composition 93 at.% Sb (see Figure 6.11(a)). Based on the seed/crystal interface position found in the previous experiment, we fixed the growth ampoule in the furnace. The first as-grown $CoSb_3$ ingot that has been grown using a solid seed is shown in Figure 6.11(b).

X-ray Laue diffraction

To verify the single-crystallinity of QX625, a perpendicular cut to the growth direction of around 20 mm from the seed was performed. Then, the cut part was fixed in the head of a goniometer for X-ray Laue measurement, see Figure 6.12(a). The obtained X-ray Laue diffraction image is shown in Figure 6.12(b). As it can be seen, the resulting diffraction image corresponds exactly to the obtained from QX620 (see Figure 6.10(b)) and matches with the simulated one (see Figure 6.12(c)).

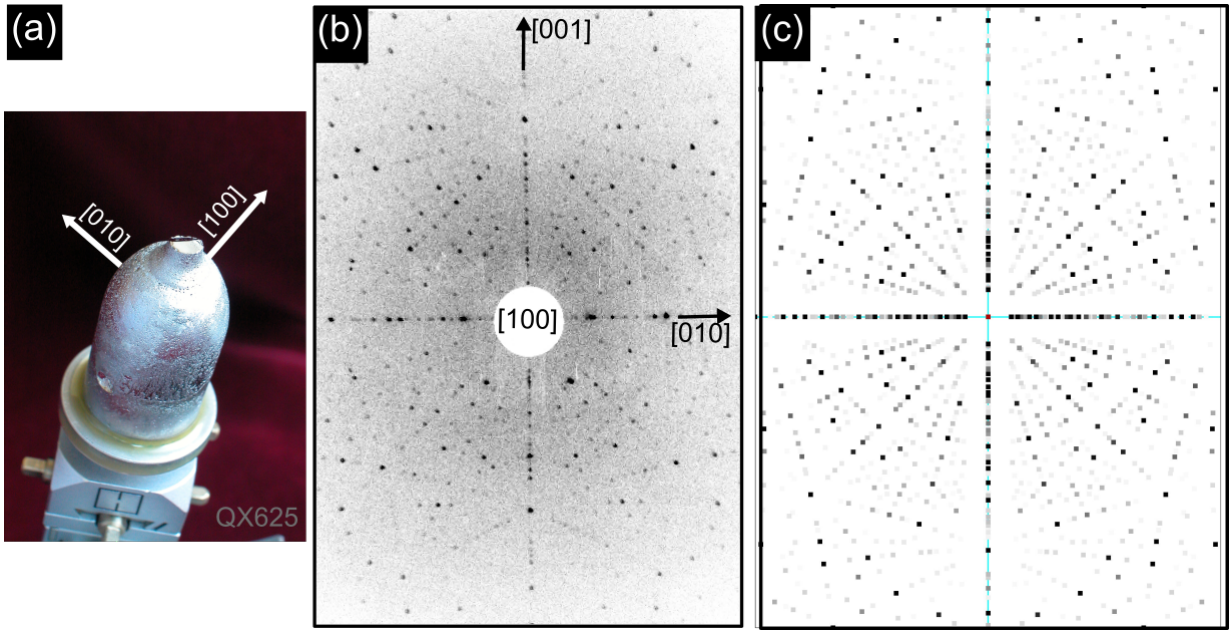

Figure 6.12: (a) As-grown ingot QX625 cut and fixed on a goniometer head for X-ray Laue diffraction. X-ray Laue back-scattering diffraction pattern (b) measured and (c) simulated for $CoSb_3$, showing the [100] orientation of the sample QX625 parallel to the primary X-ray beam.

The simulated pattern was obtained using the program package *LauePt* [107]. $CoSb_3$ single-phase status was confirmed by XRD. The calculated density $\rho_{calc} = 7.638$ g/cm^3 matches with the value $\rho_x = 7.63(4)$ g/cm^3 found experimentally using the method described in Section 4.4.3.

6.2 In-doped $CoSb_3$

It is worth to mention that in the In-doped $CoSb_3$ In should fill the cages in the (empty) skutterudite structure. Here, preliminary small-scale vertical Bridgman experiments were performed in order to find the filling fraction limit of In atoms in $CoSb_3$ crystals without forming a second phase (such as InSb). Prior to the experiments it is worth to mention two aspects: (i) From previous results, we knew that only starting compositions with $\geq$ 92.7 at.% Sb yield to a primarily crystallization of $CoSb_3$. (ii) We are aware that a third component like In might change the peritectic temperature of the binary compounds. Thus, to be sure that our growth experiments of In-doped $CoSb_3$ are within the peritectic part of the liquidus temperature, we used starting melt compositions with 94 at.% Sb to grow the ternaries compounds.

6.2.1 Vertical Bridgman experiments

The ingots with starting composition $(In_{x_0}Co_{1-x_0})_{0.06}Sb_{0.94}$ for x_0 ranging from $0.05 \leq x_0 \leq 0.2$ are shown in Figure 6.13. Unlike undoped $CoSb_3$, their surface is less shinny. The first-to-freeze part was cut, pulverized and then analyzed with X-ray powder diffraction (see Figure 6.14). From the XRD patterns, one can see that all the samples exhibit the characteristic peaks of the In-doped-$CoSb_3$ phase with only a trace amount of Sb phase (less than 2 vol.%). This was expected due to vertical Bridgman method having poor mixing conditions. No InSb phase was found even for the sample with highest indium concentration (i.e., for $x = 0.2$). A quick analysis of the lattice parameter a of In-doped $CoSb_3$ by using Rietveld refinement produced the values of a 9.0372(2) Å, 9.0373(2) Å and 9.0373(2) Å for $x_0 = 0.05$, 0.15 and 0.2, respectively. From these results, we noticed that In atoms slightly increase the lattice parameter of $CoSb_3$ by less than 1 % compared to the corresponding QX625 (undoped $CoSb_3$, $a = 9.0362(4)$ Å). Hence, crystal undoped $CoSb_3$ can be used as a seed in further experiment with Inclined Rotary Bridgman method.

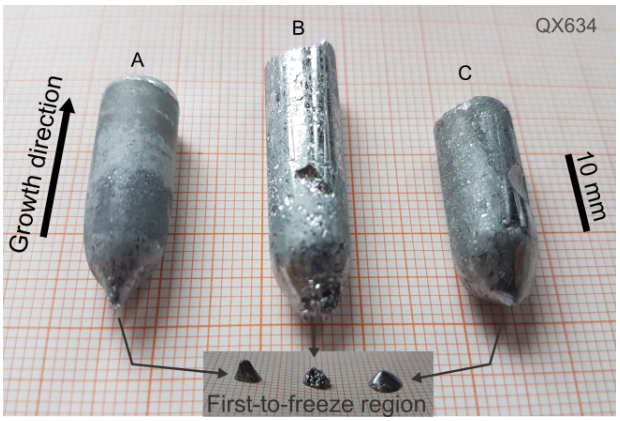

Figure 6.13: Ingots of QX634-A, B, C with different starting compositions $(In_{x_0}Co_{1-x_0})_{0.06}Sb_{0.94}$ for $x_0 = 0.05$, 0.15 and 0.2 obtained by small-scale experiments using the vertical Bridgman method. Inset shows the first-to-freeze parts cut from each ingot.

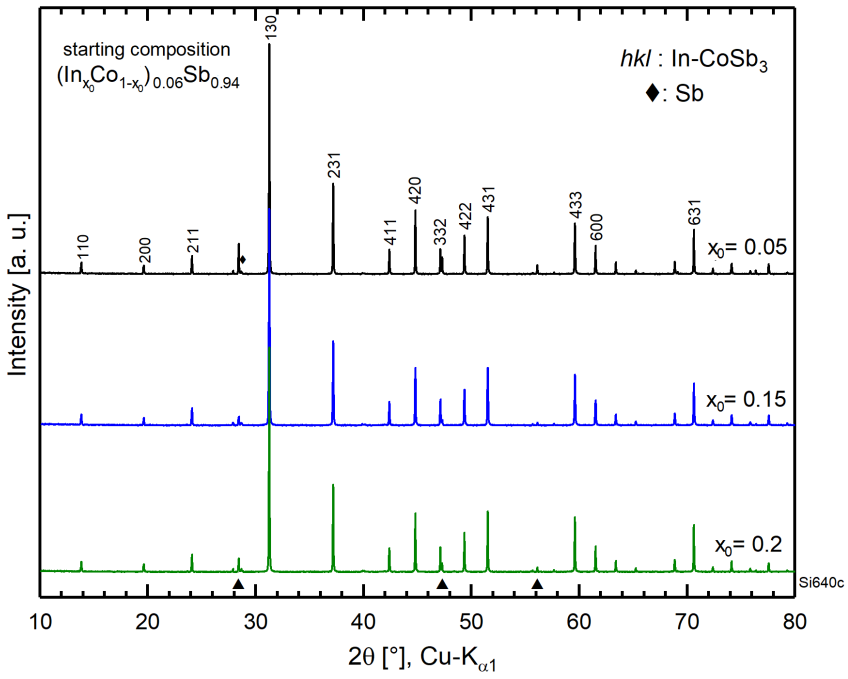

Figure 6.14: X-ray powder diffraction patterns of the three crystals QX634-A, B, C with different starting compositions $(In_{x_0}Co_{1-x_0})_{0.06}Sb_{0.94}$ for $x_0 = 0.05$, 0.15 and 0.2. A trace of Sb phase has been detected in all samples. There has been no indication of InSb formation.

6.2.2 IRB experiments with [100]-oriented seed

Based on the vertical Bridgman results, two In-doped crystals with starting composition $(In_{x_0}Co_{1-x_0})_{0.06}Sb_{0.94}$ with $x_0 = 0.05$ and 0.1 were grown by the Inclined Rotary Bridgman method. The procedure to grow the In-doped $CoSb_3$ crystals, QX637 ($x_0 = 0.05$) and QX631 ($x_0 = 0.1$), the analogous to QX625 but with an oriented seed of $CoSb_3$ ([100] parallel to the growth direction). Since the results of the previous experiment (QX625) were promising, it was possible to use the same seed for both growth experiments. Contrary to undoped $CoSb_3$, these ingots stuck to the growth ampoule and a bit of force was necessary to remove the ingot from the ampoule. This was due to the presence of a brown/green layer in both ingots which was identified as low-cristobalite (SiO_2). Most of these layers fell down easily while the rest was carefully removed with SiC water-proof grinding paper.

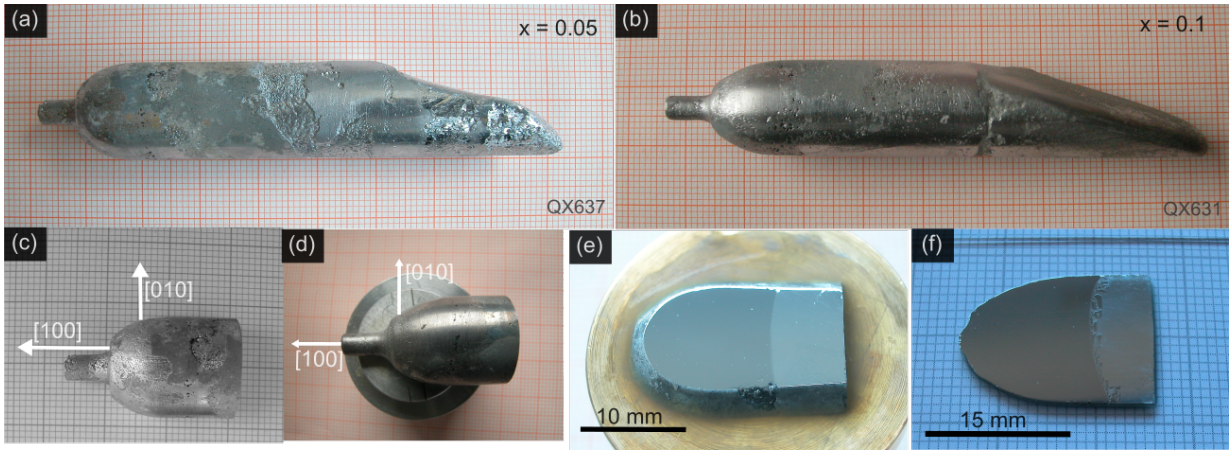

Figure 6.15: Ingots of (a) QX637 and (b) QX631. (c-d) Both crystals preserved the [100] direction of the seed. (e-f) Oriented axial polished sections parallel to [100] direction.

Figures 6.15(a) and (b) show the ingots QX637 and QX631 after removing most of the SiO_2 layer. Both ingots started to grow from approx. 7-8 mm inside the channel, because the solid seed was located only until 33 mm (including the powder at the lower part of the seed channel). Hence, the 4 mm diameter crystal shape is expected to be In-doped $CoSb_3$ material. Once again, only approx. 25% of the total ingot is In-doped $CoSb_3$ while the rest is mostly pure Sb.

X-ray Laue diffraction measurements confirmed the single-crystallinity of both crystals. Also, these results show that the single crystals are perfectly oriented along the

[100] direction of the seed, as sketched in Figures 6.15 (c) and (d). After orienting the ingots along one of the main direction, two parallel cuts to [100] direction were performed obtaining 2 mm thick slices which were subsequently polished (see Figures 6.15(e) and (f)). Both crystals have a slightly concave interface.

Microstructure studies

Figure 6.16 shows the incident light microscope images of the polished surfaces of QX637 and QX631. The uniform contrast along the longitudinal sections confirms a good homogeneity of the In-doped $CoSb_3$ single crystals. In general, the grown crystals do not present any evidence of Sb-inclusions, grain boundaries, or cracks in the main body. However, very few Sb-inclusions of $\approx$30 μm were found in the crystal edge near the interface of QX637 (see arrows in upper right part of Figure 6.16).

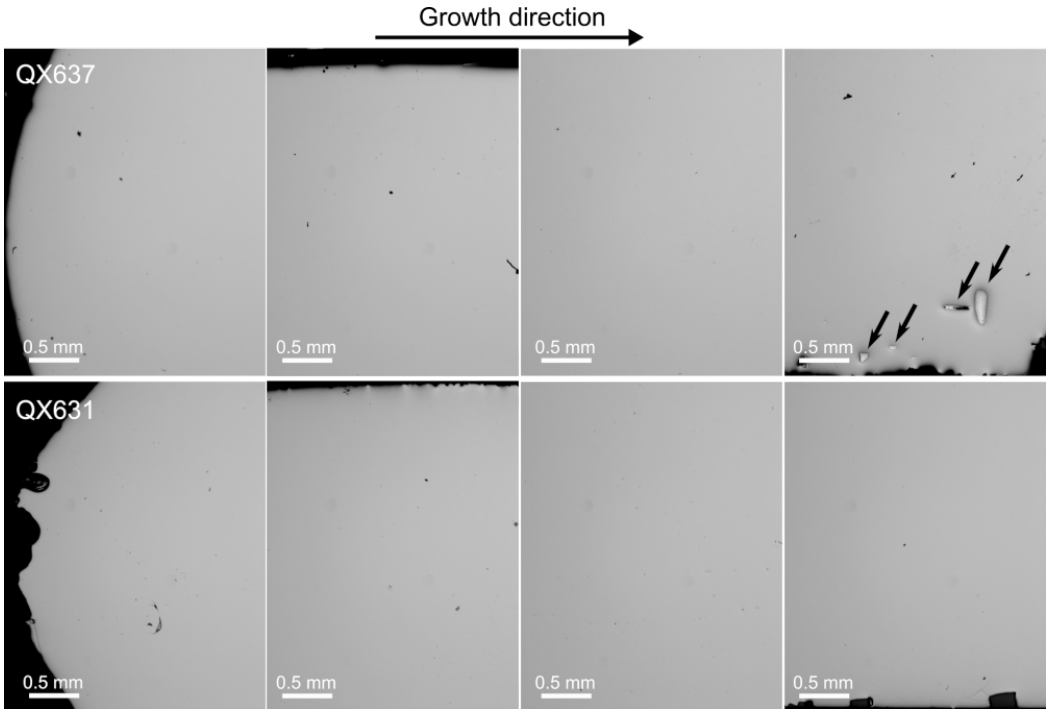

Figure 6.16: Incident light microscope images of the polished surface of QX637 (upper) and QX631 (lower). Both In-doped $CoSb_3$ crystals are mostly inclusion-free. Only few small inclusions are found at the crystal edge near to the interface in QX637.

EPMA analysis

In order to determine the In concentration in the doped $CoSb_3$ crystals, EPMA measurement was carried out on the surface of the longitudinal slice of QX631. The EPMA analysis was done along and perpendicular to the growth direction as is indicated with the white lines in the upper right left of Figure 6.17. From these results, it was impossible to detect any In in these regions (see line profiles in Figure 6.17). This indicates that the In concentration in these two crystals is below the detection limit of EPMA. Indeed, the amount of In incorporated into $CoSb_3$ structure starting from a melt of 10 at.% Co substitution by In must be much lower than expected. Regarding the Co and Sb concentrations in the grown crystal, EPMA line profiles along axial direction (line 3) and perpendicular to it (lines 1, 2 and 4) show that there is a good homogeneity in the whole crystal. This is not surprising with a compound of fixed stoichiometry.

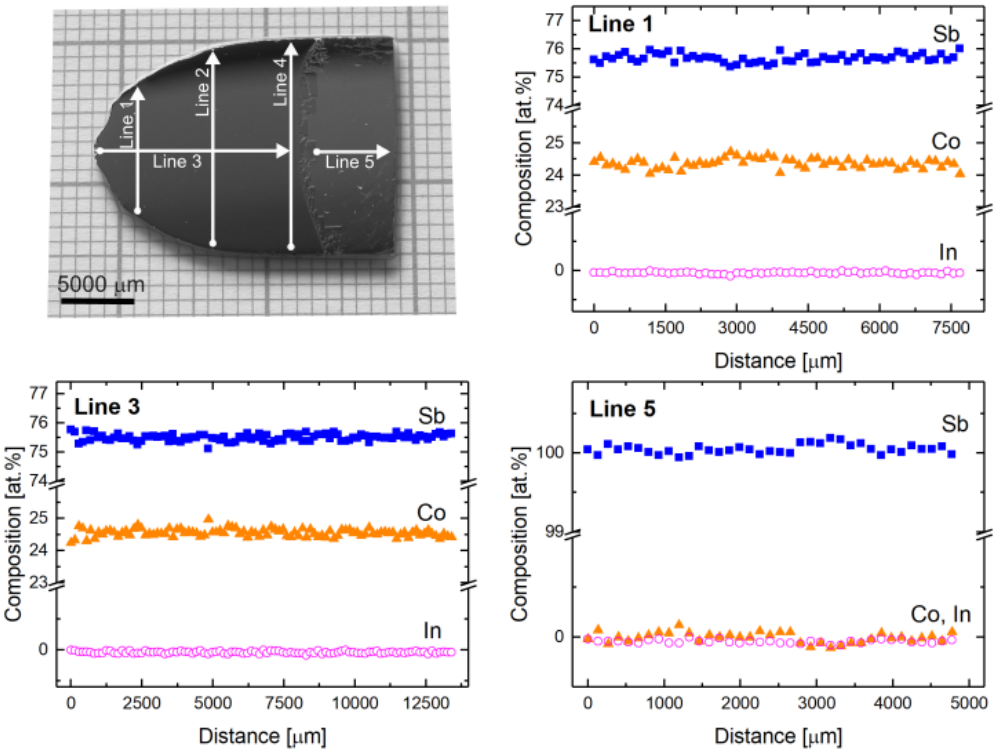

Figure 6.17: EPMA line profiles of In, Co and Sb concentrations obtained for QX631. Line profile perpendicular to the growth direction (line 1). Line profile along the crystal growth direction (line 3 in the grown crystal and line 5 in the Sb-rich eutectic zone).

XRD analysis and Rietveld refinement

Figure 6.18 shows the X-ray diffraction patterns of the In-doped $CoSb_3$ crystals with starting composition $(In_{x_0}Co_{1-x_0})_{0.06}Sb_{0.94}$ for $x_0 = 0.05$ (QX637) and $x_0 = 0.1$ (QX631). All diffraction peaks in the XRD patterns of the two single crystals were identified as In-doped $CoSb_3$ single-phase material without the presence of any secondary phases such as Sb or InSb. For comparison, we have included the XRD pattern of the undoped $CoSb_3$ ($x_0 = 0.0$, crystal QX625) in Figure 6.18. Inset shows that the peaks slightly widened after doping with In. The peaks corresponding to higher angles were also shifted due to the doping.

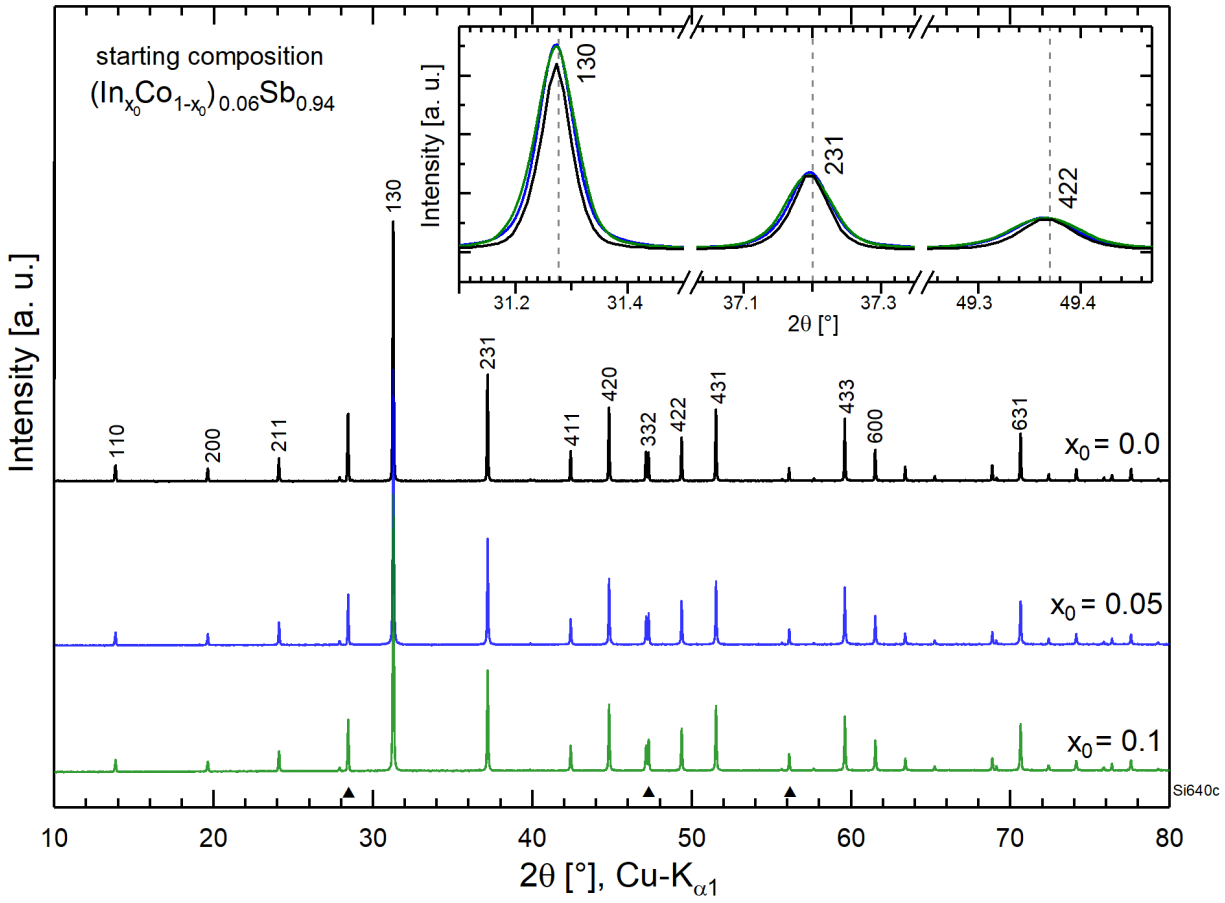

Figure 6.18: X-ray powder diffraction patterns of undoped and In-doped $CoSb_3$ with starting composition $(In_{x_0}Co_{1-x_0})_{0.06}Sb_{0.94}$ ($x_0 = 0.05$ and 0.1) obtained by the IRB method. No any secondary phase (Sb or InSb) was observed. Inset shows the widening of the peaks with In concentration.

To gain a deeper understanding of the controversy of In occupying the cages, Co or Sb sites, we proposed three different models for Rietveld refinement to analyze the distribution of In in the $CoSb_3$ crystal structure:

- Model A: In substitutes Sb at site $24g$ (0, y, z)
- Model B: In substitutes Co at site $8c$ (0.25, 0.25, 0.25)
- Model C: In partially fills the cages at site $2a$ (0, 0, 0)

Despite the failed detection of In in EPMA measurements, as a first approximation we assumed a 100 % incorporation of the In offered by the melt. The atomic occupancy of all atoms was fixed, and an overall temperature factor B_{ov} for all the atoms in each sample was applied. Table 6.2 and Figure 6.19 show the Rietveld refinement results of the three models (A, B, C) for QX631 grown from the starting composition $(In_{x_0}Co_{1-x_0})_{0.06}Sb_{0.94}$ with $x_0 = 0.1$.

Table 6.2: Refined cell parameters and statistical Rietveld factors for In-doped $CoSb_3$ with starting composition $(In_{x_0}Co_{1-x_0})_{0.06}Sb_{0.94}$ for $x_0 = 0.05$ and 0.1. Three models A, B and C where simulated to fit the XRD patterns in which In substitutes Sb, Co or void sites, respectively.

Parameters	model A In: Sb-site	model B In: Co-site	model C In: void-site
$\mathbf{x_0 = 0.05}$			
a [Å]	9.0374(2)	9.0374(2)	9.0374(2)
Sb y	0.3339(1)	0.3340(1)	0.3341(1)
Sb z	0.1573(1)	0.1572(1)	0.1572(1)
R_p	19.9	20.0	19.1
R_{wp}	15.4	15.6	14.7
R_e	11.72	11.52	11.72
χ^2	1.72	1.83	1.57
$\mathbf{x_0 = 0.1}$			
a [Å]	9.0381(2)	9.0381(2)	9.0381(2)
Sb y	0.3341(1)	0.3343(1)	0.3345(1)
Sb z	0.1568(1)	0.1568(1)	0.1570(1)
R_p	21.2	20.9	21.9
R_{wp}	15.8	15.6	15.6
R_e	12.99	12.53	12.99
χ^2	1.47	1.55	1.48

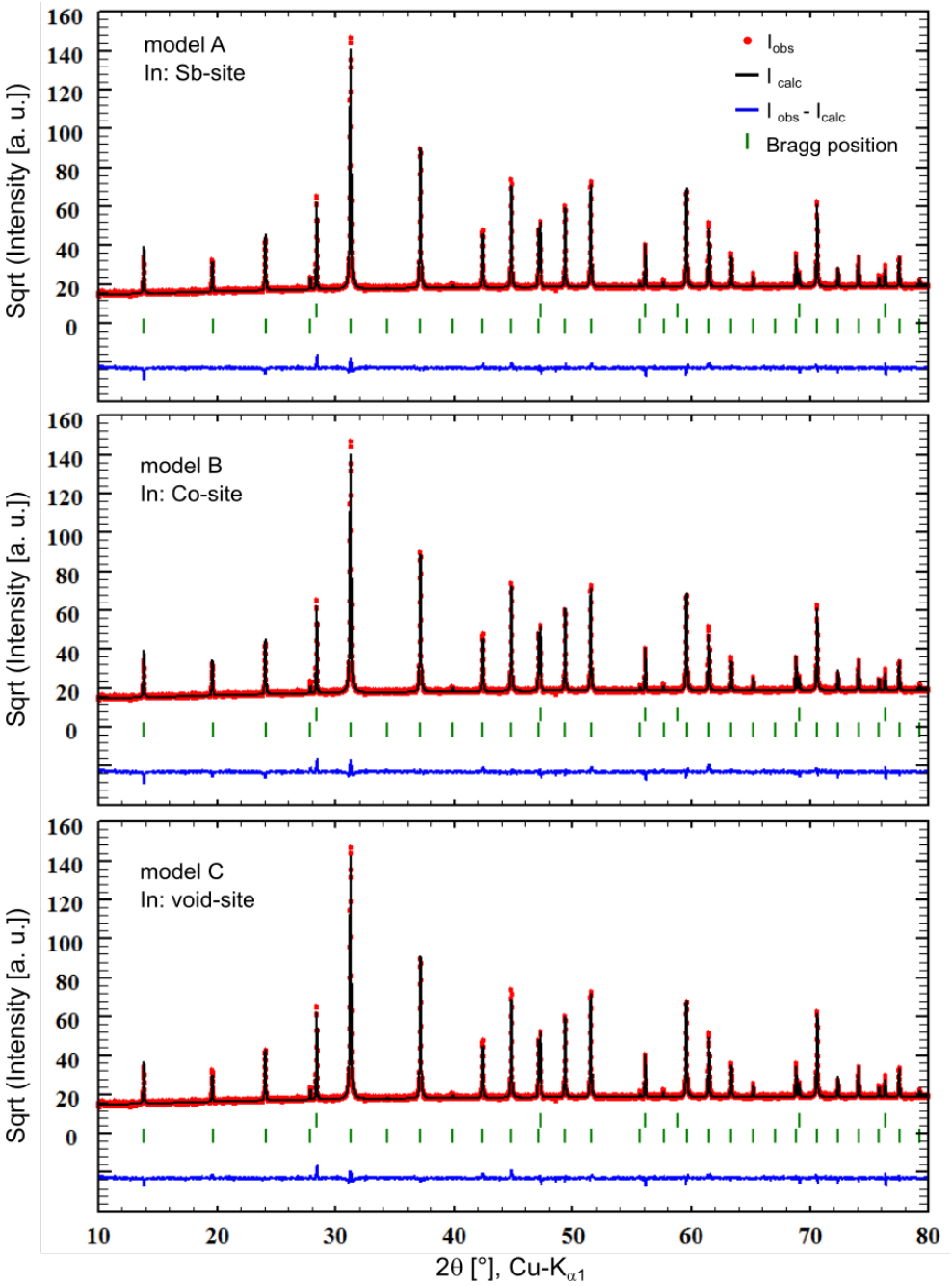

Figure 6.19: Rietveld refinement analysis of the XRD pattern of In-doped $CoSb_3$ for x_0 = 0.1 using three models. Observed: red circles, calculated: black line, and difference: blue line at the bottom. Green thick marks indicate the *hkl* reflections for the $CoSb_3$ phase and Si640c internal standard.

It can be seen that all of them fit well with the experimental data. However, the model C (In partially filling cage sites) presents the smallest value of χ^2 parameter for the two In-doped samples (see Table 6.2), producing a best fitting among all models. The low χ^2 values for models A and B suggest that In can be also incorporated in the Sb and Co sites, respectively. This might be a consequence of the low level of In concentration (much less than 0.1 at.%) in the grown crystals, which is opposite to the assumption made above.

Based on the results listed on Table 6.2, only the Sb atomic positions are slightly affected regardless of the model used for each In-doped sample. This is due to the small difference in ionic radii 0.94 Å, 0.90 Å and 0.75 Å for In, Sb and Co, respectively [108]. Figure 6.20 shows the comparison of the lattice parameters of the In-doped $CoSb_3$ crystals obtained by using VB and IRB methods, but only considering the model C. For both cases, a linear behavior of the parameter was observed after increasing the In concentration, being more pronounced for the IRB method due to the better homogeneity of the resulting crystal. These results are in agreement with the reported values in literature [47, 75, 77, 109].

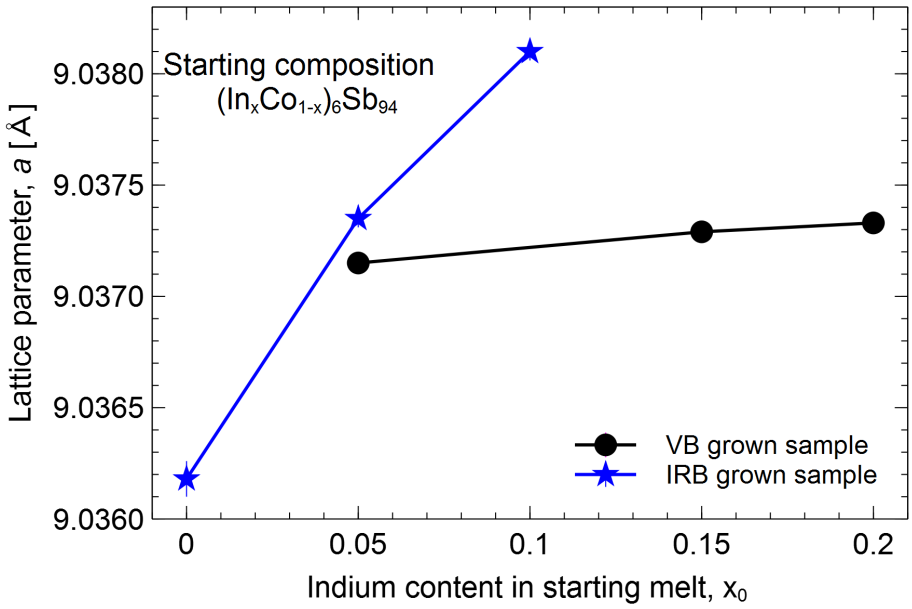

Figure 6.20: Dependence of lattice parameter on the In-doped $CoSb_3$ samples grown by Vertical Bridgman (VB) and Inclined Rotary Bridgman (IRB) method using a starting composition of $(In_{x_0}Co_{1-x_0})_{0.06}Sb_{0.94}$ for $x_0 = 0.05$, 0.1, 0.15 and 0.2. Error bars are smaller or equal than the width of the plotted symbols

6.3 Physical properties

In collaboration with the Max Planck Institute for Chemical Physics of Solids in Dresden, low-temperature electrical resistivity and Hall resistivity properties of $CoSb_3$ and In-doped $CoSb_3$ single crystals obtained by Inclined Rotary Bridgman method have been investigated. All the measurement were performed in oriented bar-shaped samples with the dimensions $4{\times}0.45{\times}1.20$ mm^3 and $1.9{\times}0.9{\times}1.0$ mm^3 (length $\times$ width $\times$ thickness). In the following, the methods and configurations used for the measurements will be briefly discussed. A very detailed information about the conditions of the measurements can be found in Ref. [110]. Here, for practical reasons, the In-doped $CoSb_3$ single crystals will be expressed as $In_xCo_4Sb_{12}$. This does not imply the In content in the solid, i.e. the mole fraction x, to be as high as x_0.

6.3.1 Equipment and conditions

Electrical resistivity and Hall measurements, were performed in a Quantum Design PPMS[1] over the temperature range of 2 - 300 K and under a magnetic field ranging up to 9 T. In order to measure the electrical resistivity ρ of the samples, a standard DC 4-probe technique was used. Electrical contacts parallel to the *ab*-plane were made using thin copper wires which were attached to the sample with silver epoxy. To measure the Hall resistivity ρ_{xy}, through the Hall voltage U_{xy}, we used the six-point method which basically consists in adding two extra contacts to the previous geometry of four-point (see sketch in Figure 6.21).

6.3.2 Electrical resistivity

The temperature dependence of the electric resistivity ρ of $CoSb_3$ and In-doped $CoSb_3$ with nominal composition $In_xCo_4Sb_{12}$ (x = 0, 0.05, 0.1) is shown in Figure 6.22. Each measurement was carried out in a sample cut from the position indicated in the sketch in Figure 6.22. Here, we observed that In doping modifies the temperature dependence of the resistivity, resulting in a non-monotonous behavior of the resistivity as a function of the In concentration. For all samples, except sample 2 (x = 0.05) which has a semiconductor behavior in the whole temperature range, the electrical resistivity

[1]PPMS: Physical Property Measurement System.

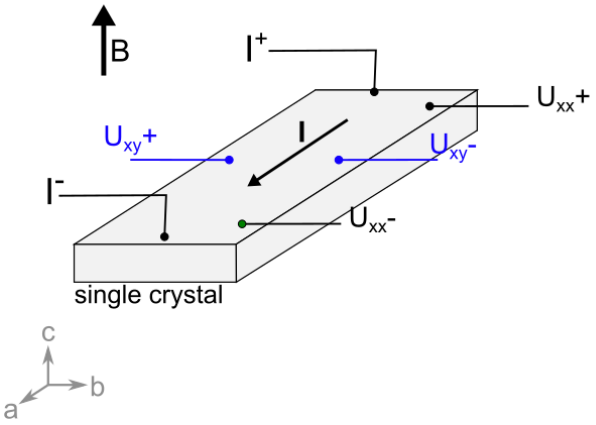

Figure 6.21: Schematic illustrations of the device setup for the measurement of the Hall resistivity ρ_{xy}. B: applied magnetic field, I: applied electric current, U_{xx} - U_{xx}: transverse voltages, and U_{xy}: Hall voltage.

decreased as the temperature is reduced, indicating a metallic-like behavior in the range 300 - 75 K. However, in the temperature range 75 - 2 K, we have found three situations: First, the slight increment of resistivity after decreasing temperature showing a semiconductor behavior. Second, the presence of a minimum of resistivity of about 1.64 mΩ-cm at 60 K for $CoSb_3$ ($x = 0$); 17.91 mΩ-cm at 73 K and 2.19 mΩ-cm at 50 K for In-doped $CoSb_3$ with $x = 0.05$, and 0.1, respectively (see insets in Figure 6.22). Finally, at 2 K the resistivity increases from the undoped $CoSb_3$ with 1.8 mΩ-cm to 25.31 mΩ-cm (sample 1) and to 2.39 mΩ-cm for $x = 0.05$ and 0.1, respectively.

The room temperature electrical resistivity for $CoSb_3$ is 4.22 mΩ-cm, which is in agreement with the values reported in Refs. [111, 112] (4 mΩ-cm); but is significantly higher than the one reported by J. Ackermann *et al.* (0.14 mΩ-cm) [113]. Moreover, we have found the resistivity increased up to 122.88 mΩ-cm and 54.78 mΩ-cm for an In concentration of $x = 0.05$ and 0.1, respectively. The increase of the resistivity of undoped $CoSb_3$ (1.8 mΩ-cm) at the lowest temperature of 2 K was also observed, reaching values of up to 25.31 mΩ-cm (sample 1) and 2.39 mΩ-cm for $x = 0.05$ and 0.1, respectively.

To study the effect of the sample position on the electrical properties, an additional measurement was performed on sample 2 corresponding to $x = 0.05$ (see sketch in the middle panel of Figure 6.22). Contrary to sample 1, the resistivity of sample 2 displays

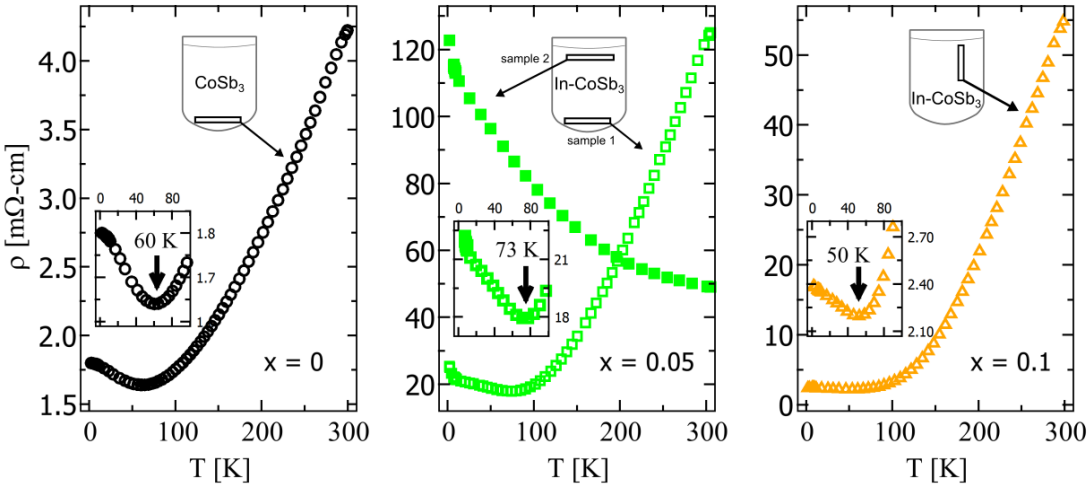

Figure 6.22: Electrical resistivity as a function of the temperature between 2 - 300 K for the single crystals $CoSb_3$ and In-doped $CoSb_3$ with nominal composition $In_xCo_4Sb_{12}$ (x =0, 0.05, 0.1). Insets show the magnification of ρ for $T \leq 100$ K of the respective panel. Sketches show the sample position in which the measurements were carried out.

a semiconductor-like behavior for the whole temperature range upon cooling down. Also, its electrical resistivity at 300 K is 49.26 mΩ-cm, which is two times lower than the value obtained for sample 1. The same electrical response has been observed for $x = 0$.

6.3.3 Hall resistivity

In Figure 6.23, the Hall resistivity ρ_{xy} is shown as a function of the magnetic field B in the range 0 - 9 T. The measurements were performed at different temperatures in the range 2 - 300 K. Very low magnetic field (0 - 0.9 T) measurements were only carried out for x = 0.1 within the temperature range 20 - 200 K (see inset Figure 6.23). Overall, one can see a linear dependence of the Hall resistivity with respect to the magnetic field, indicating the possibility of having a single type of charge carrier. Consequently, the Hall coefficient R_H ($R_H = \rho_{xy}/B$) was obtained from the slope of the linear curves fitted to ρ_{xy}(B) data. The values are presented in the bottom right panel of Figure 6.23. R_H exhibits a strong temperature dependence below 100 K and remains almost constant at higher temperatures for different In concentrations. The Hall coefficient is negative for $CoSb_3$ and x = 0.1; and positive for x = 0.05 (sample 2), suggesting that the charge carriers are electrons and

holes, respectively.

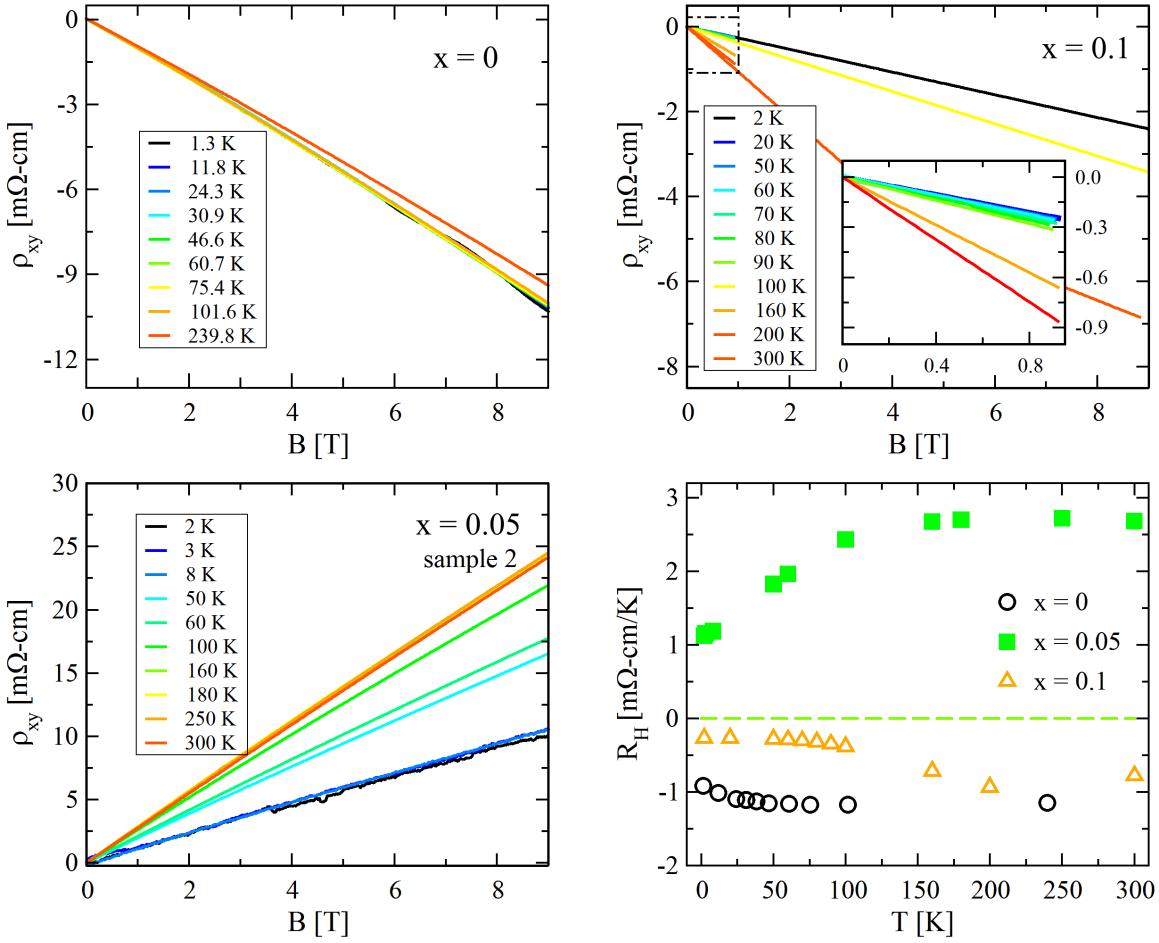

Figure 6.23: Hall resistivity ρ_{xy} measurement and Hall coefficient R_H of $In_xCo_4Sb_{12}$ for x = 0.0, 0.05, 0.1 as a function of temperature from 2 K to 300 K. Inset shows the magnification of ρ_{xy} vs. B at lower magnetic field for $x = 0.1$.

Then, the carrier density n_H was calculated from the Hall coefficient with the assumption of a single-carrier model with a scattering factor of 1. This parameter is defined as:

$$n_H = p/n = +(-)\frac{1}{R_H e}\ , \tag{6.1}$$

where p and n are the densities of holes and electrons, respectively. Meanwhile, e is the electron charge (1.60×10^{-19} C). It was found that the carrier density of the $x = 0$ sample is about an order of magnitude higher compared to $x = 0.05$ and $x = 0.1$ in the whole temperature range (Figure 6.24(a)). $CoSb_3$ ($x = 0$) shows a n-type behavior and has a

carrier density of 4.6×10^{18} cm^{-3} at room temperature, which is in agreement with those values reported in the Ref. [114]. The room temperature carrier densities of In-doped $CoSb_3$ are $2.3{\times}10^{17}$ cm^{-3} (n-type) and $\sim 3{\times}10^{17}$ cm^{-3} (p-type) for sample 1 and sample 2 of $x = 0.05$, respectively; and $\sim 8{\times}10^{17}$ cm^{-3} (n-type) for $x = 0.1$. Also, the maximum electron carrier density of In-doped $CoSb_3$ is $19.7{\times}10^{17}$ cm^{-3} at 20 K for $x = 0.1$.

Based on the Hall coefficient and the resistivity values, we determine the Hall mobility μ_H by:

$$\mu_H = \frac{R_H}{\rho} \, . \tag{6.2}$$

The results are presented in Figure 6.24(b). It can be seen that in the range 300 - 100 K, the Hall mobility increases as $T^{-3/2}$ with exception of the case $x = 0$; and below $\sim$100 K μ_H varies as $T^{3/2}$, being more pronounced for $x = 0.05$. The reduction of Hall mobility at low temperatures was also reported in others works. At room temperature the values of μ_H are between 141 - 290 cm^{2}V^{-1}s^{-1} for all the samples. The p-type sample ($x = 0.05$, sample 2) presents the highest mobility value of about 1330 cm^{2}V^{-1}s^{-1} at 130 K, which is comparable to the one obtained for $x = 0.1$ (1319 cm^{2}V^{-1}s^{-1} at 70 K). Meanwhile, n-type samples showed low mobility values such as 696 cm^{2}V^{-1}s^{-1} at 50 K and 888 cm^{2}V^{-1}s^{-1} at 60 K for $x = 0$ and $x = 0.05$, respectively.

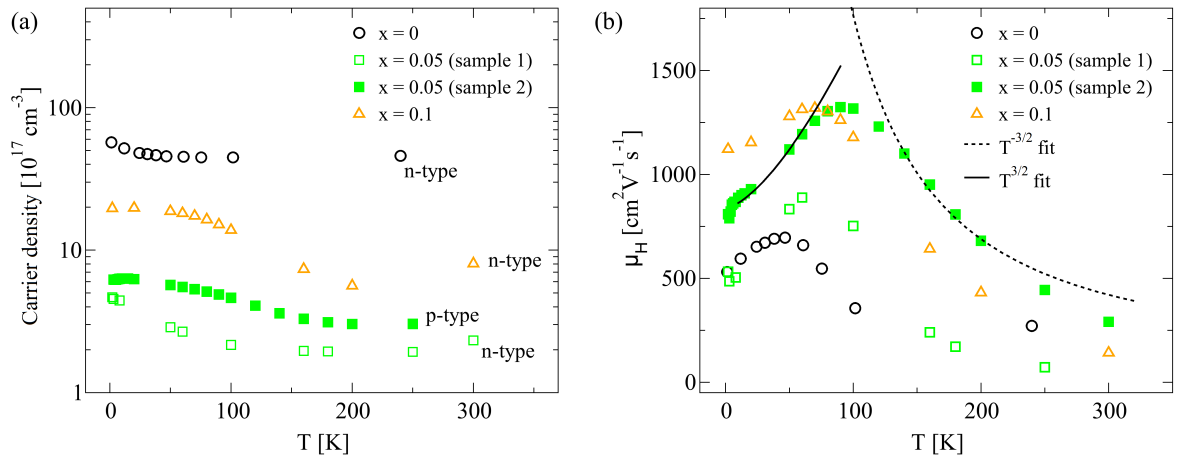

Figure 6.24: Temperature dependence of (a) the carrier concentration n_H and of (b) the Hall mobility μ_H for $CoSb_3$ and In-doped $CoSb_3$ single crystals with a nominal composition $In_xCo_4Sb_{12}$ for $x = 0$, 0.05, 0.1. Lines show the fit in the high-temperature range by $T^{-3/2}$ and by $T^{3/2}$ for temperatures below $\sim$100 K.

Chapter 7

Numerical simulation

From the results of the experiments explained in the previous sections, the effect of mixing is only observed indirectly by checking the final quality of the grown crystals. Thus, numerical simulations of hydrodynamics in crystal growth were carried out to gain a better understanding of the experiments. For comparison, the three configurations of the Bridgman method used in this work: (*i*) vertical Bridgman method, (*ii*) Inclined Bridgman method, and (*iii*) Inclined Rotary Bridgman method were simulated. All the simulation was performed by Dr. Wolfram Miller at the Leibniz Institute for Crystal Growth in Berlin, Germany, and has been included in [97].

7.1 Parameters

7.1.1 Boundary conditions

The first step to start the simulation was to compute the thermal field in the entire equipment (furnace). A sketch of the furnace geometry which is for simulation purposes embedded in a box of 1.8 m height and 1.6 m diameter with a fixed boundary temperature of 300 K is shown in Figure 7.1(a). The central part was simplified for the axisymmetric calculation by using the software CrysMAS [115] (see Figure 7.1(b)). The simulation setup was chosen in accordance with the experimental configuration. The heat conductivity and emissivity of the various materials that are part of the IRB furnace (see inset Figure 4.1) as well as from the melt are given in Table 7.1. The temperature at the boundaries of the ampoule was taken from a global axisymmetric calculation and, hence,

the values are fixed and always the same regardless of the convection. Taking into account that the experimental temperature values were obtained by a thermocouple of type K enclosed in a ceramic tube, an emissivity of 0.2 and thermal conductivity of 50 $Wm^{-1}K^{-1}$ were used in the simulations. Then, the profile temperature was calculated at different positions in the empty furnace for two different set points SP = 750 °C and SP = 900 °C for the growth of $FeSb_2$ and $CoSb_3$, respectively. For comparison, a temperature calculation was also done without considering the thermocouple.

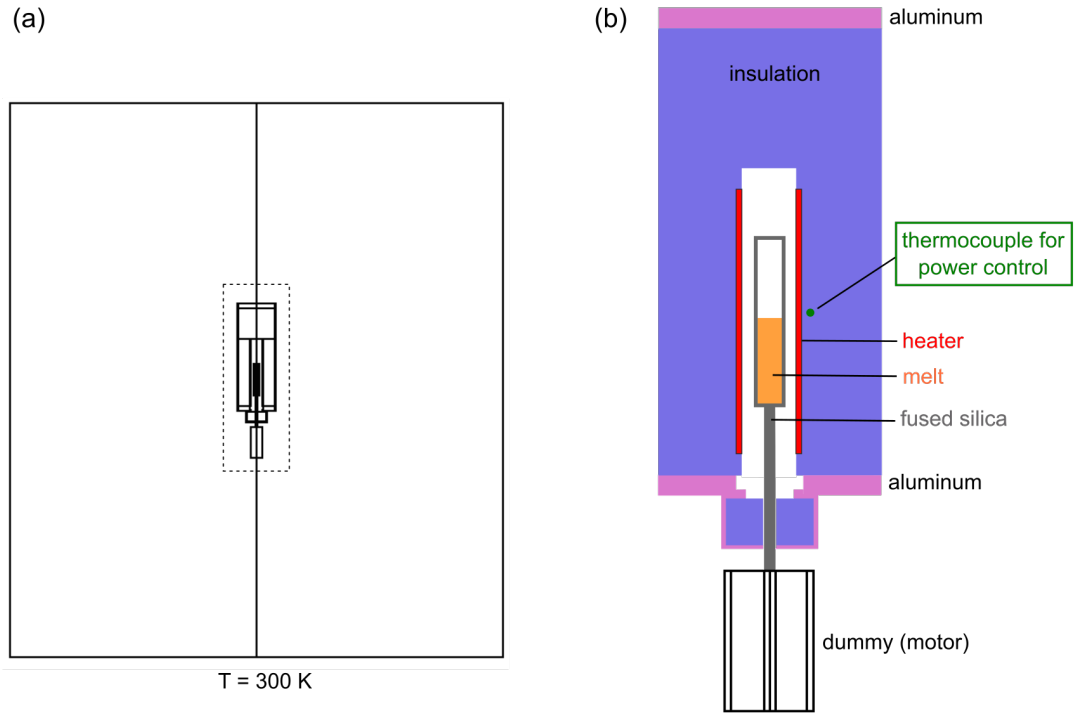

Figure 7.1: (a) Sketch of the geometry with 1.80 m in height and 1.60 m in diameter for global temperature calculations. (b) Magnification of the central part as used in the computation of the global temperature with CrysMAS.

7.1.2 Computation of melt convection

After getting the simulated temperature at the inner boundary of the ampoule along the furnace, the second step was to determine the geometry of the melt. In both configurations (vertical and inclined) the ampoule is filled up to 50 mm with Fe-Sb or Co-Sb melt. Considering the typical shape of the experimentally grown crystal in the

Table 7.1: Material properties used in the computations of the global temperature field.

Material	Heat conductivity ($Wm^{-1}K^{-1}$)	Emissivity	Ref.
Air	2.6×10^{-2}		
Aluminum	236	0.1	[116]
Al_2O_3	5.86 + 45 exp[260 (200 - T/K)]	0.35	[117]
Insulation (Fibrothal)	0.03 + 1.55 $\times$ 10^{-7} T^2/K^2	0.7	[118]
Fused silica	0.94 + 1.35 $\times$ 10 $^{-3}$ T^2/K^2	0.8	[119]
Heater	100	0.8	
Dummy	20	0.8	
Sb-melt	25	0.6	[120]

inclined furnace (and thus inclined ampoule), the resulting geometry and dimensions of the melt is as shown in Figure 7.2. Then, the three-dimensional calculation of the melt convection was performed using the software Ansys-cfx. Since both $CoSb_3$ and $FeSb_2$ single crystals are grown from starting composition mainly composed of Sb (93 at.% and 91 at.%, respectively), we used the properties for pure Sb-melt in the simulations (see Table 7.2).

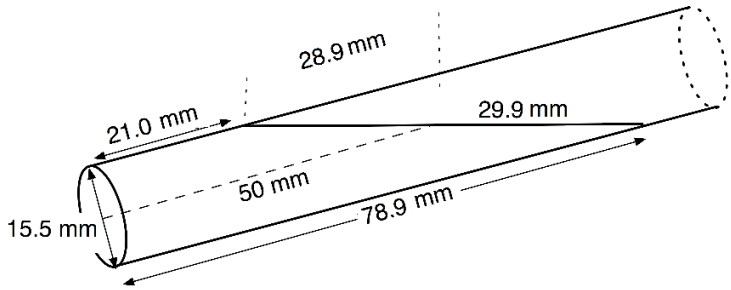

Figure 7.2: Sketch of the dimensions of the melt for the 3D calculation of convection in the case of an ampoule inclined by 15° with respect to the horizontal.

Here the hydrodynamics of the melt convection was calculated based on the Navier-Stokes equation. F. Aqra and A. Ayyad have found that the surface tension of Sb decrease linearly after increasing the temperature expressed by γ = 388 - 0.0749$(T - T_m)$ [123]. Since the temperature dependence of the surface tension of Sb is weak, we neglected Marangoni convection and we only considered the buoyancy convection. Knowing that by definition there is no buoyancy-driven convection in a vertical ampoule

Table 7.2: Physical properties of Sb-melt for convection calculation using Ansys-cfx.

Symbol	Description	Value	Reference
α	Thermal expansion coefficient	$1.03 \times 10^{-4}\,\mathrm{K}^{-1}$	Using [121]
ν	Kinematic viscosity	$1.56 \times 10^{-7}\,\mathrm{m^2 s^{-1}}$	
μ	Dynamic viscosity	$1.0 \times 10^{-3}\,\mathrm{Pa\,s}$	[121]
ρ	Density	$6400\,\mathrm{kg\,m^{-3}}$	[121]
D	Diffusion coefficient	$0.5 \times 10^{-4}\,\mathrm{cm\,s^{-1}}$	[122]
k	Thermal conductivity	$25\,\mathrm{Wm^{-1}K^{-1}}$	

with usual temperature profiles of Bridgman method but in order to compare with the inclined configuration we applied a rotation rate of 100 rpm. Regarding to the inclined furnace/ampoule, we have considered three cases:

- Case 1: Buoyancy convection only, to mimic the Inclined Bridgman experiment.
- Case 2: Buoyancy convection plus a rotation of 100 rpm, to mimic the Inclined Rotary Bridgman experiments.
- Case 3: Buoyancy convection with a modified bottom, to mimic the crystal/melt interface shape observed in the IRB experiments.

7.1.3 Computation of marker distribution

In order to visualize the mixing effect, we used a test system with a marker distribution. The marker is released at the crystal/melt interface with a constant flux of 1 mm/s (see Figure 7.3). This is considered to be a good model for the Sb-based compounds from Sb-rich solution since excess Sb is permanently rejected at the growth interface. The amount of rejected Sb is proportional to the growth and determines the flux at the bottom of modeled melt in Figure 7.3. The marker distribution is given as concentration per volume. The distribution was checked after 60 s of simulation time.

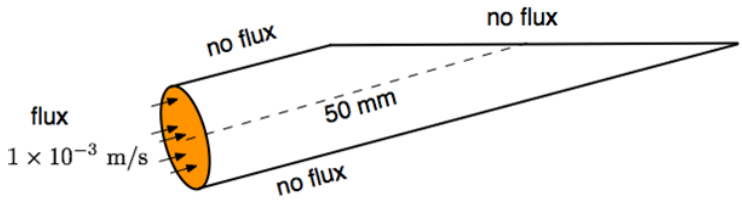

Figure 7.3: Transport of a marker released at the crystal/melt interface.

7.2 Results and Discussion

7.2.1 Comparison with temperature measurement

The results of the simulated temperature profiles for the two set points SP = 750 °C ($FeSb_2$) and SP = 900 °C ($CoSb_3$) are shown in Figure 7.4. The red triangles and blue diamonds represent the values of the experimental measurements and numerical calculations, respectively. It can be seen that they are in quite good agreement. Contrary, the temperature in the empty furnace without taking the axially arranged ceramic tube carrying the thermocouple for axial temperature measurement into account (blue lines) displays a different behavior for almost all the range of heights.

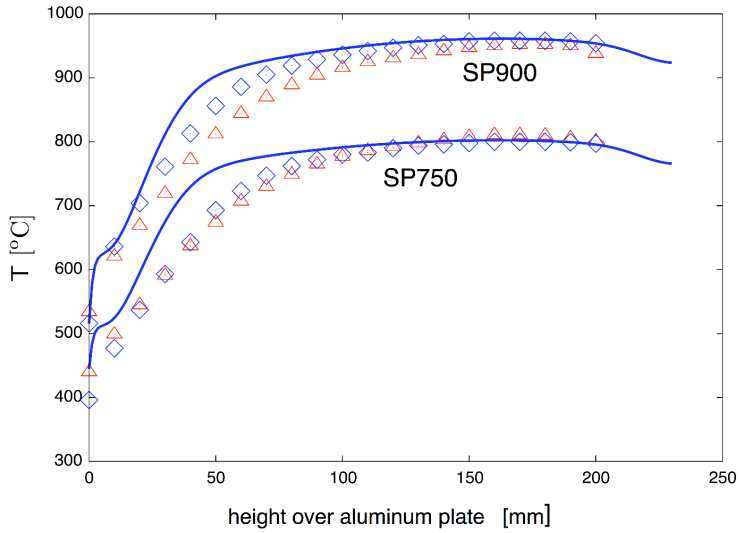

Figure 7.4: Simulation of the temperature profiles for SP = 750 °C and SP = 900 °C with Ansys-cfx. Red triangles: measurements, blue routes: calculations, blue lines: calculation without thermocouple.

Then, the control temperature was set to 900 °C and the obtained temperature at the inner boundary of the ampoule is shown with dashed lines in Figure 7.5. This temperature profile can be approximated by the following function,

$$T = 809.65\,°C + 620\frac{K}{m}z - 2600\frac{K}{m^2}z^2 \tag{7.1}$$

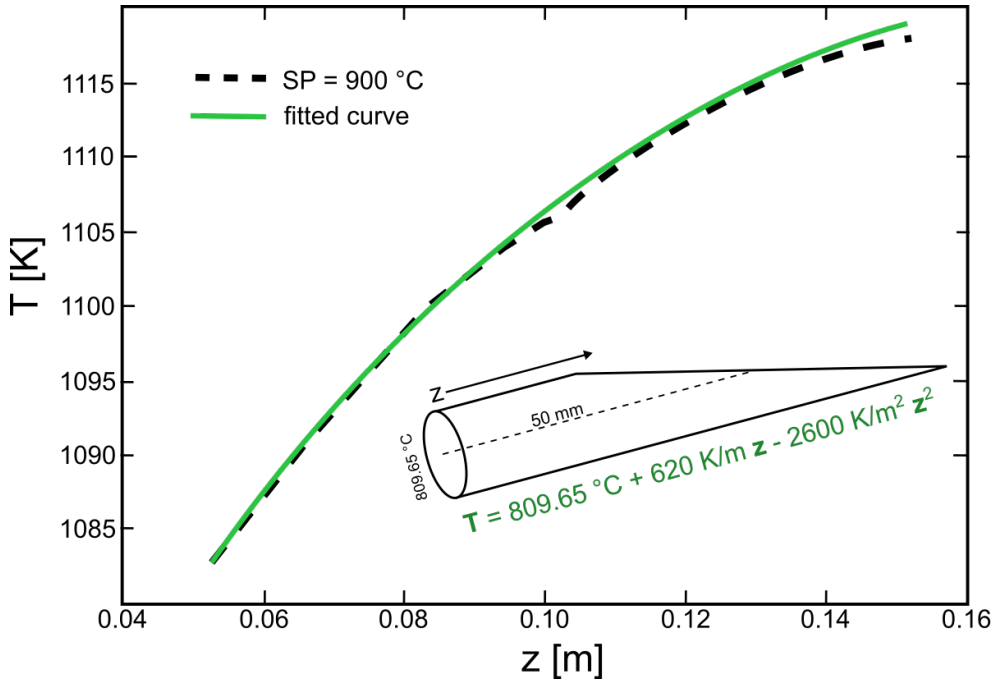

Figure 7.5: Temperature profile at the inner wall of ampoule and curve of analytic equation to mimic the temperature. Inset shows the boundary conditions for the melt.

where z is the distance from the bottom of the melt. Using the profile generated for this equation as the thermal boundary condition, we performed three-dimensional calculations for the melt.

7.2.2 Melt convection

In the calculation of melt convection, we focused more on the inclined arrangement. But a fast calculation showed that applying a rotation of 100 rpm in the vertical arrangement very weak convection rolls are obtained. In case of the inclined furnace/ampoule (see Figure 7.6 (a)), convection rolls as indicated by arrows are formed already by buoyancy forces. These rolls are quite stable in time and the flow direction change very smoothly

but the mixing was not sufficient. The influence of the crystal/melt shape has effect only near/at the interface as it can be seen in Figure 7.6(b), where the convection rolls change a little with respect to the former case. However, the picture is completely changed by applying in IRB a rotation of 100 rpm (see Figure 7.6(c)) where several small convection rolls are created, which are not stable in time. Hence, flow direction is locally changing and provides a good mixing that is also notorious in the vicinity of the bottom (interface).

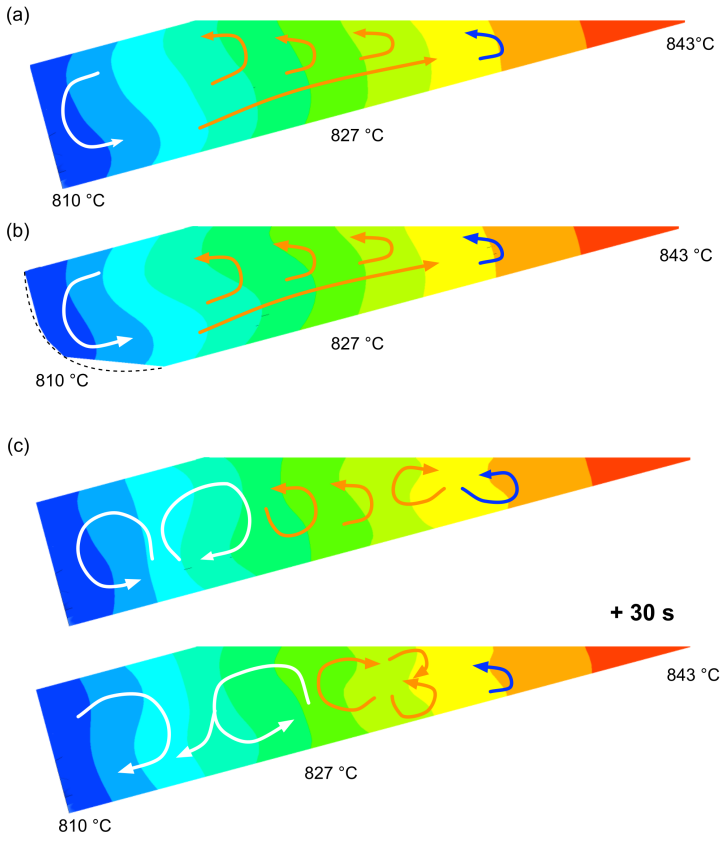

Figure 7.6: Temperature field and velocity distribution for three different cases. (a) Inclined ampoule with only buoyancy convection. (b) Inclined ampoule with a modified bottom to mimic the crystal/melt. (c) IRB with buoyancy convection plus a rotation of 100 rpm. The color code reflects the temperature value, with red representing the maximum temperature and blue representing the minimum temperature.

7.2.3 Distribution of the marker

Since modifying the bottom of the melt did not influence significantly the melt convection, this case is not considered for further calculations. Figure 7.7 shows the results for the marker distribution in the three configurations: vertical, inclined, and inclined rotary arrangement. In the case of a vertical ampoule with rotation (Figure 7.7(a)) we have a stable convection roll going down in the center and upwards at the rim with small flow velocity (2 mm/s in the close vicinity of the bottom). As a result, mixing is very weak which produced a very high marker concentration near the interface. Whereas, for an inclined ampoule without rotation (Figure 7.7(b)) the situation is much better but still there are regions of high concentration near the interface. Finally, for the case of an inclined ampoule with rotation (Figure 7.7(c)) the change of the convection roll structure in time leads to an efficient mixing with low peak concentrations in the melt.

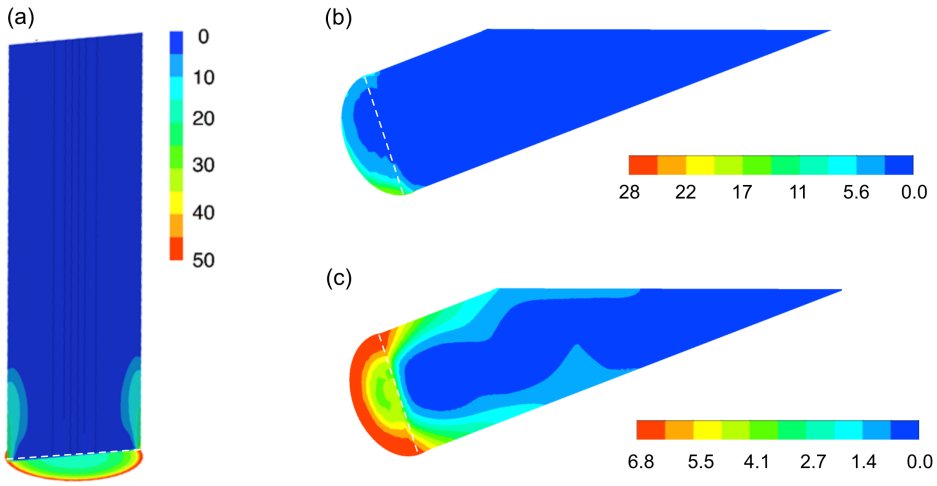

Figure 7.7: Distribution of a marker in the melt after 60 s for three different configurations. (a) vertical arrangement with rotation. (b) inclined arrangement with buoyancy flow only. (c) inclined arrangement with rotation. Lower marker concentration gradients indicate effective mixing of the melt. Note the different marker concentration scale bars in the three cases pictured.

In brief, numerical calculations showed that inclination of the ampoule already sets up an advective mixing but only additional rotation provides the sufficient mixing. This was also concluded from the experiments when observing significantly less inclusions in the case

of an inclined ampoule without rotation. And consequently, by adding rotation inclusions could be partially (for the case of $FeSb_2$) and completely (for the case of $CoSb_3$) avoided in the final crystal.

Chapter 8

Summary and outlook

8.1 Summary

In the present thesis, the Inclined Rotary Bridgman (IRB) method has been used to grow single crystals of $FeSb_2$ and $CoSb_3$ from Sb-rich solutions and some ternaries based on these compounds. It could be shown, that this method is very efficient to obtain high-quality single crystals, especially with respect of reducing or avoiding completely the Sb-inclusion formation. Here, the improvement of the crystal quality was performed in several steps which gave us a deeper understanding of the growth process using the IRB method.

Firstly, prior to explain the results obtained with the IRB method, is necessary to mention that preliminary small-scale vertical Bridgman experiments of $CoSb_3$ with starting compositions $Co_{1-x_0}Sb_{x_0}$ ($0.915 \leq x_0 \leq 0.950$) were performed. This part was a prerequisite for the successful $CoSb_3$ growth. XRD analysis of the first-to-freeze phases showed that only crystals with higher or equal concentration than 92.7 at.% Sb in the melt yield to the primary crystallization of $CoSb_3$ alone. Based on previous results, and to ensure that no $CoSb_2$ phase is formed, further growth experiments of $CoSb_3$ will be carried out with 93 at.% Sb starting composition.

Secondly, considering the IRB method, we observed that the inclined arrangement of the furnace-ampoule system (15° with respect to the horizontal direction) and an additional ampoule rotation (100 rpm along its axis) provided a strong mixing of the melt due to the gravitational forces. As a consequence, a much better mass transport was achieved in the Sb-based compounds reducing the inclusion formation at the crystal-solution interface due to the constitutional supercooling. Experiments using spontaneous nucleation resulted

in a sudden crystallization of a huge number of small grains. Further improvement was achieved by incorporating a seed channel to the bottom of the ampoule leading finally to the growth of large single crystals. Indeed, Sb-inclusions have been completely avoided in $CoSb_3$ compounds by using the IRB method in combination with native seeding. For $FeSb_2$ compounds, the density and size of these inclusions have been strongly reduced, but there is still a small residual. The dimensions of both single crystals were of approximately 15 mm in diameter and 15 mm in length.

The experimental results were accompanied by three-dimensional calculations of the melt convection employing the commercial software package ANSYS-cfx. Thus, a remarkable amplification of the melt flow was found under the Inclined Rotary Bridgman conditions compared to the conventional vertical Bridgman method. In the case of a tilted ampoule alone (i.e., without rotation of the ampoule), the convection rolls changed very smoothly and were quite stable in time but the mixing was not sufficient. However, several small convection rolls were formed by applying an ampoule rotation of 100 rpm in the IRB method. This induced a local change of the flow direction in the melt producing a better mixing. The modeling of the marker distribution, which simulates the amount of Sb rejected at the growth interface, has also shown that a much lower concentration gradient in the melt is achieved which reduces the risk of constitutional supercooling. Hence, numerical calculations showed that inclination of the ampoule already sets up better mixing but only additional rotation provides the sufficient mixing of the melt.

Thirdly, we focused on the growth of ternary compounds, $(Fe, Co)Sb_2$ and In-doped $CoSb_3$. Here, several crystals of the solid solution $Fe_{1-x}Co_xSb_2$ with $0.1 \leq x \leq 0.5$ were grown by the small-scale vertical Bridgman method in order to find the optimal solid solution prior to the IRB experiments. XRD and EPMA analyses of the first-to-freeze parts of all these $Fe_{1-x}Co_xSb_2$ crystals revealed a single-phase status of the solid solution $(Fe, Co)Sb_2$ for $0.1 \leq x \leq 0.3$ and the decomposition into two phases for $x = 0.5$, which were identified as the solid solutions $(Fe, Co)Sb_2$ and $(Fe, Co)Sb_3$. Structural changes were also observed after increasing the doping concentration: (i) the c-parameter increases slightly but the a- and b-parameters decrease strongly, resulting in an overall decrease of the unit cell volume of $(Fe, Co)Sb_2$, and (ii) a structural transformation of $Fe_{1-x}Co_xSb_2$ from orthorhombic $Pnnm$ to the pseudo-marcasite monoclinic $P2_1/c$ structure of $CoSb_2$ at $x = 0.5$. Based on the results found with the vertical Bridgman experiments, a solid solution $(Fe, Co)Sb_2$ with starting composition $(Fe_{0.9}Co_{0.1})_{0.10}Sb_{0.90}$ was successfully grown by the

Inclined Rotary Bridgman method with a native seed of $FeSb_2$. EPMA measurement on the longitudinal cut through the crystal showed that the cobalt content decreases while the Fe content increases along the growth direction. Additionally, the EPMA measurement of the first-to-freeze composition of the grown crystal was $Fe_{0.83}Co_{0.17}Sb_2$ which is in close agreement with the cobalt content incorporated in the melt.

As 92.7 at.% Sb was found to be the limit for the primary crystallization of binary $CoSb_3$, an even slightly higher Sb content was chosen for the In-doped $CoSb_3$ experiments. We used starting compositions of 94 at.% Sb, since a third component like In might change the peritectic temperature of the binary compounds. Hence, inclusion-free In-doped $CoSb_3$ large single crystals have been grown from starting compositions $(In_{x_0}Co_{1-x_0})_{0.06}Sb_{0.94}$ (x_0 = 0.05, 0.1) by using the Inclined Rotary Bridgman method in combination with native seeds of $CoSb_3$. Single crystals of size of 15 mm in diameter and 15 mm in length were obtained. XRD analysis of the first-to-freeze part of the single crystal $CoSb_3$ revealed a skutterudite structure with lattice parameter of a = 9.0362(4) Å. Moreover, the incorporation of In atoms in the crystal structure of $CoSb_3$ increased the lattice parameter. No secondary phases (such as Sb and InSb) were found in the In-doped $CoSb_3$ single crystals. However, the In content was impossible to detect with EPMA measurement on the longitudinal cut through the In-doped $CoSb_3$ crystals. This indicated that the In concentration in these two crystals were below the detection limit of EPMA.

Finally, electrical properties measurements were carried out only in single crystals of $CoSb_3$ and In-doped $CoSb_3$ compounds. The electrical resistivity of a sample cut near to the first-to-freeze part of both crystals showed a metallic-like behavior in the temperature range of 300 - 75 K and a semiconducting behavior in the range of 75 - 2 K. The value of electrical resistivity for $CoSb_3$ was 4 mΩ-cm at room temperature. Whereas, for the $In_xCo_4Sb_{12}$ single crystals, the room temperature resistivity increased up to approx. 123 mΩ-cm and 55 mΩ-cm for In concentration of x = 0.05 and 0.1, respectively. Based on the Hall measurements and the assumption of a single-carrier model, it was found that the $CoSb_3$ single crystal is electron-doped (n-type) with charge carrier density of around 4.6 × 10^{18} cm^{-3}. In the same way, the In-doped $CoSb_3$ single crystals are n-type materials with carrier densities of 2.3×10^{17} cm^{-3} for x = 0.5 and 8×10^{17} cm^{-3} for x = 0.1. However, a second measurement in a sample cut near to the interface of the single crystal $In_xCo_4Sb_{12}$ for x = 0.5 showed a p-type behavior with a charge carrier density of $\sim3\times10^{17}$ cm^{-3}.

Knowing that In generates excess of electrons, one possible explanation for this gradient from n- to p-type is that less In can be found near to the interface.

8.2 Outlook

The results shown in this work have demonstrated the effectiveness of the Inclined Rotary Bridgman method for the growth of binary Sb-based single crystals which were later on used to obtain ternary compounds through doping. The advantage of this IRB method is not only restricted to Sb-based compounds but it opens up a reliable route for other materials as well if the mass transport in solution growth is a critical issue. In this sense, our results about electrical properties characterization of $CoSb_3$ single crystal showed very interesting effects that are unique due to the quality of the material. However, measurements of Seebeck coefficient and thermal conductivity are still pending to adequately describe the thermoelectric performance of our grown materials. Notice that, to have a better understanding of the new behaviors of the physical properties, measurements must be performed on several samples taken from different positions of the grown crystals. Other physical properties besides the need to find ZT may also be of interest to measure, specially, for investigations related to doping concentration influence.

The growth process can be also improved if the synthesis is carried out by using an ampoule with lower diameter than the growth ampoule (i.e., lower than 15 mm). Thus, the ingot can be directly transferred to the growth ampoule producing a single crystal with higher quality. From the growth results by using the IRB method it was not possible to grow a yield more than 25% due to the phase diagram. Thus, in a possible following experiment, in order to increase the yield, and consequently to increase the grown crystal size, it will be an issue.

Appendix A

Supplementary figures for $(Fe, Co)Sb_2$

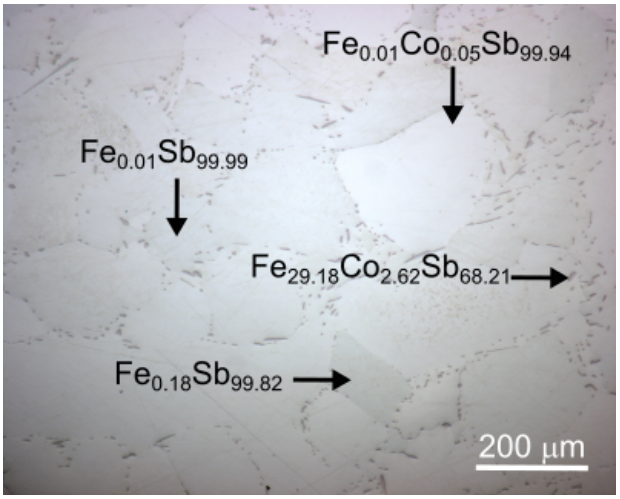

Figure A.1: Light microscope image of the Sb-rich eutectic region for $(Fe, Co)Sb_2$ showing the composition in atomic percentage at.% of the different shades areas.

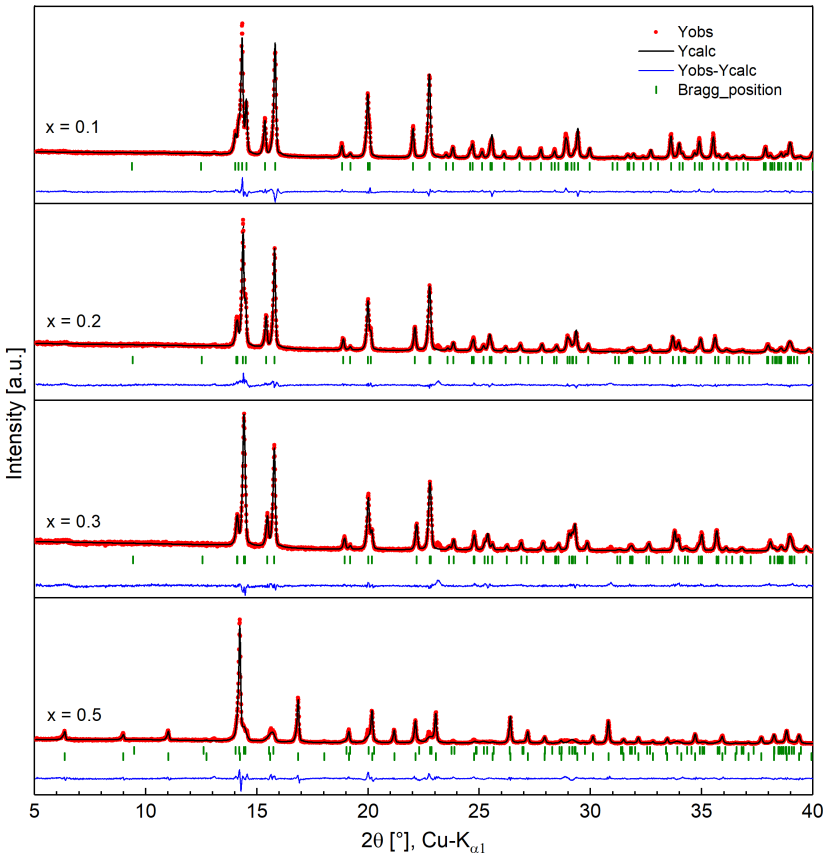

Figure A.2: Rietveld refinement of the XRD pattern the crystal $(Fe_{1-x}Co_x)Sb_2$. Observed-red circles, calculated-black line, and difference-blue line at the bottom. Green thick marks indicate the *hkl* reflections for the solid solutions $(Fe, Co)Sb_2$ and $(Fe, Co)Sb_3$.

List of Figures

List of Tables

Bibliography

[1] L. Lave, M. Savitz, R. Berry, M. Brown, L. Cohen, M. Craford, P. Decotis, J. Degraffenreidt, H. Geller, and D. Goldstein, *Real prospects for energy efficiency in the United States* (The National Academies Press, Washington D. C, 2009).

[2] A. S. Rattner and S. Garimella, *Energy harvesting, reuse and upgrade to reduce primary energy usage in the USA*, Energy **36**, 6172 (2011).

[3] S. Chu and A. Majumdar, *Opportunities and challenges for a sustainable energy future*, Nature **488**, 294 (2012).

[4] S. W. Lee, Y. Yang, H.-W. Lee, H. Ghasemi, D. Kraemer, G. Chen, and Y. Cui, *An electrochemical system for efficiently harvesting low-grade heat energy*, Nat. Commun. **5**, 3942 (2014).

[5] R. Kishore and S. Priya, *A review on low-grade thermal energy harvesting: materials, methods and devices*, Materials **11**, 1433 (2018).

[6] A. F. Ioffe, L. S. Stilbans, E. K. Iordanishvili, T. S. Stavitskaya, A. Gelbtuch, and G. Vineyard, *Semiconductor thermoelements and thermoelectric cooling*, Phys. Today **12**, 42 (1959).

[7] D. Rowe, *CRC Handbook of thermoelectrics* (CRC Press, Boca Raton, 1995).

[8] H. J. Goldsmid, *Introduction to thermoelectricity* (Springer Berlin Heidelberg, New York, 2010).

[9] J. Yang and T. Caillat, *Thermoelectric materials for space and automotive power generation*, MRS Bulletin **31**, 224 (2006).

[10] L. E. Bell, *Cooling, heating, generating power, and recovering waste heat with thermoelectric systems*, Science **321**, 1457 (2008).

[11] P. Aranguren, M. Araiz, D. Astrain, and A. Martínez, *Thermoelectric generators for waste heat harvesting: A computational and experimental approach*, Energ. Convers. Manage. **148**, 680 (2017).

[12] G. Snyder, *Small thermoelectric generators*, J. Electrochem. Soc. **17**, 54 (2008).

[13] J. R. Sootsman, D. Y. Chung, and M. G. Kanatzidis, *New and old concepts in thermoelectric materials*, Angew. Chem. Int. Ed. **48**, 8616 (2009).

[14] A. Ioffe, *Physics of semiconductors* (Academic Press, New York, 1960).

[15] T. M. Tritt, *Thermal Conductivity: Theory, properties, and applications* (Springer, New York, 2004).

[16] Y. He, P. Lu, X. Shi, F. Xu, T. Zhang, G. J. Snyder, C. Uher, and L. Chen, *Ultrahigh thermoelectric performance in mosaic crystals*, Adv. Mater. **27**, 3639 (2015).

[17] T. M. Tritt, *Recent trends in thermoelectric materials research I* (Academic Press, San Diego, 2001).

[18] *Thermoelectrics handbook: macro to nano*, edited by D. Rowe (CRC Press, Boca Raton, 2006).

[19] T. M. Tritt and M. A. Subramanian, *Thermoelectric materials, phenomena, and applications: A bird's eye view*, MRS Bulletin **31**, 188 (2006).

[20] P. Sun, N. Oeschler, S. Johnsen, B. B. Iversen, and F. Steglich, *Narrow band gap and enhanced thermoelectricity in* $FeSb_2$, Dalton Trans. **39**, 1012 (2010).

[21] W. Schnelle, A. Leithe-Jasper, H. Rosner, R. Cardoso-Gil, R. Gumeniuk, D. Trots, J. A. Mydosh, and Y. Grin, *Magnetic, thermal, and electronic properties of iron-antimony filled skutterudites* MCo_4Sb_{12} *(M=Na, K, Ca, Sr, Ba, La, Yb)*, Phys. Rev. B **77**, 094421 (2008).

[22] M. Rull-Bravo, A. Moure, J. F. Fernández, and M. Martín-González, *Skutterudites as thermoelectric materials: revisited*, RSC Adv. **5**, 41653 (2015).

[23] A. Bentien, S. Johnsen, G. K. H. Madsen, B. B. Iversen, and F. Steglich, *Colossal Seebeck coefficient in strongly correlated semiconductor $FeSb_2$*, Europhys. Lett. **80**, 17008 (2007).

[24] Q. Jie, R. Hu, E. Bozin, A. Llobet, I. Zaliznyak, C. Petrovic, and Q. Li, *Electronic thermoelectric power factor and metal-insulator transition in $FeSb_2$*, Phys. Rev. B **86**, 115121 (2012).

[25] P. Sun, N. Oeschler, S. Johnsen, B. B. Iversen, and F. Steglich, *Thermoelectric properties of the narrow-gap semiconductors $FeSb_2$ and $RuSb_2$: a comparative study*, J. Phys. Conf. Ser. **150**, 012049 (2009).

[26] R. Hu, V. F. Mitrović, and C. Petrovic, *Anisotropy in the magnetic and transport properties of $Fe_{1-x}Co_xSb_2$*, Phys. Rev. B **74**, 195130 (2006).

[27] R. Hu, V. F. Mitrović, and C. Petrovic, *Anisotropy in the magnetic and electrical transport properties of $Fe_{1-x}Cr_xSb_2$*, Phys. Rev. B **76**, 115105 (2007).

[28] J. Warren and C. Petrovic, *Enhancement of the thermoelectric properties in doped $FeSb_2$ bulk crystals*, J. Appl. Phys. **112**, 013703 (2012).

[29] A. Bentien, G. K. H. Madsen, S. Johnsen, and B. B. Iversen, *Experimental and theoretical investigations of strongly correlated $FeSb_{2-x}Sn_x$*, Phys. Rev. B **74**, 205105 (2006).

[30] A. V. Sanchela, A. D. Thakur, and C. Tomy, *Enhancement in thermoelectric properties of $FeSb_2$ by Sb site deficiency*, J. Materiomics **1**, 205 (2015).

[31] H. Luo, J. W. Krizan, L. Muechler, N. Haldolaarachchige, T. Klimczuk, W. Xie, M. K. Fuccillo, C. Felser, and R. J. Cava, *A large family of filled skutterudites stabilized by electron count*, Nat. Commun. **6**, 6489 (2015).

[32] L. D. Chen, T. Kawahara, X. F. Tang, T. Goto, T. Hirai, J. S. Dyck, W. Chen, and C. Uher, *Anomalous barium filling fraction and n-type thermoelectric performance of $Ba_yCo_4Sb_{12}$*, J. Appl. Phys. **90**, 1864 (2001).

[33] L. Guo, X. Xu, J. R. Salvador, and G. P. Meisner, *Coupled vibrational modes in multiple-filled skutterudites and the effects on lattice thermal conductivity reduction*, Appl. Phys. Lett. **102**, 111905 (2013).

[34] M. Puyet, B. Lenoir, A. Dauscher, P. Weisbecker, and S. Clarke, *Synthesis and crystal structure of $Ca_xCo_4Sb_{12}$ skutterudites*, J. Appl. Phys. **177**, 2138 (2004).

[35] G. S. Nolas, M. Kaeser, R. T. Littleton, and T. M. Tritt, *High figure of merit in partially filled ytterbium skutterudite materials*, Appl. Phys. Lett. **77**, 1855 (2000).

[36] B. C. Sales, D. Mandrus, and R. K. Williams, *Filled skutterudite antimonides: a new class of thermoelectric materials*, Science **272**, 1325 (1996).

[37] H. Kim, M. Kaviany, J. C. Thomas, A. V. der Ven, C. Uher, and B. Huang, *Structural order-disorder transitions and phonon conductivity of partially filled skutterudites*, Phys. Rev. Lett. **105**, 265901 (2010).

[38] X. Shi, S. Bai, L. Xi, J. Yang, W. Zhang, L. Chen, and J. Yang, *Realization of high thermoelectric performance in n-type partially filled skutterudites*, J. Mater. Res. **26**, 1745 (2011).

[39] Y. Kawaharada, K. Kurosaki, M. Uno, and S. Yamanaka, *Thermoelectric properties of $CoSb_3$*, J. Alloys Compd. **315**, 193 (2001).

[40] R. Zybała, M. Schmidt, P. Kamińska, M. J. Kruszewski, J. Grzonka, K. Pietrzak, and Ł. Ciupiński, *Skutterudite ($CoSb_3$) thermoelectric nanomaterials fabricated by pulse plasma in liquid*, Mater. Today: Proceedings **5**, 10316 (2018).

[41] S. L. Tonquesse, É. Alleno, V. Demange, V. Dorcet, L. Joanny, C. Prestipino, O. Rouleau, and M. Pasturel, *Innovative synthesis of mesostructured $CoSb_3$-based skutterudites by magnesioreduction*, J. Alloys Compd. **796**, 176 (2019).

[42] J. Zhang, B. Xu, F. Yu, D. Yu, Z. Liu, J. He, and Y. Tian, *Thermoelectric properties of n-type $CoSb_3$ fabricated with high pressure sintering*, J. Alloys Compd. **503**, 490 (2010).

[43] C.-H. Park and Y.-S. Kim, *Ab initio study of native point-defects in $CoSb_3$: understanding off-stoichiometric doping properties*, Phys. Rev. B **81**, 085206 (2010).

[44] T. Caillat, J.-P. Fleurial, and A. Borshchevsky, *Bridgman-solution crystal growth and characterization of the skutterudite compounds $CoSb_3$ and $RhSb_3$*, J. Cryst. Growth **166**, 722 (1996).

[45] D. T. Morelli, T. Caillat, J.-P. Fleurial, A. Borshchevsky, J. Vandersande, B. Chen, and C. Uher, *Low-temperature transport properties of p-type $CoSb_3$*, Phys. Rev. B **51**, 9622 (1995).

[46] L. Xi, Y. Qiu, S. Zheng, X. Shi, J. Yang, L. Chen, D. J. Singh, J. Yang, and W. Zhang, *Complex doping of group 13 elements In and Ga in caged skutterudite $CoSb_3$*, Acta Mater. **85**, 112 (2015).

[47] T. He, J. Chen, H. D. Rosenfeld, and M. A. Subramanian, *Thermoelectric properties of Indium-filled skutterudites*, Chem. Mater. **18**, 759 (2006).

[48] H. Okamoto, *Co-Sb (Cobalt-Antimony)*, J. Phase Equil. **12**, 244 (1991).

[49] K. W. Richter and H. Ipser, *Reinvestigation of the binary Fe-Sb phase diagram*, J. Alloys Compd. **247**, 247 (1997).

[50] P. C. Canfield and Z. Fisk, *Growth of single crystals from metallic fluxes*, Philos. Mag B **65**, 1117 (1992).

[51] D. Mandrus, A. Migliori, T. W. Darling, M. F. Hundley, E. J. Peterson, and J. D. Thompson, *Electronic transport in lightly doped $CoSb_3$*, Phys. Rev. B **52**, 4926 (1995).

[52] T. Souma and M. Ohtaki, in *Proceedings of the 25th International Conference on Thermoelectrics* (IEEE, Vienna, Austria, 2006), pp. 598–602.

[53] Y. Cao, S. Yuan, M. Liu, B. Kang, B. Lu, J. Zhang, and S. Cao, *High quality $FeSb_2$ single crystal growth by the gradient freeze technique*, J. Cryst. Growth **363**, 128 (2013).

[54] T. Caillat, A. Borshchevsky, and J.-P. Fleurial, *Properties of single crystalline semiconducting $CoSb_3$*, J. Appl. Phys **80**, 4442 (1996).

[55] M. Kowasch, MSc thesis, Ludwig-Maximilians-Universität München, Department of Earth and Environmental Sciences, Crystallography Section, 2018.

[56] M. Akasaka, T. Iida, G. Sakuragi, S. Furuyama, M. Noda, S. Matsui, M. Ota, H. Suzuki, H. Sato, Y. Takanashi, and S. Sakuragi, *Effects of post-annealing on thermoelectric properties of p-type $CoSb_3$ grown by the vertical Bridgman method*, J. Alloys Compd. **386**, 228 (2005).

[57] H. Okamoto, *Phase diagrams of binary iron alloys* (ASM International, Materials Park, Ohio, 1993).

[58] B. Pei, B. Björkman, B. Sundman, and B. Jansson, *A thermodynamic assessment of the iron-antimony system*, Calphad **19**, 1 (1995).

[59] R. Hultgen, P. Desai, D. Hawkoins, M. Gleise, and K. Kelley, *Selected values of thermodynamic properties of the elements* (ASM, Metals Park, Ohio, 1973).

[60] J. Czochralski, *Ein neues Verfahren zur Messung des Kristallisationsgeschwindigkeit der Metalle*, Z. Phys. Chem. **92**, 219 (1918).

[61] C. S. Barrett, P. Cucka, and K. Haefner, *The crystal structure of antimony at 4.2, 78 and 298° K*, Acta Cryst. **16**, 451 (1963).

[62] H. Holseth, A. Kjekshus, S. E. Harnung, H. Lundström, G. Borch, and J. C. Craig, *Compounds with the marcasite type crystal structure: IV. The crystal structure of* $FeSb_2$, Acta Chem. Scand. **23**, 3043 (1969).

[63] K. Momma and F. Izumi, *VESTA: A three-dimensional visualization system for electronic and structural analysis*, J. Appl. Cryst. **41**, 653 (2008).

[64] Y. Zhang, C. Li, Z. Du, C. Guo, J. Li, and M. Liu, *Supplementary measurements of the primary crystalline phases of the Co-Ni-Sb and the Co-Fe-Sb ternary systems*, J. Alloys Compd. **509**, 4944 (2011).

[65] C. Li, D. Zhu, Y. Zhang, Z. Du, C. Guo, J. Li, and J.-C. Tedenac, *Thermodynamic assessment of the Co-Fe-Sb system*, Calphad **47**, 23 (2014).

[66] I. Ohnuma, H. Enoki, O. Ikeda, R. Kainuma, H. Ohtani, B. Sundman, and K. Ishida, *Phase equilibria in the Fe-Co binary system*, Acta Mater. **50**, 379 (2002).

[67] K. Ishida and T. Nishizawa, *The Co-Sb (Cobalt-Antimony) system*, Bull. Alloy Phase Diagrams **11**, 243 (1990).

[68] G. Hanninger, H. Ipser, P. Terzieff, and K. L. Komarek, *The Co-Sb phase diagram and some properties of NiAs-type* $Co_{1\pm x}Sb$, J Less Common Met. **166**, 103 (1990).

[69] A. Kjekshus, T. Rakke, A. F. Andresen, and J. O. Thomas, *Compounds with the marcasite type crystal structure: XII. Structural data for arsenides and antimonides*, Acta Chem. Scand. **31a**, 253 (1977).

[70] T. Chen, J. C. Mikkelsen, and G. B. Charlan, *Crystal growth and crystal chemistry of NiAs-type compounds: MnSb, CoSb, and NiSb*, J. Cryst. Growth. **43**, 5 (1978).

[71] A. Kjekshus, B. Nolander, P. Klæboe, S. J. Cyvin, I. Lagerlund, and L. Ehrenberg, *On the properties of binary compounds with the $CoSb_2$ type crystal structure*, Acta Chem. Scand. **25**, 411 (1971).

[72] T. Schmidt, G. Kliche, and H. D. Lutz, *Structure refinement of skutterudite-type cobalt triantimonide, $CoSb_3$*, Acta Cryst. C **43**, 1678 (1987).

[73] K. Akai, H. Kurisu, T. Moriyama, S. Yamamoto, and M. Massuura, in *Proceedings of 17th International Conference on Thermoelectrics* (IEEE, Nagoya, Japan, 1998), p. 105.

[74] Y. Du, K. F. Cai, S. Chen, Z. Qin, and S. Z. Shen, *Investigation on Indium-filled skutterudite materials prepared by combining hydrothermal synthesis and hot pressing*, J. Electron. Mater. **40**, 1215 (2011).

[75] R. C. Mallik, *Thermoelectric properties of $In_zCo_4Sb_{12}$ skutterudites*, Met. Mater. Int. **14**, 223 (2008).

[76] R. C. Mallik, C. Stiewe, G. Karpinski, R. Hassdorf, and E. Müller, *Thermoelectric properties of Co_4Sb_{12} skutterudite materials with partial in filling and excess in additions*, J. Electron. Mater. **38**, 1337 (2009).

[77] Y. Tang, Y. Qiu, L. Xi, X. Shi, W. Zhang, L. Chen, S. Tseng, S. Chen, and G. J. Snyder, *Phase diagram of InCoSb system and thermoelectric properties of In-containing skutterudites*, Energy Environ. Sci. **7**, 812 (2014).

[78] G. Li, K. Kurosaki, Y. Ohishi, H. Muta, and S. Yamanaka, *Thermoelectric properties of group 13 elements-triple filled skutterudites: nominal*, Mater. Trans. **55**, 1232 (2014).

[79] A. Grytsiv, P. Rogl, H. Michor, E. Bauer, and G. Giester, *$In_yCo_4Sb_{12}$ Skutterudite: phase equilibria and crystal structure*, J. Electron. Mater. **42**, 2940 (2013).

[80] S. Tseng, S. Chen, J. Chang, Y. Tang, and G. J. Snyder, *Co-In-Sb ternary system (I): isothermal sections and liquidus projection*, Metall. Mater. Trans E **2**, 236 (2015).

[81] M. Volmer and A. Weber, *Keimbildung in übersättigten Gebilden*, Z. Phys. Chem. **119U**, 277 (1926).

[82] K.-W. Benz and W. Neumann, *Introduction to crystal growth and characterization* (Wiley-VCH Verlag GmbH & Co. KGaA, Weinheim, 2014).

[83] T. Nishinaga, *Handbook of Crystal Growth* (Elsevier, Amsterdam, 2015).

[84] H. Scheel, *Accelerated crucible rotation: a novel stirring technique in high-temperature solution growth*, J. Cryst. Growth **13-14**, 560 (1972).

[85] W. Kossel, *Zur Theorie des Kristallwachstums*, Nachr. Ges. Wiss. Göttingen **135**, 135 (1927).

[86] I. Stranski, *Theorie des Kristallwachstums*, Z. Phys. Chem. **136**, 259 (1928).

[87] K. A. Jackson, *Liquid Metals and Solidification* (ASM, Cleveland, Ohio, 1958), p. 1741.

[88] H. M. Volmer, *Die Kinetik der Phasenbildung* (Steinkopff, Dresden, 1939).

[89] W. K. Burton, N. Cabrera, and F. C. Frank, *The growth of crystals and the equilibrium structure of their surfaces*, Philos. Trans. Royal Soc. A **243**, 299 (1951).

[90] J. A. Burton, R. C. Prim, and W. P. Slichter, *The distribution of solute in crystals grown from the melt. Part I. theoretical*, J. Chem. Phys **21**, 1987 (1953).

[91] J. A. Burton, E. D. Kolb, W. P. Slichter, and J. D. Struthers, *Distribution of solute in crystals grown from the melt. Part II. experimental*, J. Chem. Phys. **21**, 1991 (1953).

[92] L. O. Wilson, *On interpreting a quantity in the burton, prim and slichter equation as a diffusion boundary layer thickness*, J. Cryst. Growth **44**, 247 (1978).

[93] G. H. Gulliver, *Metallic alloys: their structure and constitution* (Griffin & Comp., London, 1908).

[94] E. Scheil, *Bemerkungen zur Schichtkristallbildung*, Z. Metallkd. **34**, 70 (1942).

[95] W. Tiller, K. Jackson, J. Rutter, and B. Chalmers, *The redistribution of solute atoms during the solidification of metals*, Acta Mater. **1**, 428 (1953).

[96] M. E. Glicksman, *Principles of Solidification* (Springer, New York, 2011).

[97] M. Pillaca, O. Harder, W. Miller, and P. Gille, *Forced convection by inclined rotary Bridgman method for growth of $CoSb_3$ and $FeSb_2$ single crystals from Sb-rich solutions*, J. Cryst. Growth **475**, 346 (2017).

[98] A. Kirgintsev and E. Avvakumov, *A method of stirring the melt in controlled crystallization*, Sov. Phys. Crystallogr. **10**, 375 (1965).

[99] M. Kumagawa, T. Ozawa, and Y. Hayakawa, *A new technique for the growth of III-V mixed crystal layers*, Appl. Surface Sci. **33-34**, 611 (1988).

[100] T. Ozawa, Y. Hayakawa, and M. Kumagawa, *Growth of III-V ternary and quaternary mixed crystals by the rotationary Bridgman method*, J. Crystal Growth. **109**, 212 (1991).

[101] P. Gille, M. Presia, R. Bloedner, and N. Puhlmann, *Horizontal travelling heater method growth of $Hg_{1-x}Cd_xTe$ with crucible rotation*, J. Cryst. Growth **130**, 188 (1993).

[102] https://www.qsil.com/en/material/about-fused-quartz/.

[103] P. Dreier, Laboratory report, unpublished.

[104] J. Rodríguez-Carvajal, *Recent advances in magnetic structure determination by neutron powder diffraction*, Physica B **192**, 55 (1993).

[105] C. Petrovic, Y. Lee, T. Vogt, N. Lazarov, S. Bud'ko, and P. Canfield, *Kondo insulator description of spin state transition in $FeSb_2$*, Phys. Rev. B **72**, 045103 (2005).

[106] R. Kirby, T. Hahn, and B. Rothrock, *American Institute of Physics Handbook* (McGraw-Hill, New York, 1972).

[107] X. R. Huang, *LauePt, a graphical-user-interface program for simulating and analyzing white-beam X-ray diffraction Laue patterns*, J. Appl. Crystallogr. **43**, 926 (2010).

[108] R. D. Shannon, *Revised effective ionic radii and systematic studies of interatomic distances in halides and chalcogenides*, Acta Cryst. **32**, 751 (1976).

[109] G. Li, K. Kurosaki, Y. Ohishi, H. Muta, and S. Yamanaka, *Thermoelectric properties of Indium-added skutterudites* $In_xCo_4Sb_{12}$, J. Electron. Mater **42**, 1463 (2012).

[110] M. Naumann, Ph.D. thesis, Technische Universität Dresden, 2019.

[111] J. W. Sharp, E. C. Jones, R. K. Williams, P. M. Martin, and B. C. Sales, *Thermoelectric properties of* $CoSb_3$ *and related alloys*, J. Appl. Phys. **78**, 1013 (1995).

[112] T. Caillat, A. Borshchevsky, and J. P. Fleurial, in *Proceedings of the VIII International Conference on Thermoelectrics* (University of Texas at Arlington Press, Arlington, 1992).

[113] J. Ackermann and A. Wold, *The preparation and characterization of the cobalt skutterudites* CoP_3, $CoAs_3$ *and* $CoSb_3$, J. Phys. Chem. Solids **38**, 1013 (1977).

[114] C. Uher, *Recent trends in thermoelectric materials research I* (Elsevier, San Diego, 2001), pp. 139–253.

[115] J. Fainberg, D. Vizman, J. Friedrich, and G. Mueller, *A new hybrid method for the global modeling of convection in CZ crystal growth configurations*, J. Cryst. Growth **303**, 124 (2007).

[116] http://www.alu-scout.com.

[117] Data sheet from http://www-ferp.ucsd.edu/LIB/PROPS/PANOS/al2o3.html.

[118] Data sheet from http://www.kanthal.com.

[119] Data sheet from http://www.heraeus.com.

[120] A. M. A. Magomedov and B. P. Pashaev, *Thermal conductivity of alloys of the bismuth-antimony system in solid and liquid states*, Sov. Phys. J. **15**, 287 (1972).

[121] A. F. Crawley and D. R. Kiff, *The density and viscosity of liquid antimony*, Metall. Mater. Trans B **3**, 157 (1972).

[122] A. G. Ostrogorsky and M. E. Glicksman, *Handbook of crystal growth* (Elsevier, Amsterdam, 2015), pp. 995–1047.

[123] F. Aqra and A. Ayyad, *Theoretical estimation of temperature-dependent surface tension of liquid antimony, boron, and sulfur*, Metall. Mater. Trans. B **42**, 437 (2011).

Acknowledgments

Here, I would like to thank to everyone who helped me during my doctoral studies and throughout the writing of this dissertation.

I am extremely grateful to my supervisor Professor Peter Gille for the (personal and academic) support, guidance and, specially, for giving me the opportunity of being part of the Crystal Growth Group at the Ludwig Maximilian University of Munich. His expertise was invaluable in formulating the research questions and methodology, which made my doctorate very interesting. I would also like to thank him for the financial support to attend and present the results of my research work in several conferences.

Moreover, I am grateful to all the members of the Crystal Growth Group (specially, to Judith Schwerin, Michael Hahne, Kristian Bader, and Oliver Harder) for the their friendship, valuable discussions and fruitful suggestions. Many thanks to all other colleagues/friends from the Crystallography Department: Ulf Gattermann, Benedikt Röska, Stefanie Hoser, Patrick Eschenbacher, Alicia Dorner, Joan Uhlig, Isabella Kappel, Mar Simonet Roda, Martina Greiner, Laura Casella, Alexander Reul, Korbinian Schiebel, Sohyun Park, Bernd Maier, and to everyone who I accidentally forgot here. Another special thanks to Michael Hahne for the administrative help during the writing and submission process of my dissertation. *Vielen Dank für all Eure Unterstützung!*

Thanks to the people who helped me with the measurements and polishing of the grown crystals: Ulf and Benedikt (XRD), Dirk Müller (EPMA), Judith and Michael (Laue), Stefanie (polishing). I very much appreciate the support of the technicians Max Häberle and Detlef Körner. Thanks to Barbara Jaegar for helping me with all the administrative part.

I would like to acknowledge the effort of our collaborators from the Leibniz institute (Wolfram Miller) and Max Planck Institute in Dresden (Marcel Naumann, Elena Hassinger, Michael Baenitz) for the numerical simulation and physical property measurements, respectively. In particular, thanks to Marcel for the assistance and help in the analysis of the obtained results.

This journey would not have been possible without the support of my father and my family. PAPI querido MUCHISIMAS GRACIAS por tu apoyo incondicional en toda la etapa de mi vida personal y profesional. Muchas gracias por creer en mi y desearme lo mejor. También, agradezco mucho a mi tía Norma, tío Marcos, mis primas 'las ñatas' (Kassandra, Katherine, Rosalina, Mariela, y Anghela) y Panchito por acompañar a mi papi durante mi estancia aquí en Alemania.

I would also thank to my soon-to-be husband Leonardo Medrano for all the patience, encouragement, help, and support that he has offered me since we met at the UNMSM in Lima-Peru (2005). I am truly thankful for having you in my life. TE AMO!

Finally, muchas gracias to all my Peruvian friends (las gusanitas, Daniel, Kristians, Juan Manuel, Rosalyn,...) for sharing wonderful times while traveling, partying or just having dinner.

To conclude, I would like to express my sincere gratitude to the Peruvian National Council for Science, Technology, and Innovation (CONCYTEC) for the financial support to do my doctoral studies in Germany via the program "Becas para Estudios de Doctorado en el Extranjero" (grant no. 221-2014-FONDECYT). Also, I would like to thank the administrative assistance and help of Aldo de la Torre Guzmàn from the doctoral monitoring unit of CONCYTEC.

Thank you!
Vielen Dank!
Muchas gracias!